Engineering Particle Surface Chemistry and Electrochemistry with Atomic Layer Deposition

by

David Hyman Kentaro Jackson

A dissertation submitted in partial fulfillment of

the requirements for the degree of

Doctor of Philosophy

(Materials Science)

under the supervision of Professor Thomas F. Kuech

at the

UNIVERSITY OF WISCONSIN – MADISON

2017

Date of final oral examination: Monday May 1, 2017

The dissertation is approved by the following members of the Final Oral Committee:

Thomas F. Kuech, Professor, Chemical and Biological Engineering
Susan E. Babcock, Professor, Materials Science and Engineering
Xudong Wang, Professor, Materials Science and Engineering
Dane D. Morgan, Professor, Materials Science and Engineering
Paul Evans, Professor, Materials Science and Engineering

Engineering Particle Surface Chemistry and Electrochemistry using Atomic Layer Deposition

David H. K. Jackson

Under the supervision of Professor Thomas F. Kuech

at the University of Wisconsin – Madison

Atomic layer deposition (ALD) is a vapor phase thin film coating technique that relies on sequential pulsing of precursors that undergo self-limited surface reactions. The self-limiting reactions and gas phase diffusion of the precursors together enable the conformal coating of microstructured particles with a high degree of thickness and compositional control. ALD may be used to deposit thin films that introduce new functionalities to a particle surface. Examples of new functionalities include: chemical reactivity, a mechanically strong protective coating, and an electrically resistive layer. The coatings properties are often dependent on the bulk properties and microstructure of the particle substrate, though they usually do not affect its bulk properties or microstructure. Particle ALD finds utility in the ability to synthesize well controlled, model systems, though it is expensive due to the need for costly metal precursors that are dangerous and require special handling. Enhanced properties due to ALD coating of particles in various applications are frequently described empirically, while the details of their enhancement mechanisms often remain the focus of ongoing research in the field. This study covers the various types of particle ALD and attempts to describe them from the unifying perspective of surface science.

Mixed magnesium aluminum oxides were deposited onto γ-Al_2O_3 particles in varying Mg/Al precursor pulse ratios to study the formation of acidic and basic sites on the particle surface. Control over the acid/base properties of a catalyst could enable the development of bifunctional reactive catalysts with higher selectivity, and be used to elucidate two-site

chemisorption reaction mechanisms. Characterization of these ALD produced catalysts shows that the quantities and clustering of acid and base sites are controllable using process parameters. Acid sites have the highest surface density when atomic fractions of Mg and Al in the coating are similar. A fluorescent probe grafting technique that differentiated between clustered and isolated base sites showed no isolated sites present when both acid and base sites are mixed in similar quantities. Isolated base sites were identified at the two extremes, either when the concentration of acid sites on the surface is much higher than the base sites, or vice-versa. Catalyst activity in the self-condensation of acetone was similar to previous literature reports with reaction rate dependent on base site density, but not acid site density or clustering.

The effect of TiO_2 ALD coatings on cobalt/carbon water oxidation electrocatalysts was studied. The catalyst consisted of Co nanoparticles deposited onto a high surface area, mesoporous carbon support. A TiO_2 ALD coating on the electrocatalysts resulted in reduced onset potential of water oxidation and higher reaction rate compared to the control sample. The catalyst lifetime was also enhanced – the nanoparticles being more resistant to sintering due to encapsulation of the particles by the electrochemically robust TiO_2. Enhancement was attributed to the selective decoration of Co nanocrystal corners and edges with TiO_2. The TiO_2 decoration onto the Co creates Co^{4+}, an unusually high oxidation state that is not present in the common oxides: CoO or Co_3O_4. The Co^{4+} formed near the TiO_2-Co interface was observed using X-ray photoelectron spectroscopy (XPS) and attributed as the cause of increased electrochemical activity.

The Li-ion battery cathode material $LiNi_{0.5}Mn_{0.3}Co_{0.2}O_2$ (NMC) was ALD-coated with Al_2O_3 and annealed post deposition to study the effects on coin cell cycle performance and on the electrochemical decomposition of electrolytes. Cycle performance and

electrochemical properties of the cells exhibited complicated dependencies on annealing temperature. Al diffusion into the bulk NMC increases with annealing temperature and was observable starting at ~500 °C. Unique surface reactivity was observed in cells annealed at 500 °C, coinciding with the onset of measurable diffusion. These 500 °C cells underwent significantly more charge sequestering reactions during the initial two cycles as compared to all other samples. It is possible that the charge was consumed to form LiF, which was detected in high concentrations at the cathode surface after cycling. These cells demonstrated the all-around best performance: little reduction in initial capacity, improved capacity retention at high and low rates, and low self-discharge during an elevated temperature storage experiment. Formation of a charge sequestering LiF surface species could occur at the onset of diffusion and be correlated with the performance of the cells containing 500 °C annealed NMC.

Acknowledgements

I thank my advisor, Prof. Kuech, for his guidance and insight during my time at the UW. I have learned that attention to detail and sincere scientific inquiry are the key factors to successful research. I appreciate the numerous opportunities he has given me which have shaped my studies. My experiences attending meetings, listening to the discussions of talented scientists and engineers, and traveling the world to take part in several international scientific conferences have made a lasting and invaluable impact on me.

I would like to thank the professors who have been members of the various projects I have spent time on, who have given me so much of their time to discuss research, including: Prof. Dane Morgan, Prof. Robert Hamers, Prof. Mahesh Mahanthappa, Prof. George Huber and Prof. James Dumesic.

Many thanks also go to the other graduate and post-graduate students who have trained, supported and struggled with me during my graduate studies. Particular thanks go to Monika Wiedmann for first teaching me the ropes in atomic layer deposition. I am also grateful to the many staff scientists who have helped and trained me throughout the years, and the undergraduate students who have assisted me and taught me so much about leadership and team management.

The University of Wisconsin–Madison has made my education possible, for that I am forever grateful. I would also like to thank the people at funding organizations that made my research possible: the U.S. Department of Energy and The Dow Chemical Company.

Finally, I would like to dedicate this thesis to my parents Meyer and Noriko and girlfriend Jamie, who have given me so much love, support and encouragement.

Table of Contents

List of Figures

showing precursors entering the reactor and diffusing into the powder bed to coat the powder. c) Close up showing precursors diffusing through the wire cloth on the powder bed to prevent loss of the powder. d) Close up showing precursor diffusion into the powder bed and into the pores of the powder.

Figure 2.6. a) Schematic of a fluidized bed reactor for particle ALD. The reactor has an on-line in situ mass spectrometer, a stirring agitator, and vibration enhanced fluidization. The schematic on the right shows particle concentration as a function of height in the bed. b) Schematic of a rotary bed ALD reactor.

Figure 2.7. Schematic spatial ALD processes using powder reservoirs. a) Schematic of powder reservoir theory of operation i-iii. The powder to be coated is supported on a. b) CAD drawing of a powder reservoir type reactor.

Figure 2.8. Representative drawing of a lithium ion battery (LIB), in which Li^+ ions pass from a graphite anode to a $LiMO_2$ anode, while electrons travel through a load.

Figure 3.1. Exploded schematic of a typical half-cell with each component labeled. Cells are assembled bottom to top. The lithium anode is pressed against the steel spacer below it before being placed into the cell. The three droplets of electrolyte consist of 20 μL.

Figure 3.2. ALD pulse and purge times determined using a mass spectrometer. Signals of individual chemicals may be observed largely independent of one another. The spectra show the $TiCl_4$ – H_2O process which involves generation of HCl during half-reactions.

Figure 3.3. Diagram of the electron photoejection process. An X-ray with energy = hν collides with an orbital electron, resulting in ejection of a photoelectron with the energy of the incident X-ray minus the binding energy of the orbital electron.

List of Tables

1 Introduction

1.1 Motivation

Atomic layer deposition (ALD) is a vapor phase coating technique emerging as a tool for the synthesis of new classes of advanced particle-based materials. ALD is an established thin film deposition technique in the semiconductor industry, and is now gaining attention for its prospects in the field of powder coating with applications in Li-ion batteries, catalysis, light-emitting phosphors, medicine, cosmetics and solid lubricants. ALD uses sequential exposures of gas phase precursors that undergo complimentary, self-limiting surface reactions that allow for layer-by-layer deposition. The rapid sequential gas phase pulses and purges of self-limiting precursors allow geometrically complex structures to be conformally coated, provided that reactive surface sites are available to drive the ALD reaction chemistry.

The most widespread implementation of ALD is in the deposition of thin films on macroscopically planar substrates in the semiconductor industry. Particle ALD coating is much less prevalent, however its history dates back to 1967 in Russia, when titanium oxide and germanium oxide were deposited onto silica.[1] While planar ALD has rapidly outpaced particle ALD in research and in commercial viability, particle coating has nonetheless maintained a gradual growth throughout the course of ALD history due to its potential impacts. Ultimately, growth of the field is hindered by problems associated with powder handling and the orders of magnitude higher surface area of powders over planar substrates, which necessitates more precursor and longer exposure times to react over all available surfaces.

A major trend in science is towards nanoscale precision in engineering. ALD employs sub-nanometer level of thickness and compositional control so it is well-suited to facilitate technological advancement in multiple industries that use powdered materials. Powder-based technologies are ubiquitous in modern industry and implementation of industrial scale ALD

powder coating could find a wide range of applications. This study attempts to illustrate the range of powder ALD as a distinct area of surface science by addressing the problems of finer degree of control over surface species, and by improving the electrochemical stability of electrocatalysts and electrodes.

By the early 2010's, several approaches to powder handling in ALD had been demonstrated, including static bed,[2] fluidized bed,[3-6] rotating bed,[7] and semi-continuous bed.[8] With the proliferation of reactor technologies to address the issues of particle ALD, several advancements have been demonstrated across various powder-based technologies. ALD-coated catalytic metal nanoparticles have demonstrated dramatically improved stability and selectivity.[9, 10] The particle-based electrodes in lithium ion batteries have been given significantly longer lifetimes with a thin ALD coating.[11, 12] Further development into these and other powder technologies is expected to yield more breakthroughs in efficiency and effectiveness.

While improvements in catalysts and batteries have been demonstrated using ALD, many of these approaches remain exploratory. The mechanisms by which these improvements are achieved are not completely clear. For example, it is not understood exactly why ALD coating of batteries improves electrochemical performance in spite of their electrically insulating nature. The full range of applications of ultrathin ALD coatings on particles remains open to further development.

A deeper level of scientific understanding of the interactions between ultra-thin ALD coatings and particle substrates will guide the direction of the field as it progresses. Interfacial chemical species occur between a substrate and an ultrathin ALD coating and also within the coating itself. Due to the coatings being thin, substrate can affect the chemical properties of the coatings surface as well. Beyond acting as simple coatings, potential applications for particle ALD include: surface doping,[13] synthesis of two-dimensional surface

phases,[14] deposition of thin films with precisely controlled elemental compositions,[15] and as metal nanoparticle surface decorations that leave the substrate partially exposed to allow for bifunctional catalysis.[16]

Optimal catalytic supports have high surface area to maximize catalytic activity; however the synthesis of a high surface area catalyst of a specific composition is sometimes not feasible due to limitations in synthesis techniques. ALD can be used to deposit coatings of broad compositional variety onto a high surface area catalytic substrate, decoupling the surface chemistry from the materials properties. Metal nanoparticles are deposited onto high surface area supports in many catalytic applications. The coating of these crystalline metal nanoparticles with a metal oxide can lead to unique orientation-specific interactions with various crystal facets. These coatings leave low index planes uncoated, while capping and stabilizing the corners and edges, the sites most susceptible to leaching.[10, 17]

Electrochemical systems require particularly robust electrodes due to the corrosion accelerating effect of electric fields. It is important that electrochemical electrodes maintain longevity for economical utilization. ALD coatings can act as a protective layer preventing corrosion and other unwanted electrochemical reactions that reduce performance. They also may act as a method to improve the electronic characteristics of the electrode surface by accelerating the desired electrochemical reactions. Electrode properties can be modified using ALD by addressing requirements in chemical functionality as with catalysts, and also requirements in electronic properties.

This study aims to demonstrate the significance and far-reaching prospects of particle ALD via the three selected case studies as representative fields of application. Other applications exist as well, and are yet to be discovered, but these three are interesting case studies that demonstrate the capacity of ALD to stabilize a particles surface and to generate surfaces with unique chemical and electrochemical properties. Through a deeper

understanding of the surface properties of particle ALD-coated materials, these studies contribute to the growing field.

1.2 Scope of this Study

This study investigates the various aspects of surface science in particle atomic layer deposition as they affect the performance of catalyst, electrocatalyst and battery electrode particles. The nanoscale control offered by ALD makes it uniquely suited to improve effective performance and facilitate the development of advanced powder-materials.

Magnesium aluminum oxide coatings were deposited on γ-Al_2O_3 powders, coatings of various cation stoichiometries were synthesized through control over the ALD pulse sequence. Characterization showed a nonlinear relationship between on acid and base site densities that are controllable through process parameters.

Water oxidation catalysts composed of Co nanoparticles deposited onto activated carbon were coated with ALD TiO_2 and showed increased catalytic activity. This increase in activity was attributed to a Co^{4+} formed due to interactions with the TiO_2 and the Co particles.[18, 19]

High voltage $LiNi_{0.5}Mn_{0.3}Co_{0.2}O_2$ Li-ion battery cathode powders were coated with Al_2O_3 at 100 °C and then annealed in batches at temperatures ranging from 300 to 700 °C. A surface species forming during onset of observable diffusion at 500 °C may be correlated with its all around good performance across high and low rate charge-discharge cycling, and in elevated temperature storage tests.

1.3 Organization of this Document

Chapter 1 contains an introduction and motivates the work contained in this study.

Chapter 2 contains background information that forms the basis for the studies presented in later chapters. Surface science, catalysis, electrochemical, and ALD growth fundamentals are presented.

Chapter 3 contains information about the experimental techniques used in these studies. Specific experimental details are provided in later chapters, but the theory and description behind the conducted experiments are given in this chapter. The specific techniques used in this study are grouped based on their usage as either sample preparation or as materials characterization techniques.

The experimental results and their discussion are contained in Chapters 4-6. Chapter 4 presents a study of magnesium aluminum mixed oxide compositional effects on the acid/base properties of a solid base catalyst. Chapter 5 presents a study on TiO_2 coatings deposited on cobalt nanoparticle-based water oxidation electrocatalysts. Chapter 6 presents a study on the effects of annealing on Al_2O_3 coated lithium ion battery cathodes on charge-discharge cycle performance.

Conclusions and opportunities for future work are presented in Chapter 7.

1.4 References

1. Ahvenniemi, E.; Akbashev, A. R.; Ali, S.; Bechelany, M.; Berdova, M.; Boyadjiev, S.; Cameron, D. C.; Chen, R.; Chubarov, M.; Cremers, V.; Devi, A.; Drozd, V.; Elnikova, L.; Gottardi, G.; Grigoras, K.; Hausmann, D. M.; Hwang, C. S.; Jen, S.-H.; Kallio, T.; Kanervo, J.; Khmel nitskiy, I.; Kim, D. H.; Klibanov, L.; Koshtyal, Y.; Outi, A.; Krause, I.; Kuhs, J.; Kärkkäne n , I.; Kääriäinen, M.-L.; Kääriäinen, T.; Lamagna, L.; Łapicki, A. A.; Leskelä, M.; Lipsanen, H.; Lyytinen, J.; Malkov, A.; Malygin, A.; Mennad, A.; Militzer, C.; Molarius, J.; Norek, M.; Özgit- Akgün , Ç.; Panov, M.; Pedersen, H.; Piallat, F.; Popov, G.; Puurunen, R. L.; Rampelberg, G.; Ras, R. H. A.; Rauwel, E.; Roozeboom, F.; Sajavaara, T.; Salami, H.; Savin, H.; Schneider, N.; Seidel, T. E.; Sundqvist, J.; Suyatin, D. B.; Törndahl, T.; van Ommen, J. R.; Wiemer, C.; Ylivaara, O. M. E.; Yurkevich , O., Review Article: Recommended reading list of early publications on atomic layer deposition—Outcome of the "Virtual Project on the History of ALD". , 35 (1), 010801. doi:. In Journal of Vacuum Science and Technology A, 2017; Vol. 35, p 010801.

2. Libera, J. A.; Elam, J. W.; Pellin, M. J., Conformal ZnO coatings on high surface area silica gel using atomic layer deposition. *Thin Solid Films* **2008,** 516, (18), 6158-6166.

3. King, D. M.; Spencer, J. A.; Liang, X.; Hakim, L. F.; Weimer, A. W., Atomic layer deposition on particles using a fluidized bed reactor with in situ mass spectrometry. *Surface & Coatings Technology* **2007,** 201, (22-23), 9163-9171.

4. Wank, J. R.; George, S. M.; Weimer, A. W., Coating fine nickel particles with Al2O3 utilizing an atomic layer deposition-fluidized bed reactor (ALD-FBR). *Journal of the American Ceramic Society* **2004,** 87, (4), 762-765.

5. Wank, J. R.; George, S. M.; Weimer, A. W., Nanocoating individual cohesive boron nitride particles in a fluidized bed by ALD. *Powder Technology* **2004,** 142, (1), 59-69.

6. Beetstra, R.; Lafont, U.; Nijenhuis, J.; Kelder, E. M.; van Ommen, J. R., Atmospheric Pressure Process for Coating Particles Using Atomic Layer Deposition. *Chemical Vapor Deposition* **2009,** 15, (7-9), 227-233.

7. McCormick, J. A.; Cloutier, B. L.; Weimer, A. W.; George, S. M., Rotary reactor for atomic layer deposition on large quantities of nanoparticles. *Journal of Vacuum Science & Technology A* **2007,** 25, (1), 67-74.

8. King, D. M.; Weimer, A. W.; Lichty, P., Semi-Continuous Vapor Deposition Process for the Manufacture of Coated Particles. In US20110236575, 2011.

9. Lu, J.; Fu, B.; Kung, M. C.; Xiao, G.; Elam, J. W.; Kung, H. H.; Stair, P. C., Coking- and Sintering-Resistant Palladium Catalysts Achieved Through Atomic Layer Deposition. *Science* **2012,** 335, (6073), 1205-1208.

10. Zhang, H. B.; Gu, X. K.; Canlas, C.; Kropf, A. J.; Aich, P.; Greeley, J. P.; Elam, J. W.; Meyers, R. J.; Dumesic, J. A.; Stair, P. C.; Marshall, C. L., Atomic Layer Deposition Overcoating: Tuning Catalyst Selectivity for Biomass Conversion. *Angewandte Chemie-International Edition* **2014,** 53, (45), 12132-12136.

11. Jung, Y. S.; Lu, P.; Cavanagh, A. S.; Ban, C.; Kim, G. H.; Lee, S. H.; George, S. M.; Harris, S. J.; Dillon, A. C., Unexpected Improved Performance of ALD Coated LiCoO2/Graphite Li-Ion Batteries. *Advanced Energy Materials* **2013,** 3, (2), 213-219.

12. Li, X. F.; Liu, J.; Meng, X. B.; Tang, Y. J.; Banis, M. N.; Yang, J. L.; Hu, Y. H.; Li, R. Y.; Cai, M.; Sun, X. L., Significant impact on cathode performance of lithium-ion batteries by precisely controlled metal oxide nanocoatings via atomic layer deposition. *Journal of Power Sources* **2014,** 247, 57-69.

13. Xie, M.; Hu, T.; Yang, L.; Zhou, Y., Synthesis of high-voltage (4.7 V) LiCoO2 cathode materials with Al doping and conformal Al2O3 coating by atomic layer deposition. *Rsc Advances* **2016,** 6, (68), 63250-63255.

14. Wang, K. X.; Li, X. H.; Chen, J. S., Surface and Interface Engineering of Electrode Materials for Lithium-Ion Batteries. *Advanced Materials* **2015,** 27, (3), 527-545.

15. Muylaert, I.; Musschoot, J.; Leus, K.; Dendooven, J.; Detavernier, C.; Van der Voort, P., Atomic Layer Deposition of Titanium and Vanadium Oxide on Mesoporous Silica and Phenol/Formaldehyde Resins - the Effect of the Support on the Liquid Phase Epoxidation of Cyclohexene. *European Journal of Inorganic Chemistry* **2012**, (2), 251-260.

16. Alba-Rubio, A. C.; O'Neill, B. J.; Shi, F.; Akatay, C.; Canlas, C.; Li, T.; Winans, R.; Elam, J. W.; Stach, E. A.; Voyles, P. M.; Dumesic, J. A., Pore Structure and Bifunctional Catalyst Activity of Overlayers Applied by Atomic Layer Deposition on Copper Nanoparticles. *Acs Catalysis* **2014,** 4, (5), 1554-1557.

17. O'Neill, B. J.; Jackson, D. H. K.; Crisci, A. J.; Farberow, C. A.; Shi, F. Y.; Alba-Rubio, A. C.; Lu, J. L.; Dietrich, P. J.; Gu, X. K.; Marshall, C. L.; Stair, P. C.; Elam, J. W.; Miller, J. T.; Ribeiro, F. H.; Voyles, P. M.; Greeley, J.; Mavrikakis, M.; Scott, S. L.; Kuech, T. F.; Dumesic, J. A., Stabilization of Copper Catalysts for Liquid-Phase Reactions by Atomic Layer Deposition. *Angewandte Chemie-International Edition* **2013,** 52, (51), 13808-13812.

18. Yeo, B. S.; Bell, A. T., Enhanced Activity of Gold-Supported Cobalt Oxide for the Electrochemical Evolution of Oxygen. *Journal of the American Chemical Society* **2011,** 133, (14), 5587-5593.

19. Gerken, J. B.; McAlpin, J. G.; Chen, J. Y. C.; Rigsby, M. L.; Casey, W. H.; Britt, R. D.; Stahl, S. S., Electrochemical Water Oxidation with Cobalt-Based Electrocatalysts from pH 0-14: The Thermodynamic Basis for Catalyst Structure, Stability, and Activity. *Journal of the American Chemical Society* **2011,** 133, (36), 14431-14442.

2 Background Information

2.1 Atomic layer deposition

2.1.1 Surface Science in ALD

Surface science is the study of interfaces between distinct states of matter, and the solid-gas interface is at the heart of ALD.[1, 2] The advanced powder material applications examined in this study; catalysis, electrocatalysis and batteries, include the solid-gas and solid-liquid interfaces. The termination of bulk solid crystal results in exposed crystal facets; these facets possess unique atomic arrangements that determine the properties of their surfaces. An individual powder particle will have a diverse range of exposed facets. Certain surface sites such as extra atoms, surface vacancies, or terrace boundaries, often possess heightened chemical reactivity due to their low coordination. A particle may also be amorphous with no crystalline atomic arrangement, in which case the surface is a disordered assortment of under-coordinated atoms. The molecules and atoms in the liquid or gas phase may undergo reactions with a solid surface, first forming adsorbed surface species and then forming localized chemical bonds with reactive surface atoms. A facet surface is also composed of local atomic arrangements that are deviations from the perfect facet. The upper few layers of a bulk material make significant contributions to surface properties due to surface restructuring or reconstruction and the reaction of surfaces with ambient chemicals such as O_2, H_2O and CO_2.

The process of surface adsorption is well studied, and is often classified as either physisorption or chemisorption. Physisorption is the adsorption of a molecule to a surface without forming a strong covalent or ionic bond. The molecule becomes trapped in the potential well of the surface, typically via van der Waals forces, and can be mobile in the plane of the surface. A chemisorbed adsorbate forms a chemical bond to specific surface site and becomes fixed in place so long as the bond is intact. Such a chemical bond is typically stronger and physically shorter than the bond between the surface and a physisorbate. In ALD, deposition occurs via chemisorption of precursors to a substrate surface. A molecule approaching a surface has a kinetic energy based on temperature. As it approaches a surface,

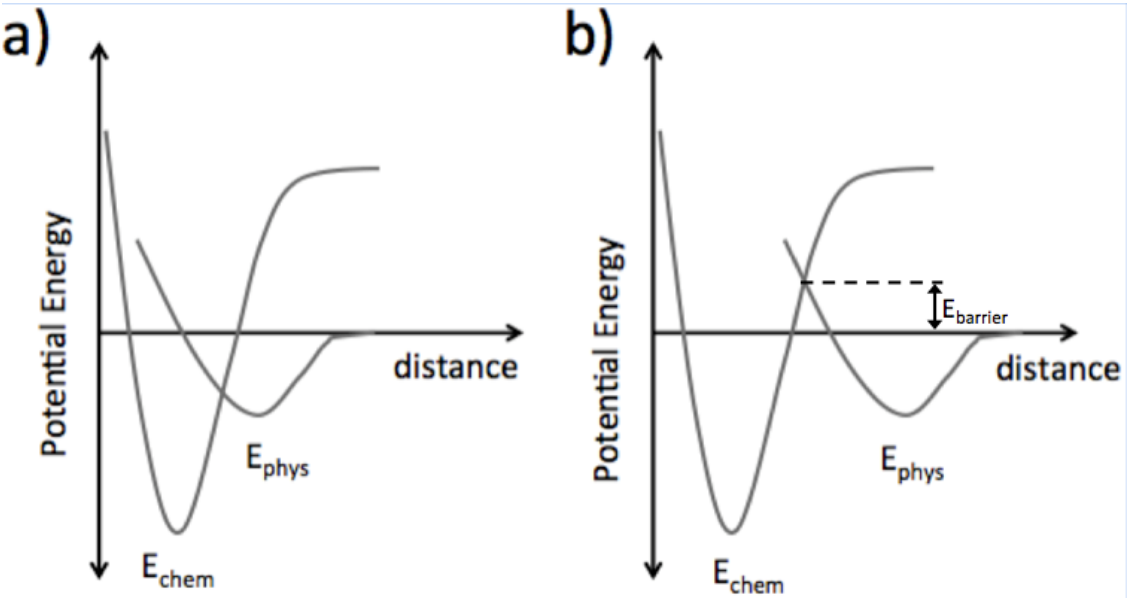

Figure 2.1. The potential energy diagram of an adsorbate as it approaches a surface. E_{chem} represents the chemisorbed species, and E_{phys} represents the physisorbed species. a) The case where no barrier exists between the physisorbed and chemisorbed state. b) The case where an energetic barrier ($E_{barrier}$) exists between the physisorbed and chemisorbed states.

it typically falls into a potential energy well, becoming physisorbed. In some cases, no potential energy barrier exists between the physisorbed and chemisorbed state, as shown in Figure 2.1a, and the mobile, physisorbed surface species quickly transitions to the lower potential energy of the chemisorbed state. In other cases, a significant energy barrier can exist

between the two states, as shown in Figure 2.1b, and the adsorbate may remain in the mobile physisorbed state. Typically there is very little barrier to desorb into the gas phase, and desorption acts in competition with further reaction to the chemisorbed state. At low temperatures, precursors may lack the thermal energy to escape this well and remain trapped as mobile surface species.

In ALD a few distinct types of chemisorption reactions exist dependent on the precursor and substrate combination. The two most common types of chemisorption reaction are the ligand exchange reaction and the dissociative reaction. In a ligand exchange reaction, a metal-ligand bond of the precursor breaks and is replaced by a bond to a reactive surface species.[3] An example of this type of reaction is:

1A) $$* \mathrm{MOH} + \mathrm{TiCl_4\ (g)} \rightarrow * \mathrm{MOTiCl_3} + * \mathrm{HCl}$$

* Denotes a surface species and M indicates a metal atom in the substrate

In dissociative chemisorption, a metal-ligand bond in the precursor is broken, and both the metal precursor and the cleaved ligand are bound to the substrate.[3] An example of this type of reaction may be written as:

2A) $$2 * \mathrm{MOH} + \mathrm{TiCl_4\ (g)} \rightarrow * \mathrm{MOTiCl_3} + * \mathrm{MCl} + \mathrm{H_2O\ (g)}$$

The reaction of the complementary precursor would proceed via ligand replacement in both these cases as follows (where equation 1B follows 1A and 2B follows 2A):

1B) $$* \mathrm{MOTiCl_3} + 3\ \mathrm{H_2O\ (g)} \rightarrow * \mathrm{MOTiOH_3} + 3\ \mathrm{HCl(g)}$$

2B) $$* \mathrm{MOTiCl_3} + * \mathrm{MCl} + 4\ \mathrm{H_2O\ (g)} \rightarrow * \mathrm{MOTiOH_3} + * \mathrm{MOH} + 4\ \mathrm{HCl(g)}$$

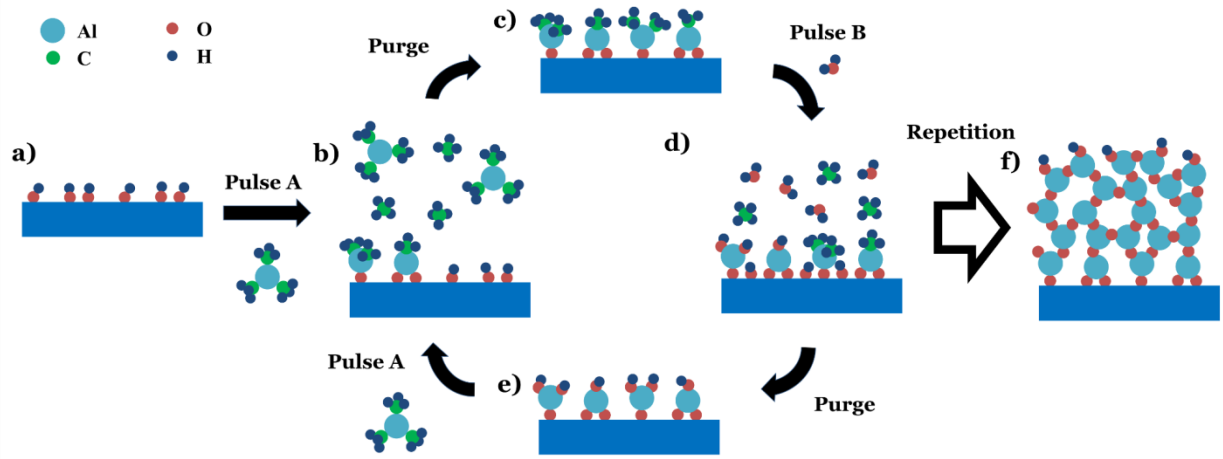

Figure 2.2. A schematic of a representative ALD process: a) The substrate surface with reactive OH groups, b) the surface reacting with TMA, forming chemisorbed surface species and gas phase reaction byproducts, c) substrate surface saturated with precursor, d) surface reacting with H_2O, with ligands being removed, and further formation of gas phase reaction byproducts, e) substrate surface saturated with H_2O reactions, f) ALD film formed after repetition of cycles.

A schematic representation of the trimethylaluminum (TMA) – H_2O process is presented in Figure 2.2. Precursors are pulsed individually into a reactor until the surface reaction reaches completion (Fig 2.2a-b). Surface saturation is achieved when all possible sites on a surface have generated chemisorbed precursors and no further reaction is possible. At this point the pulse is terminated and unreacted precursor and gas phase reaction byproducts are purged from the reactor, leaving the surface terminated with chemisorbed precursors that will react with the complementary precursor (Fig 2.2b-c). This pulse-purge process is cycled between the complementary precursors to deposit multiple ALD layers. While at least two precursors are required, more than two are routinely employed for the formation of materials.

The idealized self-limiting nature of these reactions allows films to be conformal over high aspect ratio morphologies, such as trenches, nanorods and mesoporous particles with tortuous diffusion pathways. As a result ALD is well suited for powder coating,[4, 5] especially where nm-scale control over film thickness is desirable. A film's thickness is determined by

multiplying the number of ALD cycles by the characteristic growth per cycle (GPC) of the ALD process. The type of surface reactions occurring during ALD will affect film microstructure and determine the observed GPC, which is usually <1nm per cycle.

2.1.2 ALD Process Conditions

The extent and kinetics of chemisorption reactions and thus film deposition are in part dependent on the availability of surface sites. Surface site type and quantity are affected by prior film deposition and by any thermochemical pretreatment of the surface, such as an acid 'rinse' or high temperature heat treatment. GPC values in the initial and later stages of film growth are frequently different due to differences in the reactivity of the initial substrate surface and the surface of the growing film (Figure 2.3a). A nucleation stage that occurs during the early stages of ALD film formation on the substrate may result in some degree of island growth. Surface reactivity may be exploited to control film microstructure and composition.

ALD film growth is dependent on sequential, self-limited surface reactions, in contrast to other vapor phase deposition processes such as physical vapor deposition and chemical vapor deposition, in which continuous deposition occurs. ALD processes must be operated under conditions that minimize continuous growth and selectively drive self-limited deposition to take place. The range of processing conditions that lead to self-limited ALD growth is called the *ALD window*. The ALD window for each process will correspond to a certain temperature range and to the length of the pulse and purge steps. Four temperature-related factors may cause a process to deviate from self-limiting growth behavior needed for ALD[3]:

1. *Decomposition above an upper temperature bound:* Homogeneous gas phase precursor decomposition and/or homogeneous decomposition of physisorbed precursors leads to continuous deposition.
2. *Desorption above an upper temperature bound:* Weak chemical bonds and low vapor pressure of film components in the gas phase drive their evaporation, counteracting deposition.
3. *Low reactivity below a lower temperature bound:* Thermal energy required to overcome chemisorption reaction barriers is insufficient and no precursor deposition occurs.
4. *Condensation below a lower temperature bound*: Precursor desorption from the physisorbed state is inhibited causing formation of multilayers that are not removed during the purging stage.

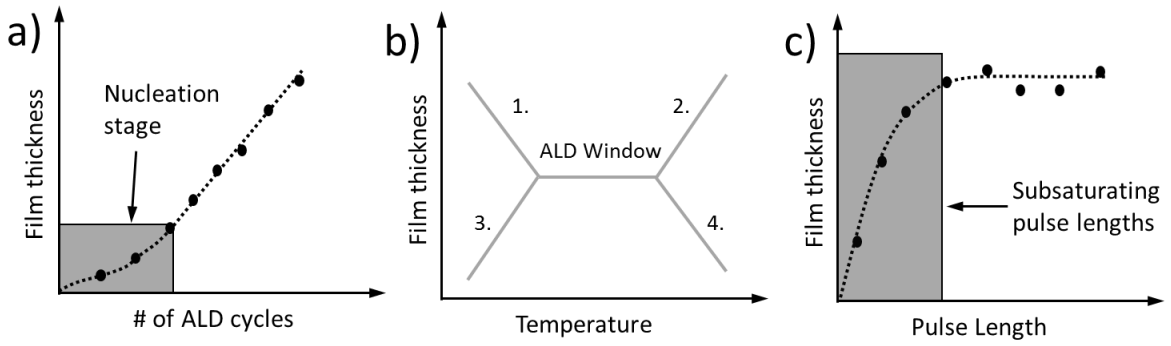

Figure 2.3. a) Film thickness versus number of cycles showing variation in growth per cycle in the initial stage of film growth. b) A scheme depicting the types of self-limited and non-self-limited deposition in their temperature ranges where 1 = condensation, 2 = decomposition, 3 = low reactivity and 4 = desorption. c) Films deposited using pulses that are too short lead to thinner films as a result of incomplete surface reactions, or sub-saturation.

Self-limited growth is often confirmed through a *saturation curve*[3] (depicted in Figure 2.3b) which plots film thickness versus precursor pulse length. If precursor pulses are not

sufficiently long, the total flux of precursor to the surface will not result in saturation of all reactive sites, leading to sub-saturating growth. Sub-saturating growth results in films that are thinner than predicted from GPC and yield a spatial inhomogeneity in film thickness. Pulses that exceed the saturation length do not result in thicker films because precursor deposition does not occur beyond monolayer saturation. If purge times between precursor pulses are too short, the unreacted precursor will not be sufficiently purged, and gas phase and physisorbed multilayers of precursor remain present during pulsing of the next precursor. Two precursors mixing in the gas phase can lead to gas phase reaction products that deposit onto a sample. Precursor multilayers that do not desorb can react with the complementary precursor resulting in multilayer deposition.

To achieve conformal coatings with ALD on high surface area materials such as powders, long precursor pulse times are necessary. This increase in pulse time is due to precursor and byproduct mass transport limitations, and it increases the possibility of non-self-limiting growth. Longer pulse times may lead to a small amount of continuous deposition due to a very low but non-zero reaction rate counteracting self-limiting growth. An example of non-ideal conformality is found in the coating of trench structures with hafnium oxide, which can result in thicker coatings at the tops of the trenches than at the bottoms.[6] This non-conformality may be due to insufficient pulse lengths, or to a small amount of continuous deposition. The top of the trench is exposed to the Hf source at a higher partial pressure than seen in the base of the trench, leading to a higher reactant dose and increased deposition at the trench opening. Reports on other high surface area materials systems have noted the deviation from purely self-limited growth, such as in the deposition of Al_2O_3 on battery $LiCoO_2$ cathode powders,[7] the deposition of tungsten oxide on TiO_2 powders,[8] and in a TiN process with precursors decomposing during long pulses.[9] While the ideal self-limiting

growth mode is commonly used to describe ALD, deviations from ideal self-limited growth can play a significant role in the application of ALD to powders. Researchers looking to leverage the advantages of ALD in powders must to be cognizant that self-limited deposition and continuous deposition are part of the same growth continuum.

2.1.3 ALD Process Types

The example of ALD shown in Figure 2.2 is representative of a binary half-reaction process leading to the formation of thermodynamically favored surface species. The thermally-driven, two precursor (AB) process is the most commonly employed process, and several variations of it exist. For example, three different precursors can be used, such as aminopropyl triethoxysilane – H_2O – ozone,[10] or $Pd(hfac)_2$ – TMA – H_2O, in an ABC sequence.[11] The complexity of the reaction sequence can be further increased to create ABCB processes, which have been used in the deposition of mixed oxides, such as TMA – H_2O – Cp_2Mg – H_2O.[12, 13] Flexibility in reaction sequencing is a significant part of what makes ALD such an attractive method of thin film synthesis.

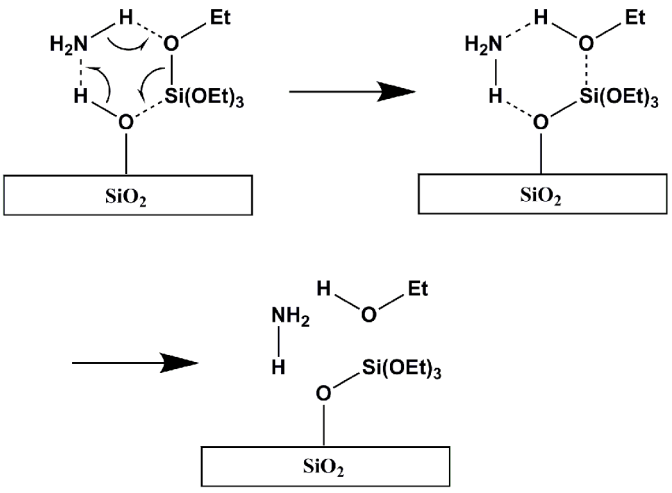

Figure 2.4. Proposed mechanism for Lewis base catalysis of SiO_2 atomic layer deposition during the $Si(OEt)_4$ half-reaction using NH_3. a) NH_3 forms a six-membered ring complex with silanol and $Si(OEt)_4$, b) pushing electrons in the six membered ring complex creating a more reactive and nucleophilic surface oxygen c) resulting in a Si surface species, NH_3, and the reaction byproduct ethanol.

The simultaneous introduction of specific reactants can open possible process windows that extend the previously mentioned ALD window by catalyzing a half-reaction. This co-addition or co-pulsing of reactants that do not remain in the film yet interact with ALD precursors can facilitate the film deposition process. These catalyzed ALD processes, usually referred to as catalytic-ALD, may be written as an A/C – B/C sequence. The most well studied example is the use of an amine catalyst to facilitate the reactions between the surface and precursors which have been developed to enable the low temperature deposition of SiO_2.[14-20] Si precursors such as $SiCl_4$ and TEOS possess low reactivity and require somewhat high deposition temperatures compared to those typically used in ALD (>250 °C).[14-20] Amine catalysts enables the deposition of SiO_2 at room temperature, avoiding potential thermally-induced damage to other system components, such as those on an existing electronic circuit or supported metal nanoparticles. A proposed catalytic reaction mechanism is shown in Figure 2.4, where ammonia is hypothesized to form hydrogen bonds with surface silanol groups, thus increasing the nucleophilic nature of the hydroxyl oxygen and catalyzing the deposition of $SiCl_4$.[16]

In contrast to thermally or catalytically-driven ALD, film deposition may also be enhanced using the in situ transfer of energy to precursors to generate reactive molecules such as ozone or the metastable species found in plasmas. Energy-enhanced ALD (EE-ALD) is used as an umbrella term to encompass a variety of methods used to transfer energy to precursors before they reach the substrate. EE-ALD methods include plasma-enhanced ALD (PE-ALD),[21] hot wire ALD,[22-25] and ALD processes using ozone.[6, 10, 26-30] Ozone can be

generated in oxygen plasma or through the use of UV light irradiation. EE-ALD techniques are typically employed to reduce the deposition temperature, to circumvent the need for water as the oxygen precursor, or to increase growth rates.[29] Careful design of process and reactor conditions, including the wall material, are important considerations in these EE-ALD methods. For example in PE-ALD oxygen radical recombination on reactor walls can be 3 orders of magnitude higher than on a SiO_2 surface, dramatically reducing these species' lifetime.

The least energetic of the PE-ALD techniques is called radical-enhanced ALD (REALD), which typically utilizes plasma generated through a RF-coupled source, electron-cyclotron-resonance, or surface-wave-type plasmas powered by a microwave source.[21, 29] The source is positioned sufficiently far from the sample that ions generated in the plasma recombine and are quenched before they reach the sample, while the remaining radicals act as precursors to film growth. Another technique, hot-wire ALD, generates radicals as precursors using a filament heated to ~1300 to 1900 °C placed near the inlet, on which precursors are cracked before entering the reactor.[22-25, 29] Remote plasma ALD is similar to REALD; however, a remote plasma source is positioned sufficiently close to the reactor that the concentration of ions reaching the sample is controlled and does not necessarily diminish to zero.[21, 29] The remote plasma source in this case is separate from the reaction chamber, but the substrate can experience a small concentration of impinging ions and a high radical flux. The EE-ALD approach with the highest amount of energy directed to the growth front is direct plasma ALD. This approach involves an electrical connection between one of the plasma electrodes and a substrate creating a near-surface electric field generally perpendicular to the surface directing and accelerating ions to the growth front.[21, 29] The kinetic energy of the ions can be transferred to the adsorbed species, leading to an enhanced

reaction rate at low substrate temperatures. The required electrical connectivity is often difficult to achieve and hence the use of direct plasma on powders poses significant obstacles. The EE-ALD approaches most relevant to catalysis-based applications are therefore ozone ALD, radical enhanced ALD and remote plasma ALD. The growth of AlN[31] and TiN[32] on powders using NH_3 plasma has been demonstrated using remote plasma ALD.

A wide range of materials may be deposited or coated by ALD. The self-limiting growth mode allows for conformally-coated substrates in almost any geometry.[33-42] Additionally, selective coating may be achieved by control over the nature and density of active species on the substrate.[43-49] ALD layers can be uniformly developed over complex geometries, provided that the entire surface has appropriate reactive sites. The possible materials with complex geometries coated by ALD include hierarchically-structured mesoporous oxides,[35-38] zeolites,[39-42] high aspect ratio nanostructures (i.e. nanowires,[50, 51] nanotubes[52-57]), complex self-assembled surfactants[34] and block copolymers.[58] Furthermore, the choice of the ALD precursors, surface preparation, and deposition conditions allows for the production of pinhole-free coatings, porous coatings,[49, 59-61] coatings with compositionally controlled gradients,[12, 13, 62-64] nanolaminates,[65-68] nanoparticles,[69-71] and core-shell structures.[72-74] This wide array of synthesis approaches to the ALD process has only begun to be exploited for powder applications.

The structure and composition of an ALD film is dependent on the choice of precursor. In addition to oxides, ALD nitrides,[9, 75, 76] sulfides,[77-79] carbides[80] and other binary alloys have been deposited through appropriate design of half-reaction schemes. Metals are deposited using a reducing agent instead of an oxidant.[70, 71, 73, 81-85] For example, the processes for TiO_2 ($TiCl_4$ – H_2O) and Al_2O_3 (TMA – H_2O), may be modified so that the H_2O pulses are replaced with NH_3 pulses, resulting in the growth of TiN[76, 86] and AlN.[87, 88] In the case of

some ALD-grown oxides, the choice of oxygen-containing source can change the bonding and oxygen content.[26] The specific reactants, while nominally generating films of the same composition, can affect the microstructure and defect concentration. For example, Al_2O_3 films grown with ozone have been found to contain a lower concentration of Al-Al bonds and O-H bonds than Al_2O_3 grown with H_2O, effectively giving ALD another degree of control over the resulting atomic structure.[26]

In addition to the deposition of conformal coatings, nanoparticles may also be formed on a surface through an appropriate choice of precursors, substrate, and deposition conditions. Nanoparticle formation is especially notable in the deposition of metals for catalysis, where ALD provides exceptional control over particle size.[69-71] The initial formation of sparsely spaced metal clusters or islands serve as nucleation points during the ALD process. Nanoparticle growth proceeds through an island growth mode often referred to as the Volmer-Weber growth mechanism.[89] The metal precursors can have a stronger interaction with the preexisting deposited metals than with the substrate, leading to the preferential formation of islands instead of conformal films. These interactions between metal precursors, substrates, and surface metal deposits in ALD have been demonstrated in certain systems to allow core shell metal nanoparticles to be produced with a high degree of compositional control. [72-74]

The selective adsorption of molecules which block or consume active sites prior to the initiation of the ALD cycles prevents these sites from participating in ALD film formation, creating templates for selectively coated surfaces. The templates can be removed after the ALD process, creating controlled porosity or the formation of microstructure in the ALD film.[48, 90] Selective coating by ALD was first developed through the lithographic patterning of planar surfaces with unreactive organosilanes.[48] The templating approach was extended to

powders by grafting unreactive template molecules onto TiO_2 particles.[90] The template molecules serve to block ALD coating, resulting in the formation of nanobowls that allowed for finely tuned sieving of reactant molecules by controlling the size and shape of the template as well as the thickness of the film.[90] Another example of atomic selectivity in the ALD synthesis of catalysts has also been demonstrated in the deposition of oxides onto metal surfaces, in which edge and corner sites were significantly more reactive with the coating precursors than the low index number facets.[49, 91] If greater than ~30 ALD cycles were used, the ALD films coalesced, completely encapsulating the metal. Subsequent high temperature treatment of encapsulated particles led to the formation of pores in the coating through the densification of the ALD film, leading to a selectively exposed metal surface.[8] The chemical bonds formed between the ALD film and the highly reactive edge and corner metal sites stay intact, while the oxide coating de-wets from the lower index planes. These pores allow the diffusion of reactants through the coating to undergo chemical transformation at the metal surface.

An emerging field within ALD is the production of organic and hybrid inorganic-organic materials. These techniques include the growth of inorganic materials on organic substrates, the growth of polymers, and the growth of hybrid inorganic-organic films. Recent studies have demonstrated the deposition of model inorganic films, such as Al_2O_3, onto substrates such as polymers[92, 93] nanofibers[94, 95] and surfactants.[34] Techniques that utilize organic molecules exclusively as precursors, or organic molecules in conjunction with metal precursors, are categorized as molecular layer deposition (MLD).[96, 97] A class of hybrid inorganic-organic materials produced using this technique are the *metalcones* (i.e., alucone, zincone and titanicone).[96] The simplest example of a metalcone process is the TMA – ethylene glycol process to produce alucone.[98] The alcohol groups of the ethylene glycol react

with the TMA in a similar fashion to the typical TMA – H_2O process, with ethylene glycol spacers linking molecular AlO_x layers. Metalcone films can have excellent compliance[96] and may be pyrolized to produce graphitic microdomains embedded within an oxide,[99] or oxidized to generate highly porous oxides.[59, 61]

2.1.3 Powder ALD reactor designs

Many ALD processes were developed primarily for the coating of planar substrates such as silicon wafers. New designs and approaches are required to utilize ALD processes on powders both on the research and industrial scales. Powders present the most dramatically different case from the typical planar Si wafer, with increased diffusion times required for precursors to travel through pores on the meso-scale, and orders of magnitude more surface area which require correspondingly longer reaction times or higher reactant partial pressures in the ALD reactor. Many attempts have been made to agitate particle beds to decrease diffusion times and prevent particle agglomeration. In this section, different ALD reactor configurations are briefly described. A more detailed article discussing the various techniques to use ALD for coating of powders may be found in reference {[100]}.

The simplest and most established approach to the coating of powders consists of a static bed of particles into which the precursor vapors must diffuse and permeate to reach and coat all surfaces. The bed may be in a crucible or tray supported on a heating stage,[100] or it may be in a flow tube with a specifically designed tray, such as that seen in Figure 6.[101] The diffusion kinetics for this type of reactor configuration may be simplified to a model that treats the bed as a series of channels between particles.[102] Analytical solutions to this growth model can be obtained to describe the ALD growth process. These solutions are important in developing a fundamental understanding of the ALD processes.[100, 103, 104] Assuming typical particle sizes and reaction conditions, a powder or particle bed depth of greater than a few

hundred microns would require precursor residence times that are unreasonably long for practical applications (greater than a few minutes per precursor pulse).

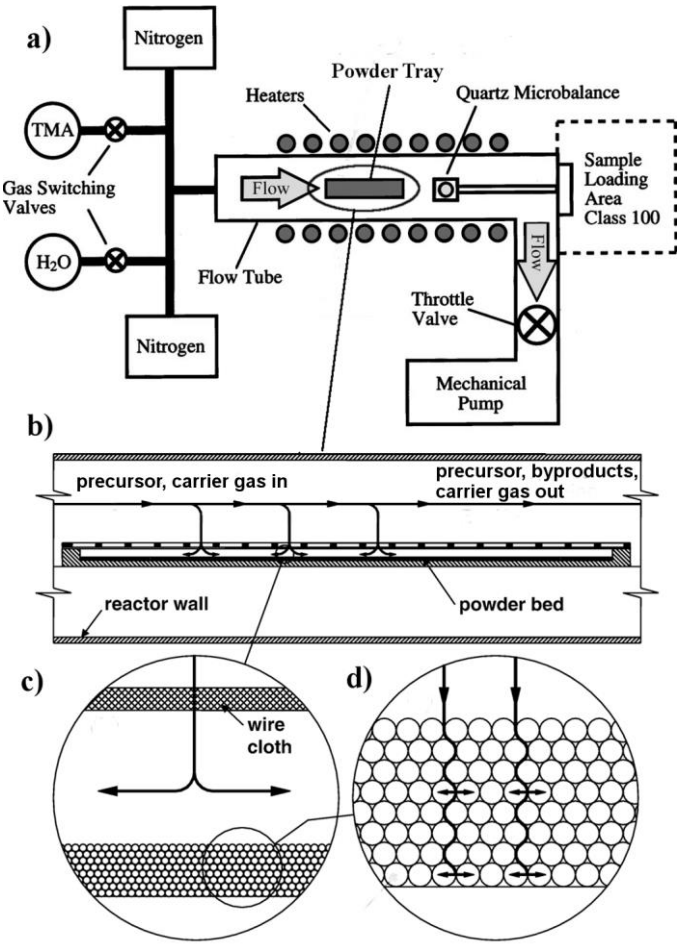

Figure 6.5. a) ALD reactor schematic showing precursors, carrier gas, heated flowtube, valves, and pump, with a powder tray in the flowtube. b) Side view of the powder tray showing precursors entering the reactor and diffusing into the powder bed to coat the powder. c) Close up showing precursors diffusing through the wire cloth on the powder bed to prevent loss of the powder. d) Close up showing precursor diffusion into the powder bed and into the pores of the powder. Part a) adapted with permission from Elam et al. Copyright 2002 AIP Publishing LLC.[105] Parts b)-d) adapted with permission from Libera et al. Copyright 2008 Elsevier B.V.[101]

Various approaches to enhance the reactant contact with the particle surface in a static bed have been developed. Precursors may continuously flow through the reactor under an active pressure drop, permitting a high reactant partial pressure to be present throughout the reaction. Alternatively, the precursors may be dosed and held in a static, non-flowing reactor,

allowing a ‘soak time’ for thorough reactant diffusion and reaction, leading to greater precursor utilization. This static bed approach is well suited for the laboratory scale; however, batch size is typically limited to several grams.

Particle coating in a fluidized bed is a standard industrial approach to powder processing; however, the use of fluidized bed reactors for ALD is less common.[106] An example of a fluidized bed ALD reactor design is shown in Figure a, and a few fluidized bed ALD reactor options are now commercially available with a range of features and functionality. Fluidized bed ALD has several advantages including: 1) the ability to operate between vacuum and ambient pressure,[107] 2) demonstrated scalability of the fluid bed design (e.g., fluidized catalytic cracking) provides the ability to produce larger quantities of catalyst, 3) solid particles are well mixed, 4) improved gas transport compared to a static bed, and 5) a very large ratio of powder to reactor wall surface area which allows for the efficient use of precursor by preventing its loss to the reactor walls.

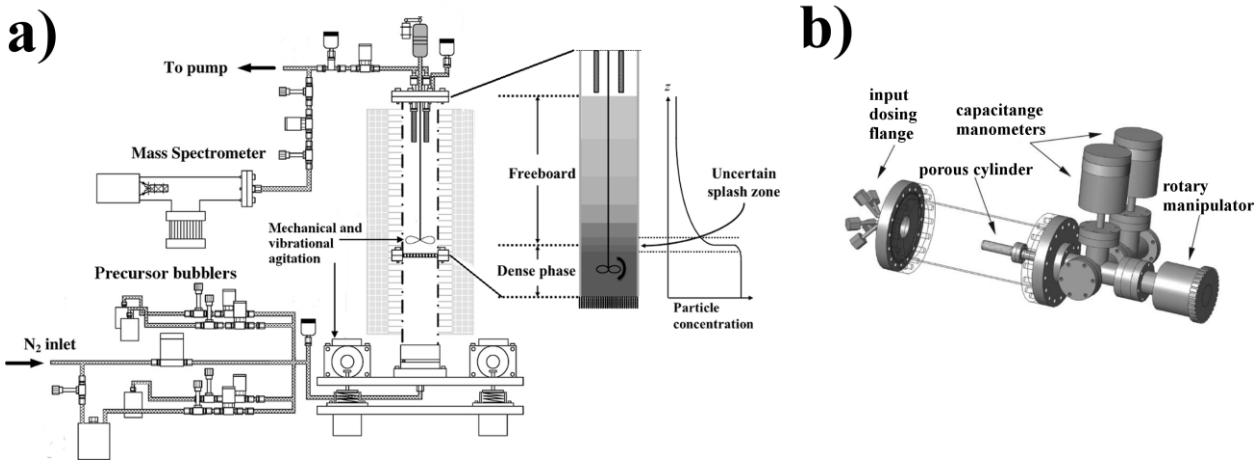

Figure 2.6. a) Schematic of a fluidized bed reactor for particle ALD. The reactor has an on-line in situ mass spectrometer, a stirring agitator, and vibration enhanced fluidization. The schematic on the right shows particle concentration as a function of height in the bed. b) Schematic of a rotary bed ALD reactor. Part a adapted with permission from Elsevier Copyright 2007.[108] Part b adapted with permission from AIP Publishing LLC Copyright 2007.[109]

A bed of solid particles is fluidized when the forces acting upwards on the bed due to the fluidization gas balances the force acting downward on the bed due to gravity. The critical minimum velocity V_{min} required for fluidization of small spherical particles is given by Equation 3:[110]

3) $$V_{min} = \frac{g(\rho_p - \rho)D_p^2\varepsilon^3}{150\mu(1-\varepsilon)}$$

In Equation 3, V_{min} is the minimum fluidization velocity, g is the acceleration of gravity, ρ_p is the particle density, ρ is the gas density, D_p is the diameter of the particles, ε is the void fraction of the bed, and μ is the dynamic viscosity of the gas. As shown by Equation 3, the fluidization properties are strongly dependent on the particle diameter, density and porosity. The fluidization regime within the fluidized bed reactor changes with increasing flow rate from: static, to bubbling bed, to turbulent bed, to pneumatic transport bed (riser reactor). The only existing examples in the literature are ALD processes operated in the bubbling bed regime, in which the solids are continuously mixed and circulated throughout the bed while the gases pass through the bed. Two phases form in this bubbling bed reactor: an emulsion phase that contains the solids and some gases and a gaseous phase that forms bubbles. The bubbles coalesce and grow as they travel up the reactor bed. The amount of gases that are in the bubble versus the emulsion phase depends on how high above the minimum fluidization velocity the bed operates. Fluidization at this minimum velocity typically allows the reactor base pressures to increase up to the Torr scale as a lower limit rather than the milliTorr scale used in other types of reactors.[100] When gas transport through a fluidized bed is faster than through a packed bed, the possibility of particle agglomeration is reduced. The particles in the fluidized bed reactor are continuously circulated or well mixed,

so there is a uniform distribution between the particles and the gas. Additionally, as all of the precursor must pass through the fluidized powder bed, precursor usage efficiency can be greatly increased which has the practical implication of greatly reducing synthesis time and cost. Progress of the reaction can be monitored using in situ mass spectrometry to determine pulse and purge times to optimize deposition speed and precursor utilization.[111] Fluidization may also be aided by the addition of baffles, vibration of the bed, or by a rotating propeller.[111] Finally, it is important to note that particles typically have a dispersion of sizes, and this will influence the fluidization behavior.[111, 112] In addition, nanoparticles typically fluidize as larger highly porous aggregates, but the nanoparticles can shed and recombine between aggregates, which allows all of the individual particles to be coated.[113]

An alternative approach to the agitation of particles during ALD is in the use of rotary bed reactors (Figure).[31, 32, 102, 114, 115] In this approach, the powder is typically contained within a rotating cylindrical enclosure with porous walls through which the reactants diffuse. Remote plasma ALD has been demonstrated on powders in a variant rotary bed in which an RF coil on a rotating quartz tube is used to energize precursors before the gas reaches the powder. [31, 32] The remote plasma source allows the higher energy ions to recombine before impinging on the coating surface where their interaction can lead to defects. Note that while the rotary reactor is simpler than alternatives such fluidized bed ALD, it is also more likely to waste precursor due to bypassing of the substrate in the reactor.

A typical reactor design uses well-controlled valving to enable rapid and near-complete changes in the gas phase composition. Reactors are commonly operated at low pressures to facilitate mass transport of the gas phase with the flow rate and composition controlled through the use of mass flow controllers. While most reactors are operated at low pressure, atmospheric pressure reactors also exist.[116-118]

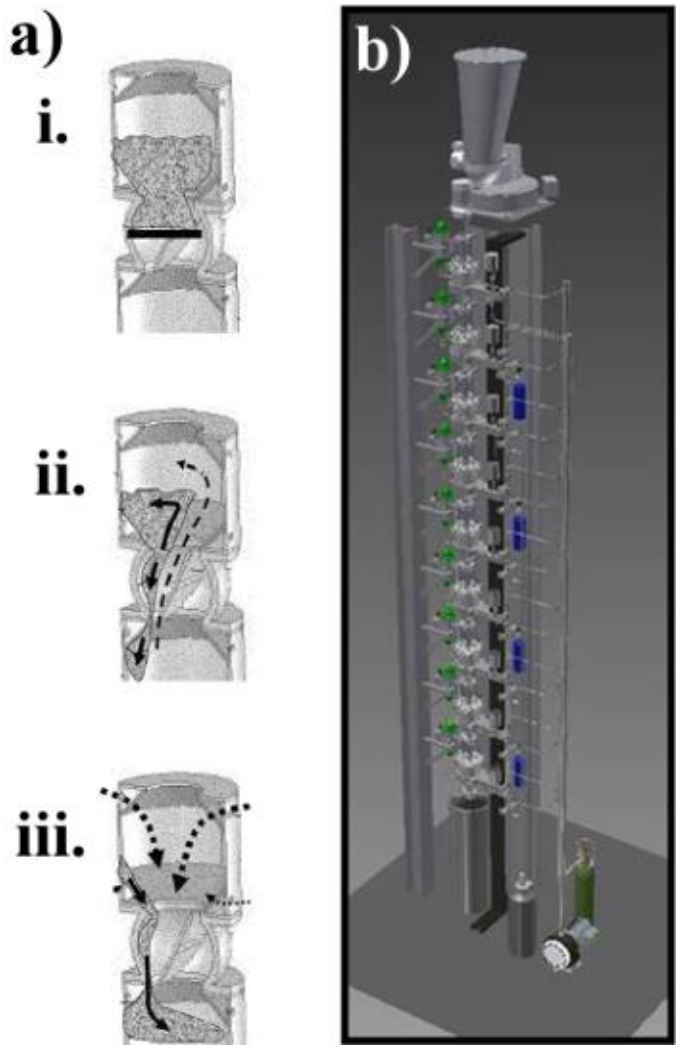

Figure 2.7. Schematic spatial ALD processes using powder reservoirs. a) Schematic of powder reservoir theory of operation i-iii. The powder to be coated is supported on a. b) CAD drawing of a powder reservoir type reactor. Adapted from King et al., and material available in the public domain. [119, 120]

The typical ALD process relies on temporal separation of the precursors through the inclusion of a purge stage between precursor pulses, with the substrate remaining fixed in space. An alternate approach to temporal ALD is spatial ALD, in which the precursors are dosed continuously in different zones of the reactor, while the substrate moves spatially through these regions.[121] Studies on spatial ALD have shown promising preliminary results in the scale up of wafer coating systems.[121] Designs of a spatial ALD powder system are shown

alongside the theory of operation of a semi-continuous spatial ALD reactor based on a valved reservoir concept (Figure).[119, 120] The powder is supported above a powder compliant valve while precursor vapor is filled into a reservoir below (Figure ai). The pressure in the powder reservoir is lower than in the precursor reservoir, so that when the valve is opened the precursor gasses escape upwards and the powder becomes a partially fluidized spouted bed (Figure aii). The precursor reacts with the powder as the powder falls into the reservoir below (Figure aiii). This design offers the advantage of semi-continuous processing and has a reported throughput of 12 to 15 kg per hour on the pilot scale. A CAD drawing of this semi-continuous reactor is shown in Figure b.[120] Another spatial ALD design has been proposed by a group at Delft.[122] In this configuration a powder is moved using pneumatic transport through a winding tube made up of reaction zones that alternate with empty or purged regions.

One of the primary hurdles for powder ALD is to ensure maximal usage of the gas phase precursor. Cost considerations and the large powder substrate–to-reactor surface area ratio achievable in a fluidized bed reactor, in combination with fact that scaled commercial processes for fluidization technology have already been developed; motivate the use of fluidized beds as a preferred technology. It is worth noting that the high cost of “rare” or custom precursors is not an uncommon hurdle in commercialization of new technologies. Appropriate large-scale applications for a precursor are required before large-scale production is pursued which can subsequently bring down the costs drastically. Also, while continuous processes generally have advantages with respect to capital and operating labor expenditures, the use of a fluidized bed ALD as a batch process in catalyst synthesis applications should not necessarily be considered prohibitory as industrial scale catalyst

manufacturing. Catalyst preparation is commonly done via batch synthesis, e.g., zeolite crystallization.

Implementation of ALD catalyst manufacturing on a commercial scale will require integration into the existing manufacturing infrastructure, execution at an economically feasible cost, detailed reactor design, and process intensification. Since catalyst manufacturing costs represent the summation of materials costs, capital expenditure, and labor, some promising routes to reducing total costs include increasing reactor throughput, increasing precursor utilization, and reducing net energy consumption during operation. The choice of the appropriate reactor requires the appropriate cost mitigation strategies with the required material specifications on a case–by-case basis. While ALD on powders at a commercial scale is still not realized, the advances presented above are expanding the set of options for technology development.

A broad range of ALD reactor designs exist and new designs continue to emerge.[123, 124] The implementation of ALD for new applications leads to innovation in reactor configurations. Challenges, such as scalability and deposition on high surface area powdered substrates, have in part expanded the breadth of this technology.

2.2 Overview of Catalysis

A catalyst is any material or chemical that accelerates the rate of a desired chemical reaction but remains unchanged after catalytic action.[125] Catalysts reduce the energetic barriers to specific, desired reaction pathways, and affect the selectivity and rate of a reaction. The majority of modern industries use catalysis including chemical, pharmaceutical, healthcare, food, agriculture, and environmental remediation. At modest estimation, approximately one third of the planetary GDP depends on catalysis.[126]

A heterogeneous catalyst is a solid that acts on chemicals that are in the gaseous or liquid phase. While more limited in terms of the range of methodologies for chemical synthesis than homogeneous catalysts, heterogeneous catalysts are desirable due to their superior handling and reusability. The dissimilarity of solid and liquid or gas phases allows the catalyst to be easily separated from the reaction mixture, leading to reusability and economical attractiveness. They are generally metal oxides, metal halides or metals, which can make up the entirety of the catalyst powder, or a catalyst can be deposited on a support, which acts as a high surface area scaffolding for the catalyst. Synthetic approaches for the production of catalysts include impregnation, ion exchange, and precipitation, which are all well established.

Chemical reactants will physically or chemically adsorb to the surface of a solid catalyst, undergo chemical transformation, and then desorb, leaving the catalyst surface. The interaction between a reactant and a catalysts creates a low-energy reaction intermediate, facilitating formation of the desired product.

2.3 Electrochemistry and Electrolytic Water Splitting

Electrocatalysts differs from conventional catalysis in that the presence of the electric field reduces the activation energy of kinetic barriers to desired reactions, and that reactions all involve the reduction or oxidation of chemical reactants to produce the desired reaction products.

Electrochemical testing is typically performed in a three-electrode cell, comprising positive and negative electrodes, and also a third electrode with known reduction potential that acts as a reference.[127] The third electrode is necessary due to difficulties maintaining constant electrode potential while passing a current. The most straightforward electrochemical test is linear sweep voltammetry, in which the current is monitored as a

function of a constant voltage sweep starting at a potential at which no reaction occurs. This results in a polarization curve, which shows the electrocatalytic activity of an electrode. A variety of other electrochemical characterization exists, including Tafel analysis, which sheds insight into the number electrons transferred in a reaction, and electrochemical impedance spectroscopy, which models an electrochemical cell as equivalent circuit elements.[127]

Modern day use of hydrogen is primarily based in the chemical industry, but much research is towards the use of hydrogen as an alternative fuel. Approaches to the production of hydrogen include chemical reforming of common industrial feedstocks such as hydrocarbons, sulfur and ammonia, and various approaches to water splitting. Water splitting by electrolysis ($2H_2O(l) \rightarrow 2H_2(g) + O_2(g)$, ΔE = 1.23 V) is an electrochemical technique for the generation of hydrogen and oxygen from water. The formation of H_2 and O_2 in water splitting occur on opposite electrodes, requiring each to have its own specific electrocatalyst.

The water splitting reaction typically occurs in highly corrosive environments (high and low pH, high electrical bias) which provide significant stability challenges in applications such as alkaline water electrolysis cells, proton exchange membranes, and solid oxide electrolysis cells that are commonly used.[128]

2.4 Li^+ ion batteries

A battery is an electrochemical cell that acts as a power supply by generating a flow of electrons across an external load. Electrons travel from anode to cathode outside of the cell, while Li^+ cations move from anode to cathode within the electrochemical cell (Figure 2.8). Li^+ transports between the electrodes through an electrolyte such as a dimethyl carbonate/ethyl carbonate mixture containing a Li salt, such as $LiPF_6$.[129] The chemical potential of lithium in the anode is higher than in the cathode, so the most energetically

favorable state is the discharged state with the Li in the cathode. The difference in electrode chemical potentials is responsible for the battery voltage according to Equation 4:[129]

$$4) \qquad V_{OC} = \frac{\left(\mu_{Li}^{anode} - \mu_{Li}^{cathode}\right)}{nF}$$

where V_{OC} is the open circuit potential of the battery, μ_{Li}^{anode} is the chemical potential of Li in the anode, $\mu_{Li}^{cathode}$ is the chemical potential of Li in the cathode, n is the number electrons involved in the reaction, which in this case is one, and F is Faraday's constant.

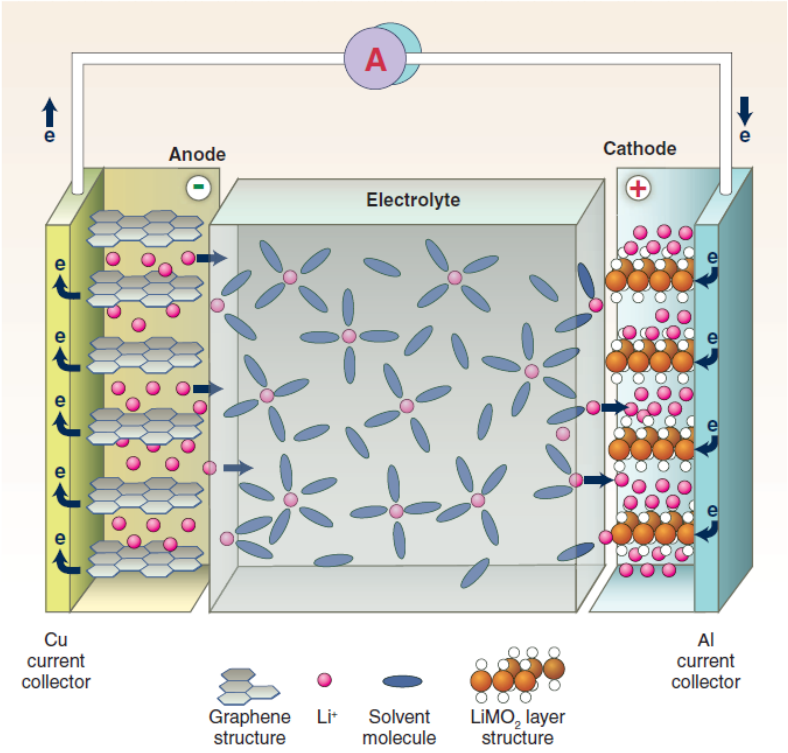

Figure 2.8. Representative drawing of a lithium ion battery (LIB), in which Li^+ ions pass from a graphite anode to a $LiMO_2$ anode, while electrons travel through a load. Reprinted with permission from Science, AAAS. [130]

A primary lithium ion battery (LIB) is designed for a single discharge, while a secondary LIB is designed for multiple charge/discharge cycles. After a secondary LIB is discharged, an externally applied bias can be used to drive cations back to the anode to

perform charging. Charging a cell in this manner allows it to be used as a rechargeable power source.

The charging process is not perfectly reversible, and LIB charge capacity and open circuit voltage degrade with each successive discharge. This degradation is caused by ionic disorder within the anode and cathode materials, increased cell impedance, and dissolution of electrode materials.[129] Improvement of the cycle-lifetime of common battery materials by addressing these degradation issues is one of the major thrusts of LIB research today.[129]

The electrochemical properties of the electrolytes, the electrodes and their compatibility must be considered carefully when designing a LIB. For example, the redox potentials or chemical potentials of the electrodes dictate the open circuit potential of the LIB through Equation 4. Development of electrodes that lead to higher voltages is an important research direction,[131-133] however with higher voltages new problems arise. Electrochemical stability of the electrolyte is a key issue in high voltage batteries, since electrolyte decomposition is a major path of LIB degradation.[129] An "electrolyte window" describes the safe operating voltage range in which an electrolyte does not undergo significant decomposition. If a battery is operated outside the electrolyte window, a layer of decomposed electrolyte will form on the electrode surface. This decomposed electrolyte is often called the solid electrolyte interphase or SEI layer, although this is a simplification of the complex SEI formation processes. The SEI creates states for the Li that are intermediary to the limits of the electrolyte window and the electrode potential.[129] SEI layer typically possesses high impedance, and its formation can further accelerate other cycle-lifetime degradation pathways.

In the case of LIBs, a $LiCoO_2$ cathode with a graphite anode is presently the most common configuration, and has been in use commercially since 1991. The $LiCoO_2$ cathode is

effective because of the high electron affinity of the Co(IV)/Co(III) redox couple, and undergoes the following reaction upon charging:

5) $$LiCoO_2 \rightarrow Li_{1-x}CoO_2 + Li_x^+ + e_x^-$$

This reaction remains reversible for x < 0.5, while beyond x = 0.5 the reaction becomes irreversible.[129] This change in reaction reversibility is due to a phase transformation to cobalt oxide phases, or cationic disordering which leads to metal ions occupying the crystal sites that were previously available to Li^+ ions.[134]

Several cathode materials exist with the $LiMO_2$ composition, in which M is any transition metal. In a notable example where M = Mn, the use of $LiMnO_2$ leads to a higher charge capacity. $LiMnO_2$ has not found widespread success due to the ease of dissolution of Mn^{2+} ions from the cathode crystal lattice, leading to their solvation into the electrolyte and degradation of the cathode structure. The formation of a more complex oxide achieved through mixing Mn with the more stable Ni, Co or both Ni and Co, to form $LiNi_xMn_yCo_{1-x-y}O_2$ (NMC), mitigates this effect.[50, 135, 136] Two common phases of lithium metal oxides are layered and spinel. Both structures are susceptible to cationic disordering and dissolution, but the layered structure has a higher charge capacity. For example, the layered structure of $LiMnO_2$ has an improved charge capacity of 200 mAh g^{-1} compared to 130 mAh g^{-1} for the $LiMn_2O_4$ spinel.[52] The layered structure allows for Li^+ intercalation into the two-dimensional planes between layers.

Table 2.2. Tabulated energy and charge capacity for typical cathode materials. Values for $LiMO_2$ type materials are for the layered compound, not the spinel. Charge capacities are for battery operation in the reversible regime.

Material	**Energy vs Li (eV)**	**Charge Capacity ($mAhg^{-1}$)**
$LiCoO_2$	4.0[129]	130[52]
$LiFePO_4$	3.45[129]	170[137]
$LiMnO_2$	4.0[129]	200[52]
$LiNi_{1/3}Mn_{1/3}Co_{1/3}O_2$	3.7[138]	170[138]

Several other cathodes are described in the battery literature that are beyond the discussion of this overview. It is worth noting that the lower voltage, but stable $LiFePO_4$ has enjoyed success in high power applications such as in power tools and electric vehicles.[137] Additionally, next generation electrodes such as lithium-air and lithium-sulfur have excellent prospects.[55]

LIB electrolytes are ion-conducting salts dissolved in organic carbonate solutions. Salt and solution both decompose to form a SEI layer composed of organic carbonate, Li_2CO_3 and LiF decomposition products, which coat the electrode surface.[139, 140] The SEI coating adds to cell impedance and traps Li through the formation of Li species such as Li_2CO_3 and LiF. Increased impedance in the cell causes a voltage gradient across the cell, sometimes referred to as an "IR drop" in reference to Ohms law: where $V = IR_{SEI}$; the voltage drop equals current times resistance of the SEI layer. This voltage drop in turn reduces the amount of power accessible from the cell.

Organic carbonates undergo oxidative decomposition to form the organic component of the SEI via electron transfer to the carbonyl carbon.[141] The common electrolyte salt, $LiPF_6$, can decompose to form HF, which etches battery components and forms LiF.[139, 140] LiF is a poor lithium conductor, and adds to the cell impedance, reducing available power. These and

other undesirable reactions occur between the electrode surface and the electrolyte during LIB operation. Surface-electrolyte reactions are not fully understood and their elucidation will help develop the fundamental scientific understanding of LIB operation. [59]

The anodic SEI is much more prominent in LIB research, and its existence is important to stabilizing the commonly used graphitic anode.[142, 143] The cathodic SEI has been linked with battery degradation though it is not clearly understood whether material comprising the SEI formed at the anode and then migrated to the cathode plays a more significant role than SEI formed on the cathode.[144, 145] Despite this ambiguity, it has been shown that reduction of cathodic SEI due to cathode coating can be correlated to improvements in battery performance in terms of both rate performance and cycle lifetime performance.[144, 145] As a result, formation of electrode coating layers has become a promising approach to improving the performance of layered $LiMO_2$ cathode materials and to other LIB components.[144, 146, 147]

Among the more successful electrode coatings are resistive materials such as SiO_2, Al_2O_3 and ZrO_2. The thickness of resistive coatings plays an important role, even at the nm scale, as added impedance to a cell will affect the accessible power.[146, 148] ALD is well suited to form these coating layers due to its ability to deposit ultrathin films with excellent conformality regardless of substrate morphology.

2.5 References

1. Somorjai, G. A.; Li, Y., Introduction to Surface Chemistry and Catalysis. In Wiley; 2 edition: 2010.

2. Zangwill, A., *Physics at Surfaces*. Cambridge University Press: 1992.

3. Puurunen, R. L., Surface chemistry of atomic layer deposition: A case study for the trimethylaluminum/water process. *Journal of Applied Physics* **2005,** 97, (12), 52.

4. Elam, J. W.; Libera, J. A.; Huynh, T. H.; Feng, H.; Pellin, M. J., Atomic Layer Deposition or Aluminum Oxide in Mesoporous Silica Gel. *Journal of Physical Chemistry C* **2010,** 114, (41), 17286-17292.

5. Detavernier, C.; Dendooven, J.; Sree, S. P.; Ludwig, K. F.; Martens, J. A., Tailoring nanoporous materials by atomic layer deposition. *Chemical Society Reviews* **2011,** 40, (11), 5242-5253.

6. Xinye, L.; Ramanathan, S.; Longdergan, A.; Srivastava, A.; Lee, E.; Seidel, T. E.; Barton, J. T.; Dawen, P.; Gordon, R. G., ALD of hafnium oxide thin films from Tetrakis(ethylmethylamino)hafnium and ozone. *J. Electrochem. Soc.* **2005,** 152, (3), G213-G219.

7. Jung, Y. S.; Cavanagh, A. S.; Dillon, A. C.; Groner, M. D.; George, S. M.; Lee, S. H., Enhanced Stability of LiCoO2 Cathodes in Lithium-Ion Batteries Using Surface Modification by Atomic Layer Deposition. *J. Electrochem. Soc.* **2010,** 157, (1), A75-A81.

8. Jackson, D. H. K.; Dunn, B. A.; Guan, Y.; Kuech, T. F., Tungsten hexacarbonyl and hydrogen peroxide as precursors for the growth of tungsten oxide thin films on titania nanoparticles. *AICHE J.* **2014,** 60, (4), 1278-1286.

9. Elam, J. W.; Schuisky, M.; Ferguson, J. D.; George, S. M., Surface chemistry and film growth during TiN atomic layer deposition using TDMAT and NH3. *Thin Solid Films* **2003,** 436, (2), 145-156.

10. Rai, V. R.; Agarwal, S., Mechanism of Self-catalytic Atomic Layer Deposition of Silicon Dioxide Using 3-Aminopropyl Triethoxysilane, Water, and Ozone. *Chem. Mater.* **2011,** 23, (9), 2312-2316.

11. Hicks, J. C.; Dabestani, R.; Buchanan, A. C., III; Jones, C. W., Spacing and site isolation of amine groups in 3-aminopropyl-grafted silica materials: The role of protecting groups. *Chemistry of Materials* **2006,** 18, (21), 5022-5032.

12. Putkonen, M.; Nieminen, M.; Niinisto, L., Magnesium aluminate thin films by atomic layer deposition from organometallic precursors and water. *Thin Solid Films* **2004,** 466, (1-2), 103-107.

13. O'Neill, B. J.; Sener, C.; Jackson, D. H. K.; Kuech, T. F.; Dumesic, J. A., Control of Thickness and Chemical Properties of Atomic Layer Deposition Overcoats for Stabilizing Cu/γ-Al2O3 Catalysts. *ChemSusChem* **2014,** 7, (12), 3247-3251.

14. Ferguson, J. D.; Smith, E. R.; Weimer, A. W.; George, S. M., ALD of SiO_2 at room temperature using TEOS and H_2O with NH_3 as the catalyst. *J. Electrochem. Soc.* **2004,** 151, (8), G528-G535.

15. Jackson, D. H. K.; Wang, D.; Gallo, J. M. R.; Crisci, A. J.; Scott, S. L.; Dumesic, J. A.; Kuech, T. F., Amine Catalyzed Atomic Layer Deposition of (3-Mercaptopropyl)trimethoxysilane for the Production of Heterogeneous Sulfonic Acid Catalysts. *Chem. Mater.* **2013,** 25, (19), 3844-3851.

16. Klaus, J. W.; George, S. M., Atomic layer deposition of SiO_2 at room temperature using NH_3-catalyzed sequential surface reactions. *Surf. Sci.* **2000,** 447, (1-3), 81-90.

17. Klaus, J. W.; Sneh, O.; Ott, A. W.; George, S. M., Atomic layer deposition of SiO_2 using catalyzed and uncatalyzed self-limiting surface reactions. *Surf. Rev. Lett.* **1999,** 6, (3-4), 435-448.

18. Klaus, J. W.; Sneh, O.; George, S. M., Growth of SiO2 at room temperature with the use of catalyzed sequential half-reactions. *Science* **1997,** 278, (5345), 1934-1936.

19. Du, Y.; Du, X.; George, S. M., Mechanism of pyridine-catalyzed SiO_2 atomic layer deposition studied by Fourier transform infrared spectroscopy. *J. Phys. Chem. C* **2007,** 111, (1), 219-226.

20. Du, Y.; Du, X.; George, S. M., SiO2 film growth at low temperatures by catalyzed atomic layer deposition in a viscous flow reactor. *Thin Solid Films* **2005,** 491, (1-2), 43-53.

21. Profijt, H. B.; Potts, S. E.; van de Sanden, M. C. M.; Kessels, W. M. M., Plasma-Assisted Atomic Layer Deposition: Basics, Opportunities, and Challenges. *J. Vac. Sci. Technol., A* **2011,** 29, (5).

22. Van Bui, H.; Kovalgin, A. Y.; Aarnink, A. A. I.; Wolters, R. A. M., Hot-Wire Generated Atomic Hydrogen and its Impact on Thermal ALD in $TiCl_4/NH_3$ System. *ECS J. Solid State Sci. Technol.* **2013,** 2, (4), P149-P155.

23. Shimizu, H.; Sakoda, K.; Momose, T.; Koshi, M.; Shimogaki, Y., Hot-wire-assisted atomic layer deposition of a high quality cobalt film using cobaltocene: Elementary reaction analysis on NHx radical formation. *J. Vac. Sci. Technol., A* **2012,** 30, (1).

24. Yuan, G. J.; Shimizu, H.; Momose, T.; Shimogaki, Y., Kinetic study on hot-wire-assisted atomic layer deposition of nickel thin films. *J. Vac. Sci. Technol., A* **2014,** 32, (1), 7.

25. Yuan, G.; Shimizu, H.; Momose, T.; Shimogaki, Y., Role of NH_3 feeding period to realize high-quality nickel films by hot-wire-assisted atomic layer deposition. *Microelectron. Eng.* **2014,** 120, 230-234.

26. Kim, J. B.; Kwon, D. R.; Chakrabarti, K.; Lee, C.; Oh, K. Y.; Lee, J. H., Improvement in Al_2O_3 dielectric behavior by using ozone as an oxidant for the atomic layer deposition technique. *J. Appl. Phys.* **2002,** 92, (11), 6739-6742.

27. Niinisto, L.; Ritala, M.; Leskela, M., Synthesis of oxide thin films and overlayers by atomic layer epitaxy for advanced applications. *J. Mater. Sci. Eng. B* **1996,** 41, (1), 23-29.

28. Goldstein, D. N.; McCormick, J. A.; George, S. M., Al_2O_3 Atomic Layer Deposition with Trimethylaluminum and Ozone Studied by in Situ Transmission FTIR Spectroscopy and Quadrupole Mass Spectrometry. *J. Phys. Chem. C* **2008,** 112, (49), 19530-19539.

29. Potts, S. E.; Kessels, W. M. M., Energy-enhanced atomic layer deposition for more process and precursor versatility. *Coord. Chem. Rev.* **2013,** 257, (23-24), 3254-3270.

30. Kim, S. K.; Hwang, C. S.; Park, S. H. K.; Yun, S. J., Comparison between ZnO films grown by atomic layer deposition using H2O or O-3 as oxidant. *Thin Solid Films* **2005,** 478, (1-2), 103-108.

31. Longrie, D.; Deduytsche, D.; Haemers, J.; Driesen, K.; Detavernier, C., A rotary reactor for thermal and plasma-enhanced atomic layer deposition on powders and small objects. *Surf. Coat. Technol.* **2012,** 213, 183-191.

32. Longrie, D.; Deduytsche, D.; Haemers, J.; Smet, P. F.; Driesen, K.; Detavernier, C., Thermal and Plasma-Enhanced Atomic Layer Deposition of TiN Using TDMAT and NH_3 on Particles Agitated in a Rotary Reactor. *ACS Appl. Mater. Interfaces* **2014,** 6, (10), 7316-7324.

33. Liu, X. Y.; Gu, Y. Q.; Huang, J. G., Hierarchical, Titania-Coated, Carbon Nanofibrous Material Derived from a Natural Cellulosic Substance. *Chem.-Eur. J.* **2010,** 16, (26), 7730-7740.

34. Gong, B.; Kim, D. H.; Parsons, G. N., Mesoporous Metal Oxides by Vapor Infiltration and Atomic Layer Deposition on Ordered Surfactant Polymer Films. *Langmuir* **2012,** 28, (32), 11915-11922.

35. Kovger, J.; Naujokaitis, A.; Niaura, G.; Juodkazyte, J.; Valusis, G.; Jagminas, A., Research on Hydrothermal Decoration of TiO2 Nanotube Films with Nanoplatelet MoS2 Species. *Nanomaterials and Nanotechnology* **2016,** 6.

36. Sree, S. P.; Dendooven, J.; Jammaer, J.; Masschaele, K.; Deduytsche, D.; D'Haen, J.; Kirschhock, C. E. A.; Martens, J. A.; Detavernier, C., Anisotropic Atomic Layer Deposition Profiles of TiO_2 in Hierarchical Silica Material with Multiple Porosity. *Chem. Mater.* **2012,** 24, (14), 2775-2780.

37. Pagán-Torres, Y. J.; Gallo, J. M. R.; Wang, D.; Pham, H. N.; Libera, J. A.; Marshall, C. L.; Elam, J. W.; Datye, A. K.; Dumesic, J. A., Synthesis of Highly Ordered Hydrothermally Stable Mesoporous Niobia Catalysts by Atomic Layer Deposition. *ACS Catal.* **2011,** 1, (10), 1234-1245.

38. Elam, J. W.; Libera, J. A.; Huynh, T. H.; Feng, H.; Pellin, M. J., Atomic Layer Deposition or Aluminum Oxide in Mesoporous Silica Gel. *J. Phys. Chem. C* **2010,** 114, (41), 17286-17292.

39. Groner, M. D.; Fabreguette, F. H.; Elam, J. W.; George, S. M., Low-temperature Al2O3 atomic layer deposition. *Chemistry of Materials* **2004,** 16, (4), 639-645.

40. Verheyen, E.; Sree, S. P.; Thomas, K.; Dendooven, J.; De Prins, M.; Vanbutsele, G.; Breynaert, E.; Gilson, J. P.; Kirschhock, C. E. A.; Detavernier, C.; Martens, J. A., Catalytic activation of OKO zeolite with intersecting pores of 10-and 12-membered rings using atomic layer deposition of aluminium. *Chem. Commun.* **2014,** 50, (35), 4610-4612.

41. Luan, X. N.; Guan, D. S.; Wang, Y., Enhancing High-Rate and Elevated-Temperature Performances of Nano-Sized and Micron-Sized LiMn2O4 in Lithium-Ion Batteries with Ultrathin Surface Coatings. *Journal of Nanoscience and Nanotechnology* **2012,** 12, (9), 7113-7120.

42. Sree, S. P.; Dendooven, J.; Koranyi, T. I.; Vanbutsele, G.; Houthoofd, K.; Deduytsche, D.; Detavernier, C.; Martens, J. A., Aluminium atomic layer deposition applied to mesoporous zeolites for acid catalytic activity enhancement. *Catal. Sci. Technol.* **2011,** 1, (2), 218-221.

43. Mackus, A. J. M.; Thissen, N. F. W.; Mulders, J. J. L.; Trompenaars, P. H. F.; Verheijen, M. A.; Bol, A. A.; Kessels, W. M. M., Direct-Write Atomic Layer Deposition of High-Quality Pt Nanostructures: Selective Growth Conditions and Seed Layer Requirements. *J. Phys. Chem. C* **2013,** 117, (20), 10788-10798.

44. Selvaraj, S. K.; Parulekar, J.; Takoudis, C. G., Selective atomic layer deposition of zirconia on copper patterned silicon substrates using ethanol as oxygen source as well as copper reductant. *J. Vac. Sci. Technol. A* **2014,** 32, (1), 4.

45. Park, K. J.; Doub, J. M.; Gougousi, T.; Parsons, G. N., Microcontact patterning of ruthenium gate electrodes by selective area atomic layer deposition. *Appl. Phys. Lett.* **2005,** 86, (5).

46. Sinha, A.; Hess, D. W.; Henderson, C. L., Transport behavior of atomic layer deposition precursors through polymer masking layers: Influence on area selective atomic layer deposition. *J. Vac. Sci. Technol., B* **2007,** 25, (5), 1721-1728.

47. Sinha, A.; Hess, D. W.; Henderson, C. L., Area selective atomic layer, deposition of titanium dioxide: Effect of precursor chemistry. *J. Vac. Sci. Technol., B* **2006,** 24, (6), 2523-2532.

48. Yan, M.; Koide, Y.; Babcock, J. R.; Markworth, P. R.; Belot, J. A.; Marks, T. J.; Chang, R. P. H., Selective-area atomic layer epitaxy growth of ZnO features on soft lithography-patterned substrates. *Appl. Phys. Lett.* **2001,** 79, (11), 1709-1711.

49. Lim, J. W.; Yun, S. J.; Lee, J. H., Characteristics of TiO2 films prepared by ALD with and without plasma. *Electrochemical and Solid State Letters* **2004,** 7, (11), F73-F76.

50. Hwang, B. J.; Tsai, Y. W.; Carlier, D.; Ceder, G., A combined computational/experimental study on LiNi1/3Co1/3Mn1/3O2. *Chemistry of Materials* **2003,** 15, (19), 3676-3682.

51. Tahir, M. N.; Sahoo, J. K.; Hoshyargar, F.; Tremel, W., Growth Mechanism and Surface Functionalization of Metal Chalcogenides Nanostructures. *Metal Chalcogenide Nanostructures for Renewable Energy Applications* **2015**, 83-121.

52. Bruce, P. G.; Armstrong, A. R.; Gitzendanner, R. L., New intercalation compounds for lithium batteries: layered LiMnO2. *Journal of Materials Chemistry* **1999,** 9, (1), 193-198.

53. Riley, L. A.; Van Ana, S.; Cavanagh, A. S.; Yan, Y. F.; George, S. M.; Liu, P.; Dillon, A. C.; Lee, S. H., Electrochemical effects of ALD surface modification on combustion synthesized LiNi1/3Mn1/3Co1/3O2 as a layered-cathode material. *Journal of Power Sources* **2011,** 196, (6), 3317-3324.

54. Moffitt, C. E.; Chen, B.; Wieliczka, D. M.; Kruger, M. B., XPS comparison between nanocrystalline gamma-alumina and a new high pressure polymorph. *Solid State Communications* **2000,** 116, (11), 631-636.

55. Bruce, P. G.; Freunberger, S. A.; Hardwick, L. J.; Tarascon, J.-M., Li-O-2 and Li-S batteries with high energy storage. *Nature Materials* **2012,** 11, (1), 19-29.

56. Zhao, J. Q.; Qu, G. Y.; Flake, J. C.; Wang, Y., Low temperature preparation of crystalline ZrO2 coatings for improved elevated-temperature performances of Li-ion battery cathodes. *Chemical Communications* **2012,** 48, (65), 8108-8110.

57. McGuire, G. E.; Schweitz.Gk; Carlson, T. A., Study of Core Electron Binding-Energies in Some Group IIIA, VB, and VIB Compounds. *Inorganic Chemistry* **1973,** 12, (10), 2450-2453.

58. Kim, E.; Vaynzof, Y.; Sepe, A.; Guldin, S.; Scherer, M.; Cunha, P.; Roth, S. V.; Steiner, U., Gyroid-Structured 3D ZnO Networks Made by Atomic Layer Deposition. *Adv. Funct. Mater.* **2014,** 24, (6), 863-872.

59. Gong, B.; Peng, Q.; Parsons, G. N., Conformal Organic-Inorganic Hybrid Network Polymer Thin Films by Molecular Layer Deposition using Trimethylaluminum and Glycidol. *J. Phys. Chem. B* **2011,** 115, (37), 11028-11028.

60. Liang, X. H.; Yu, M.; Li, J. H.; Jiang, Y. B.; Weimer, A. W., Ultra-thin microporous-mesoporous metal oxide films prepared by molecular layer deposition (MLD). *Chemical Communications* **2009**, (46), 7140-7142.

61. Liang, X. H.; Yu, M.; Li, J. H.; Jiang, Y. B.; Weimer, A. W., Ultra-thin microporous-mesoporous metal oxide films prepared by molecular layer deposition (MLD). *Chem. Commun.* **2009**, (46), 7140-7142.

62. Rahtu, A.; Ritala, M.; Leskela, M., Atomic layer deposition of zirconium titanium oxide from titanium isopropoxide and zirconium chloride. *Chem. Mater.* **2001,** 13, (5), 1528-1532.

63. Brahim, C.; Chauveau, F.; Ringuede, A.; Cassir, M.; Putkonen, M.; Niinistoe, L., ZrO_2-In_2O_3 thin layers with gradual ionic to electronic composition synthesized by atomic layer deposition for SOFC applications. *J. Mater. Chem.* **2009,** 19, (6), 760-766.

64. Kasikov, A.; Aarik, J.; Mandar, H.; Moppel, M.; Pars, M.; Uustare, T., Refractive index gradients in TiO_2 thin films grown by atomic layer deposition. *J. Phys. D Appl. Phys.* **2006,** 39, (1), 54-60.

65. Elers, K. E.; Saanila, V.; Li, W. M.; Soininen, P. J.; Kostamo, J. T.; Haukka, S.; Juhanoja, J.; Besling, W. F. A., Atomic layer deposition of WxN/TiN and WNxCy/TiN nanolaminates. *Thin Solid Films* **2003,** 434, (1-2), 94-99.

66. Elam, J. W.; Sechrist, Z. A.; George, S. M., ZnO/Al_2O_3 nanolaminates fabricated by atomic layer deposition: growth and surface roughness measurements. *Thin Solid Films* **2002,** 414, (1), 43-55.

67. Winkler, H.; Rueger, R. TiO_2 thin films and doped TiO_2 nanolaminates, their structure and its effect on their photocatalytic propertiesCoated phosphor particles with refractive index adaption. 2015.

68. Zhong, L. J.; Daniel, W. L.; Zhang, Z. H.; Campbell, S. A.; Gladfelter, W. L., Atomic layer deposition, characterization, and dielectric properties of HfO_2/SiO_2 nanolaminates and comparisons with their homogeneous mixtures. *Chem. Vap. Deposition* **2006,** 12, (2-3), 143-150.

69. Kibsgaard, J.; Clausen, B. S.; Topsoe, H.; Laegsgaard, E.; Lauritsen, J. V.; Besenbacher, F., Scanning tunneling microscopy studies of TiO_2-supported hydrotreating catalysts: Anisotropic particle shapes by edge-specific MoS_2-support bonding. *Journal of Catalysis* **2009,** 263, (1), 98-103.

70. Masango, S. S.; Peng, L.; Marks, L. D.; Van Duyne, R. P.; Stair, P. C., Nucleation and Growth of Silver Nanoparticles by AB and ABC-Type Atomic Layer Deposition. *J. Phys. Chem. C* **2014,** 118, (31), 17655-17661.

71. Sugier, A.; E, F. 1978.

72. Nie, A.; Liu, J.; Li, Q.; Cheng, Y.; Dong, C.; Zhou, W.; Wang, P.; Wang, Q.; Yang, Y.; Zhu, Y.; Zeng, Y.; Wang, H., Epitaxial TiO_2/SnO_2 core-shell heterostructure by atomic layer deposition. *J. Mater. Chem.* **2012,** 22, (21), 10665-10671.

73. Vuori, H.; Silvennoinen, R. J.; Lindblad, M.; Osterholm, H.; Krause, A. O. I., Beta Zeolite-Supported Iridium Catalysts by Gas Phase Deposition. *Catalysis Letters* **2009,** 131, (1-2), 7-15.

74. Elers, K.-E., Suvi P.Saanila, Ville AnteroKaipio, Sari JohannaSoininen, Pekka Juha Deposition of transition metal carbides.

75. Wank, J. R.; George, S. M.; Weimer, A. W., Nanocoating individual cohesive boron nitride particles in a fluidized bed by ALD. *Powder Technol.* **2004,** 142, (1), 59-69.

76. Tiznado, H.; Zaera, F., Surface chemistry in the atomic layer deposition of TiN films from $TiCl_4$ and ammonia. *J. Phys. Chem. B* **2006,** 110, (27), 13491-13498.

77. Reijnen, L.; Meester, B.; Goossens, A.; Schoonman, J., Atomic layer deposition of Cu_xS for solar energy conversion. *Chem. Vap. Deposition* **2003,** 9, (1), 15-20.

78. Scharf, T. W.; Prasad, S. V.; Mayer, T. M.; Goeke, R. S.; Dugger, M. T., Atomic layer deposition of tungsten disulphide solid lubricant thin films. *J. Mater. Res.* **2004,** 19, (12), 3443-3446.

79. Sinsermsuksakul, P.; Heo, J.; Noh, W.; Hock, A. S.; Gordon, R. G., Atomic Layer Deposition of Tin Monosulfide Thin Films. *Adv. Energy Mater.* **2011,** 1, (6), 1116-1125.

80. Nagasawa, H.; Yamaguchi, Y., Atomic Level Epitaxy of 3C-SIC by Low-Pressure Vapor-Deposition with Alternating Gas-Supply. *Thin Solid Films* **1993,** 225, (1-2), 230-234.

81. Feng, H.; Libera, J. A.; Stair, P. C.; Miller, J. T.; Elam, J. W., Subnanometer Palladium Particles Synthesized by Atomic Layer Deposition. *ACS Catal.* **2011,** 1, (6), 665-673.

82. Aaltonen, T.; Ritala, M.; Tung, Y. L.; Chi, Y.; Arstila, K.; Meinander, K.; Leskela, M., Atomic layer deposition of noble metals: Exploration of the low limit of the deposition temperature. *J. Mater. Res.* **2004,** 19, (11), 3353-3358.

83. Kim, S. K.; Han, J. H.; Kim, G. H.; Hwang, C. S., Investigation on the Growth Initiation of Ru Thin Films by Atomic Layer Deposition. *Chem. Mater.* **2010,** 22, (9), 2850-2856.

84. Lu, J. L.; Elam, J. W.; Stair, P. C., Atomic layer deposition-Sequential self-limiting surface reactions for advanced catalyst "bottom-up" synthesis. *Surface Science Reports* **2016,** 71, (2), 410-472.

85. Elliott, S. D., Mechanism, Products, and Growth Rate of Atomic Layer Deposition of Noble Metals. *Langmuir* **2010,** 26, (12), 9179-9182.

86. Ritala, M.; Leskela, M.; Rauhala, E.; Haussalo, P., Atomic Layer Epitaxy Growth of Tin Thin-Films. *J. Electrochem. Soc.* **1995,** 142, (8), 2731-2737.

87. Puurunen, R. L.; Root, A.; Sarv, P.; Haukka, S.; Iiskola, E. I.; Lindblad, M.; Krause, A. O. I., Growth of aluminium nitride on porous silica by atomic layer chemical vapour deposition. *Appl. Surf. Sci.* **2000,** 165, (2-3), 193-202.

88. Liu, H.; Bertolet, D. C.; Rogers, J. W., Reactions of Trimethylaluminum and Ammonia on Alumina at 600-K - Surface Chemical Aspects of AlN Thin-Film Growth. *Surf. Sci.* **1995,** 340, (1-2), 88-100.

89. Bauer, E., Phaenomenologische Theorie der Kristallabscheidung an Oberflaechen I. In *Z. Kristallogr.*: 1958; Vol. 110, pp 374-394.

90. Gordon, R. G.; Hausmann, D.; Kim, E.; Shepard, J., A kinetic model for step coverage by atomic layer deposition in narrow holes or trenches. *Chemical Vapor Deposition* **2003,** 9, (2), 73-78.

91. Lu, J.; Fu, B.; Kung, M. C.; Xiao, G.; Elam, J. W.; Kung, H. H.; Stair, P. C., Coking- and Sintering-Resistant Palladium Catalysts Achieved Through Atomic Layer Deposition. *Science* **2012,** 335, (6073), 1205-1208.

92. Parsons, G. N.; Atanasov, S. E.; Dandley, E. C.; Devine, C. K.; Gong, B.; Jur, J. S.; Lee, K.; Oldham, C. J.; Peng, Q.; Spagnola, J. C.; Williams, P. S., Mechanisms and reactions during atomic layer deposition on polymers. *Coord. Chem. Rev.* **2013,** 257, (23-24), 3323-3331.

93. Liang, X.; King, D. M.; Groner, M. D.; Blackson, J. H.; Harris, J. D.; George, S. M.; Weimer, A. W., Barrier properties of polymer/alumina nanocomposite membranes fabricated by atomic layer deposition. *J. Membr. Sci.* **2008,** 322, (1), 105-112.

94. Kayaci, F.; Ozgit-Akgun, C.; Donmez, I.; Biyikli, N.; Uyar, T., Polymer-Inorganic Core-Shell Nanofibers by Electrospinning and Atomic Layer Deposition: Flexible Nylon-ZnO Core-Shell Nanofiber Mats and Their Photocatalytic Activity. *ACS Appl. Mater. Interfaces* **2012,** 4, (11), 6185-6194.

95. Korhonen, J. T.; Hiekkataipale, P.; Malm, J.; Karppinen, M.; Ikkala, O.; Ras, R. H. A., Inorganic Hollow Nanotube Aerogels by Atomic Layer Deposition onto Native Nanocellulose Templates. *ACS Nano* **2011,** 5, (3), 1967-1974.

96. George, S. M.; Lee, B. H.; Yoon, B.; Abdulagatov, A. I.; Hall, R. A., Metalcones: Hybrid Organic-Inorganic Films Fabricated Using Atomic and Molecular Layer Deposition Techniques. *J. Nanosci. Nanotechnol.* **2011,** 11, (9), 7948-7955.

97. Sundberg, P.; Karppinen, M., Organic and inorganic-organic thin film structures by molecular layer deposition: A review. *Beilstein J. Nanotechnol.* **2014,** 5, 1104-1136.

98. Dameron, A. A.; Seghete, D.; Burton, B. B.; Davidson, S. D.; Cavanagh, A. S.; Bertrand, J. A.; George, S. M., Molecular layer deposition of alucone polymer films using trimethylaluminum and ethylene glycol. *Chem. Mater.* **2008,** 20, (10), 3315-3326.

99. Abdulagatov, A. I.; Hall, R. A.; Sutherland, J. L.; Lee, B. H.; Cavanagh, A. S.; George, S. M., Molecular Layer Deposition of Titanicone Films using $TiCl_4$ and Ethylene Glycol or Glycerol: Growth and Properties. *Chem. Mater.* **2012,** 24, (15), 2854-2863.

100. Longrie, D.; Deduytsche, D.; Detavernier, C., Reactor concepts for atomic layer deposition on agitated particles: A review. *J. Vac. Sci. Technol., A* **2014,** 32, (1).

101. Libera, J. A.; Elam, J. W.; Pellin, M. J., Conformal ZnO coatings on high surface area silica gel using atomic layer deposition. *Thin Solid Films* **2008,** 516, (18), 6158-6166.

102. King, D. M.; Liang, X. H.; Weimer, A. W., Functionalization of fine particles using atomic and molecular layer deposition. *Powder Technol.* **2012,** 221, 13-25.

103. Gordon, R. G.; Hausmann, D.; Kim, E.; Shepard, J., A kinetic model for step coverage by atomic layer deposition in narrow holes or trenches. *Chem. Vap. Deposition* **2003,** 9, (2), 73-78.

104. Yanguas-Gil, A.; Elam, J. W., Self-Limited Reaction-Diffusion in Nanostructured Substrates: Surface Coverage Dynamics and Analytic Approximations to ALD Saturation Times. *Chem. Vap. Deposition* **2012,** 18, (1-3), 46-52.

105. Elam, J. W.; Groner, M. D.; George, S. M., Viscous flow reactor with quartz crystal microbalance for thin film growth by atomic layer deposition. *Review of Scientific Instruments* **2002,** 73, (8), 2981-2987.

106. Serp, P.; Kalck, P.; Feurer, R., Chemical vapor deposition methods for the controlled preparation of supported catalytic materials. *Chem. Rev.* **2002,** 102, (9), 3085-3128.

107. Santinis.C; Riess, J. G., Preparation of Monomethyl-Niobium(V) and Monomethyl-Tantalum(V) Halides and of Some of their Complexes. *Journal of the Chemical Society-Dalton Transactions* **1973**, (22), 2436-2440.

108. King, D. M.; Spencer, J. A.; Liang, X.; Hakim, L. F.; Weimer, A. W., Atomic layer deposition on particles using a fluidized bed reactor with in situ mass spectrometry. *Surface & Coatings Technology* **2007,** 201, (22-23), 9163-9171.

109. McCormick, J. A.; Cloutier, B. L.; Weimer, A. W.; George, S. M., Rotary reactor for atomic layer deposition on large quantities of nanoparticles. *Journal of Vacuum Science & Technology A* **2007,** 25, (1), 67-74.

110. McCabe, W.; Smith, J.; Harriott, P., Unit Operations of Chemical Engineering (7th Edition). In McGraw-Hill Science/Engineering/Math.

111. King, D. M.; Spencer, J. A., II; Liang, X.; Hakim, L. F.; Weimer, A. W., Atomic layer deposition on particles using a fluidized bed reactor with in situ mass spectrometry. *Surf. Coat. Technol.* **2007,** 201, (22-23), 9163-9171.

112. van Ommen, J. R.; Manuel Valverde, J.; Pfeffer, R., Fluidization of nanopowders: a review. *J. Nanopart. Res.* **2012,** 14, (3).

113. Hakim, L. F.; Portman, J. L.; Casper, M. D.; Weimer, A. W., Aggregation behavior of nanoparticles in fluidized beds. *Powder Technol.* **2005,** 160, (3), 149-160.

114. Samain, L.; Jaworski, A.; Eden, M.; Ladd, D. M.; Seo, D. K.; Garcia-Garcia, F. J.; Haussermann, U., Structural analysis of highly porous gamma-Al2O3. *Journal of Solid State Chemistry* **2014,** 217, 1-8.

115. Ma, Z.; Brown, S.; Howe, J. Y.; Overbury, S. H.; Dai, S., Surface modification of Au/TiO2 catalysts by SiO2 via atomic layer deposition. *J. Phys. Chem. C* **2008,** 112, (25), 9448-9457.

116. Beetstra, R.; Lafont, U.; Nijenhuis, J.; Kelder, E. M.; van Ommen, J. R., Atmospheric Pressure Process for Coating Particles Using Atomic Layer Deposition. *Chemical Vapor Deposition* **2009,** 15, (7-9), 227-233.

117. Goulas, A.; van Ommen, J. R., Atomic layer deposition of platinum clusters on titania nanoparticles at atmospheric pressure. *Journal of Materials Chemistry A* **2013,** 1, (15), 4647-4650.

118. Goulas, A.; van Ommen, J. R., Scalable Production of Nanostructured Particles using Atomic Layer Deposition. *Kona Powder and Particle Journal* **2014**, (31), 234-246.

119. King, D. M.; Weimer, A. W.; Lichty, P., Semi-Continuous Vapor Deposition Process for the Manufacture of Coated Particles. In US20110236575, 2011.

120. LLC, P. T., In http://www.pneumaticoat.com/production-ald.html.

121. Poodt, P.; Cameron, D. C.; Dickey, E.; George, S. M.; Kuznetsov, V.; Parsons, G. N.; Roozeboom, F.; Sundaram, G.; Vermeer, A., Spatial atomic layer deposition: A route towards further industrialization of atomic layer deposition. *J. Vac. Sci. Technol., A* **2012,** 30, (1).

122. Van Ommen, J. R., Apparatus and process for atomic or molecular layer deposition onto particles during pneumatic transport. In US 20120009343.

123. Poodt, P.; Cameron, D. C.; Dickey, E.; George, S. M.; Kuznetsov, V.; Parsons, G. N.; Roozeboom, F.; Sundaram, G.; Vermeer, A., Spatial atomic layer deposition: A route towards further industrialization of atomic layer deposition. *Journal of Vacuum Science & Technology A* **2012,** 30, (1).

124. Longrie, D.; Deduytsche, D.; Detavernier, C., Reactor concepts for atomic layer deposition on agitated particles: A review. *Journal of Vacuum Science & Technology A* **2014,** 32, (1).

125. Fogler, H. S., Elements of Chemical Reaction Engineering. In 2nd ed.; Prentice-Hall, Inc.: 1992; p 242.

126. Adams, C., Applied Catalysis: A Predictive Socioeconomic History. *Topics in Catalysis* **2009,** 52, (8), 924-934.

127. Bard, A. J.; Faulkner, L. R., *Electrochemical Methods: Fundamentals and Applications*. 2nd edition ed.; Wiley: 2000.

128. Holladay, J. D.; Hu, J.; King, D. L.; Wang, Y., An overview of hydrogen production technologies. *Catalysis Today* **2009,** 139, (4), 244-260.

129. Goodenough, J. B.; Kim, Y., Challenges for Rechargeable Li Batteries. *Chemistry of Materials* **2010,** 22, (3), 587-603.

130. Dunn, B.; Kamath, H.; Tarascon, J. M., Electrical Energy Storage for the Grid: A Battery of Choices. *Science* **2011,** 334, (6058), 928-935.

131. Liu, D.; Zhu, W.; Trottier, J.; Gagnon, C.; Barray, F.; Guerfi, A.; Mauger, A.; Groult, H.; Julien, C. M.; Goodenough, J. B.; Zaghi, K., Spinel materials for high-voltage cathodes in Li-ion batteries. *Rsc Advances* **2014,** 4, (1), 154-167.

132. Kraytsberg, A.; Ein-Eli, Y., Higher, Stronger, Better ... A Review of 5 Volt Cathode Materials for Advanced Lithium-Ion Batteries. *Advanced Energy Materials* **2012,** 2, (8), 922-939.

133. Johnson, C. S.; Li, N.; Lefief, C.; Thackeray, M. M., Anomalous capacity and cycling stability of $xLi_{(2)}MnO_{(3)*(1-x)}LiMO_2$ electrodes (M = Mn, Ni, Co) in lithium batteries at 50 degrees C. *Electrochemistry Communications* **2007,** 9, (4), 787-795.

134. Mizushima, K.; Jones, P. C.; Wiseman, P. J.; Goodenough, J. B., $Li_xCoO_{2\ (O\leq1)}$ - A New Cathode Material for Batteries of High-Energy Density. *Materials Research Bulletin* **1980,** 15, (6), 783-789.

135. Li, D. C.; Muta, T.; Zhang, L. Q.; Yoshio, M.; Noguchi, H., Effect of synthesis method on the electrochemical performance of $LiNi_{1/3}Mn_{1/3}Co_{1/3}O_2$. *Journal of Power Sources* **2004,** 132, (1-2), 150-155.

136. Zhang, L. Q.; Noguchi, H.; Yoshio, M., Synthesis and electrochemical properties of layered Li-Ni-Mn-O compounds. *Journal of Power Sources* **2002,** 110, (1), 57-64.

137. Chung, S. Y.; Bloking, J. T.; Chiang, Y. M., Electronically conductive phospho-olivines as lithium storage electrodes. *Nature Materials* **2002,** 1, (2), 123-128.

138. Croguennec, L.; Palacin, M. R., Recent Achievements on Inorganic Electrode Materials for Lithium-Ion Batteries. *Journal of the American Chemical Society* **2015,** 137, (9), 3140-3156.

139. Edstrom, K.; Gustafsson, T.; Thomas, J. O., The cathode-electrolyte interface in the Li-ion battery. *Electrochimica Acta* **2004,** 50, (2-3), 397-403.

140. Kawaguchi, T.; Shimada, K.; Ichitsubo, T.; Yagi, S.; Matsubara, E., Surface-layer formation by reductive decomposition of LiPF6 at relatively high potentials on negative electrodes in lithium ion batteries and its suppression. *Journal of Power Sources* **2014,** 271, 431-436.

141. Xu, K.; von Cresce, A., Interfacing electrolytes with electrodes in Li ion batteries. *Journal of Materials Chemistry* **2011,** 21, (27), 9849-9864.

142. Winter, M., The Solid Electrolyte Interphase - The Most Important and the Least Understood Solid Electrolyte in Rechargeable Li Batteries. *Zeitschrift Fur Physikalische Chemie-International Journal of Research in Physical Chemistry & Chemical Physics* **2009,** 223, (10-11), 1395-1406.

143. Arora, P.; White, R. E.; Doyle, M., Capacity fade mechanisms and side reactions in lithium-ion batteries. *Journal of the Electrochemical Society* **1998,** 145, (10), 3647-3667.

144. Chen, Z. H.; Qin, Y.; Amine, K.; Sun, Y. K., Role of surface coating on cathode materials for lithium-ion batteries. *Journal of Materials Chemistry* **2010,** 20, (36), 7606-7612.

145. Kim, J. W.; Travis, J. J.; Hu, E. Y.; Nam, K. W.; Kim, S. C.; Kang, C. S.; Woo, J. H.; Yang, X. Q.; George, S. M.; Oh, K. H.; Cho, S. J.; Lee, S. H., Unexpected high power performance of atomic layer deposition coated Li Ni1/3Mn1/3Co1/3 O-2 cathodes. *Journal of Power Sources* **2014,** 254, 190-197.

146. Li, C.; Zhang, H. P.; Fu, L. J.; Liu, H.; Wu, Y. P.; Ram, E.; Holze, R.; Wu, H. Q., Cathode materials modified by surface coating for lithium ion batteries. *Electrochimica Acta* **2006,** 51, (19), 3872-3883.

147. Fu, L. J.; Liu, H.; Li, C.; Wu, Y. P.; Rahm, E.; Holze, R.; Wu, H. Q., Surface modifications of electrode materials for lithium ion batteries. *Solid State Sciences* **2006,** 8, (2), 113-128.

148. Zhao, J. Q.; Wang, Y., Surface modifications of Li-ion battery electrodes with various ultrathin amphoteric oxide coatings for enhanced cycleability. *Journal of Solid State Electrochemistry* **2013,** 17, (4), 1049-1058.

3 Experimental Techniques

This section contains information regarding the experimental techniques used for study of ALD-coated particle based materials. The techniques covered here are separated into two sections. The first section covers the sample preparation techniques associated with powder samples, and the second covers the materials characterization techniques used in this study.

3.1 Powder preparation and treatment

3.1.1 Grinding and sieving

Powders received directly from a vendor may arrive as pellets that require further grinding with a mortar and pestle, which results in a broad range of particulate diameters. A narrow range of particle sizes is often desirable for an experiment, so that the ground pellets or powders with a broad particle size distribution may require further separation. Two-step sieving of powders allows for separation of particles by size yielding a more monodispersed size distribution. Only particles below a certain diameter pass through the mesh, the larger particles are retained above the mesh. Using two meshes allows for the separation of particles with an upper and lower size limit. The larger mesh size sieve is used first, and acts as an upper limit filter, and the larger diameter fraction is discarded. The smaller diameter fraction of this first separation is passed through the second, smaller mesh size sieve, which acts as a lower limit. The remaining upper fraction of the second sieving contains only particles within the desired upper and lower size limits.

3.1.2 Incipient wetness impregnation

Metal nanoparticles may be synthesized on a high surface area supports using a catalyst preparation technique termed incipient wetness impregnation. A metal precursor, such as a salt, is dissolved in an aqueous or organic solution. The solution has a volume matching the internal pore volume of the support, so that when all of the precursor solution is

absorbed by the powder, the powder begins to appear wet, and visual observation of the slurry may be used as an indicator of incipient wetness. The capillary action of the micropores of the support draws the solution fully into the pores. When the slurry containing the support particles reaches the point of incipient wetness, the catalyst is dried at elevated temperatures for a prolonged period, and then calcined at a higher temperature to drive formation of metal oxide nanoparticles from the precursors. A reduction using hydrogen is performed after calcination to reduce the metal oxide to its metallic form. In some cases where the metal nanoparticles are easily oxidized, a final passivation step is performed, in which dilute oxygen is used to form a thin passivating oxide on the surface of the metal nanoparticles. In the case of cobalt/carbon electrocatalysts, $Co(NO_3)_2 \cdot 6H_2O$ in an aqueous solution was used to give a 20 wt% on the activated carbon support.

3.1.3 Cathode sheets and coin cells

Cathode sheets are prepared by mixing a NMC cathode powder with a solution of polyvinyl difluoride dissolved in n-methyl pyrrolidone and carbon black. Polyvinyl difluoride acts as a binder to maintain the adhesion of the cathode components, and carbon black acts as an electronic conductor that imparts electrical connectivity between NMC particles and the current collector. The slurry solution is mixed in a planetary mixer and then spread onto an aluminum sheet current collector. The sheet is dried overnight under vacuum to drive off the solvent and then punched into discs of appropriate size for coin cells. The discs are then pressed at 3 tons/cm^2 to further enhance connectivity between particles and baked at elevated temperature in glove box to remove any residual water from handling in air.

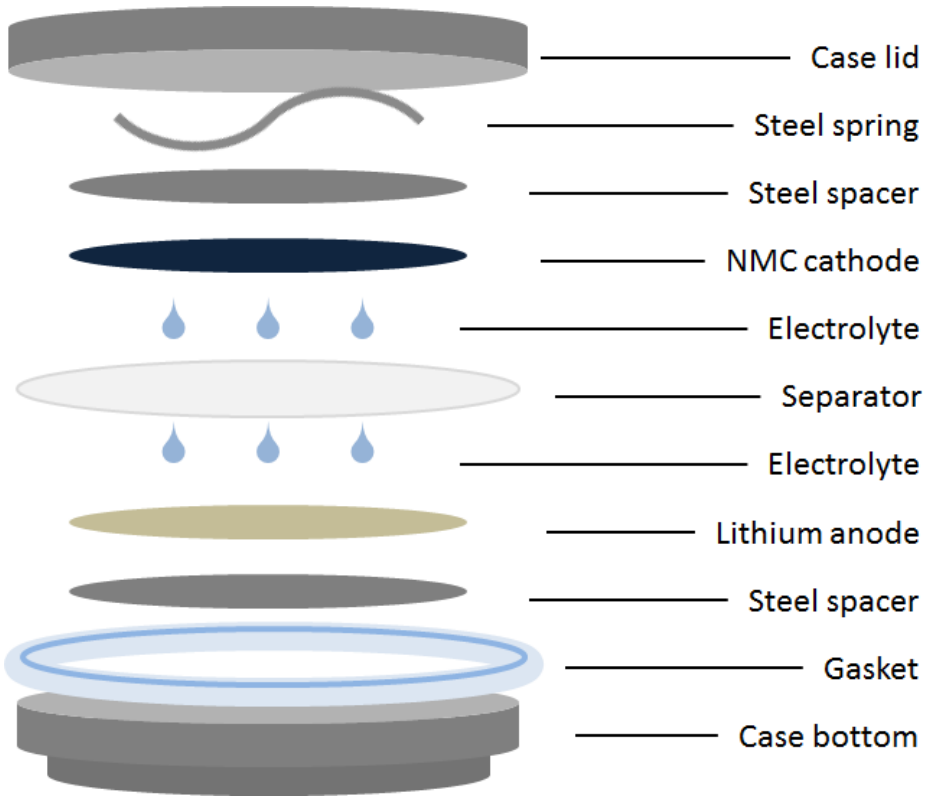

Figure 3.1. Exploded schematic of a typical half-cell with each component labeled. Cells are assembled bottom to top. The lithium anode is pressed against the steel spacer below it before being placed into the cell. The three droplets of electrolyte consist of 20 μL.

Figure 3.1 shows an exploded diagram of a coin cell. A proper assembly procedure is essential to optimizing coin cell operation. Coin cells were assembled in an Ar filled glove box using CR2032 type cases with Li foil or graphite used as the anode. Cells with Li foil were used for all studies except the elevated temperature storage test, which used cells with graphite anodes. The lithium foil is brushed with a nylon toothbrush immediately prior to assembly to remove any oxide formed at the surface. The electrolyte used was $LiPF_6$ in a 1-to-1 volume mixture of ethylene carbonate and dimethyl carbonate. The separators used are made of porous polypropylene and soaked for at least 5 minutes in electrolyte before assembly.

The assembly shown in Figure 3.1 shows the configuration with Li foil as an anode and is often referred to as a "half-cell." Commercial rechargeable batteries are "full-cells"

using graphite instead of a lithium anode, due to safety risk associated with lithium anodes. The half-cell is useful for non-rechargeable commercial batteries and for experimental studies on electrodes, such as NMC or $LiCoO_2$ cathodes, and can be operated safely in controlled laboratory conditions. Graphite anodes may be fabricated in a similar matter to cathodes, the powder is cast as a slurry and dried. Additionally, several vendors sell graphite anodes (and several types of cathodes as well) deposited on copper current collector sheets.

3.1.4 Atomic layer deposition

ALD in these studies was performed in two separate home-built reactors. The first two studies, covering electrocatalysis and catalysis, were performed in a fluidized bed reactor. The third study was performed in a viscous flow reactor with a static powder bed. Schematics of both these reactors may be found in the appendices at the end.

The viscous flow reactor consisted of a quartz flowtube 75 cm long and with 3.5 cm inner diameter and is heated using a three zone clamshell style furnace. Powders were placed on a static tray and spread as thin as possible (<1mm) over the tray surface to ensure rapid gas transport to particles at the bottom of the bed. The deposition chamber of the fluidized bed consists of a vertical stainless steel tube 45-cm tall, 5 cm in diameter at the bottom, and flared out at the middle and top to 9 cm. The chamber is lined with a removable insert that has a porous (10 μm) stainless steel distribution plate at the bottom to support the powder bed.

Fluidization is a condition in which a powder bed is agitated by a carrier gas stream passing vertically through the bed from the bottom to the top. The upward force acting on the particles must be similar in magnitude to the downward gravitational force acting on them to attain fluid-like behavior. Fluidized particles move vigorously in random directions, and may even “boil” under certain conditions. Minimum fluidization velocity of a carrier gas stream can be calculated using the following equation, derived from the Ergun equation:

1) $$v_f = \frac{(\rho_p - \rho) g D_p^2 \varepsilon^3}{150\eta(1-\varepsilon)}$$

where v_f = the minimum fluidization velocity, ρ = the density of the gas and ρ_p = the density of the particles, g = the gravitational force, D_p = the average particle diameter, ε = void fraction of the bed, and η = the viscosity of the gas.

In an ALD reactor, the carrier gas also acts to transport precursor vapors through convection. The precursors are held in bubblers and delivered to the reactor relying on their own intrinsic vapor pressures, or by passing an inert carrier gas through a heated bubbler to entrain the precursor vapor. Pressure during depositions is generally ~0.5 Torr in the viscous flow reactor and ~2 Torr in the fluidized bed reactor, as measured by pressure gauges on the reactor outlets. Reactor pressure is controlled through adjustment of the carrier gas flowrate using mass flow controllers, and through a throttle valve on the exhaust directly upstream of a roughing pump.

Depositions are performed at constant temperature after allowing the reactor temperature to equilibrate. Pulse sequences use precursor exposures of sufficient magnitude for the self-limited surface reactions to reach completion. Purge times between precursor pulses are long enough to allow all excess precursor and reaction byproduct to be removed from the reactor. These pulse and purge times were determined using in situ mass spectrometry, detailed in the following section.

Pulse sequences may be complex, ranging from a simple [A-B] sequence, where A and B represent complementary precursors such as trimethylaluminum (TMA) and H_2O, or $TiCl_4$ and NH_3. Square brackets in the sequence shown above denote individual cycles that may be repeated any number of times to achieve a desired film thickness. The number of cycles will correspond with a thickness according to the growth per cycle of the process. A more complex sequence may involve higher order patterns, for example ([A-B]x5 – [C-

D]x1)x100, where a ternary or higher order mixed oxide can be deposited with excellent compositional precision. The digital nature of pulsing resulting from the self-limiting reactions allows for a high degree of precision of materials synthesis. Due to the complexity of pulse sequencing, an ALD reactor is controlled by a computer utilizing a user defined recipe.

3.1.5 In situ mass spectrometry

In situ monitoring of reaction processes may be performed using a residual gas analyzer (RGA) that utilizes a quadrupole mass spectrometer. Real time chemical analysis of the reactor effluent allows surface reactions associated with film growth to be monitored, so that pulse and purge lengths may be determined in an expedient manner. An example spectra is shown in Figure 3.2.

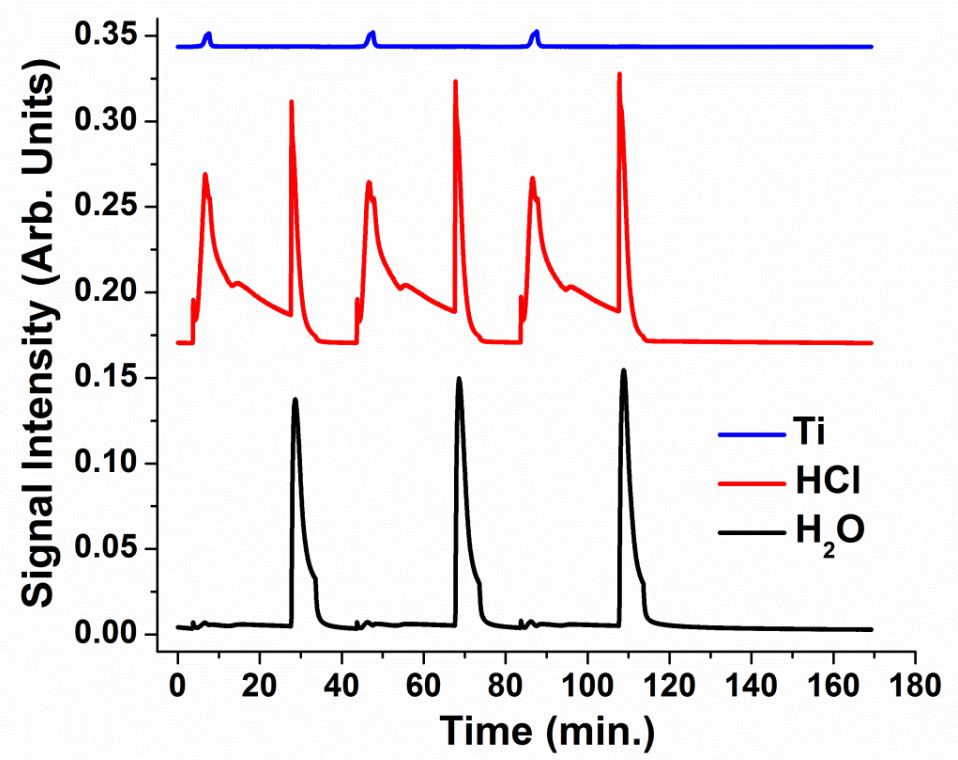

Figure 3.7. ALD pulse and purge times determined using a mass spectrometer. Signals of individual chemicals may be observed largely independent of one another. The spectra show the $TiCl_4$ – H_2O process which involves generation of HCl during half-reactions.

The quadrupole mass spectrometer analyzes effluent molecule masses by ionizing them on an electrically biased filament. The ions are filtered based on their mass to charge ratio using a field created by the four parallel rods of the quadrupole oscillating at radio frequency.[1]

3.1.6 Post-deposition heat treatment

Post-deposition heat treatments induce structural and chemical changes in an ALD coating and in the underlying substrate. These changes include crystallization, surface diffusion, diffusion into the bulk, reduction, oxidation, chemical decomposition and other chemical changes. Heat treatment temperatures are typically higher than the useable ALD temperatures (>400 °C), and involve process gasses such as nitrogen, oxygen and hydrogen. Heating under oxygen is often called calcination, while heating under hydrogen is often called reduction. The term annealing may also be used to describe heating process under a controlled environment. The heating rate may be ramped, and soak time at the target temperature is selected to optimize completion of the desired changes induced in the samples.

3.2 Materials characterization techniques

3.2.1 Scanning electron microscopy

Scanning electron microscopy (SEM) is a technique that allows for morphological imaging of a sample at the micron-to-nanometer scale.[1] The technique employs an electron beam that rasters over the area of interest. Atoms absorb the incident electron beam and emit low energy electrons that are inelastically scattered from the outer electron orbitals. Due to their low energy all detected secondary electrons originate within the outer few nanometers of any bulk sample, and give information regarding the morphology of the sample. The result electron micrograph appears similar to a photograph.

3.2.2 Energy dispersive X-ray analysis

Aside from secondary electrons, a variety of other signals emitted from the sample may be collected in an SEM. Also present are high energy X-rays that contain elemental information about the samples. The incident electron beam causes ejection of inner orbital electrons, creating holes in the orbitals. Holes are filled by electrons relaxing from higher orbitals, and an X-ray is emitted carrying the energy corresponding to the difference between the two electron orbitals.

Analysis of X-rays emitted by in this manner is called energy dispersive X-ray analysis (EDS).[1] EDS has a sampling volume much deeper than SEM, as high energy X-rays have an escape depth on the micron scale. This escape depth depends on X-ray energy and sample composition. As a result, EDS allows for characterization of the bulk properties of a sample. This makes the technique useful in analyzing the composition of ALD films deposited within highly porous samples.

3.2.3 Powder X-ray diffraction

Powder X-ray diffraction (PXRD) is a variant of X-ray diffraction (XRD) and is used to identify the lattice parameters and crystal phases present in a material. Scattering of X-rays from a single crystal results in points on the Ewald sphere, occurring due to constructive interference that results when the conditions of the Bragg equation ($n\lambda = 2d\sin\theta$) are satisfied.[2] A crystalline powder contains a collection of crystals randomly oriented in nearly every possible direction. This orientational randomization results in X-ray scattering in the form of concentric rings centering on the incident beam axis, instead of points. The individual points positioned on the Ewald sphere are collapsed into one dimension with the only significant factor being radial distance. The positions of these rings may be used to calculate the lattice parameters of various crystallographic orientations within the sample.

In addition to phase information, XRD may be used to estimate crystallite size using the Scherrer equation,[2] where the broadening of a peak is inversely proportional to the average crystallite size. This may be used to observe nucleation and growth of crystals in a disordered material. The Scherrer equation should be used with the caveat that other factors may contribute to peak broadening such as dislocations and grain boundaries.

3.2.4 Transmission electron microscopy

Transmission electron microscopy (TEM) is an electron microscopic technique distinct from SEM that relies on primary electrons transmitted through a sample rather than secondary electrons emitted from the sample. As electrons must pass entirely through the materials being studied, the sample must be no more than ~100 nm thick, and may require involved preparation such as using a microtome. The high resolution of TEM allows imaging of the crystal lattices within a sample.

3.2.5 Barrett-Joyner-Halenda (BJH) analysis

BJH analysis is a porous media characterization technique that allows for measurement of specific surface area, total pore volume, distribution of pore sizes, average internal pore diameter, and external pore diameter.[3] The internal pores of particles account for the very high surface area which is desirable in applications such as catalysis.

The Langmuir adsorption model describes surface coverage of a molecule based on the heat of adsorption and can be used to predict the behavior of simple systems characterized by surface coverage which is limited to a single monolayer. Brunauer-Emmett-Teller (BET) theory is an extension of the Langmuir model that accounts for the heat of adsorption of second and higher layers of physisorbed molecules and may account for the total volume of gas adsorbed in addition to the surface area.[4] The BET model is limited to measuring the volume of adsorbed gas multilayers on non-porous media (i.e. perfect spheres). BJH theory builds upon BET, using a combined model that incorporates the thermodynamics of

multilayer formation and the capillary action within pores. This more comprehensive model allows for accurate measurement of porous samples, and can measure non-Gaussian or Maxwellian pore size distributions with accuracy.

The BJH technique usually employs N_2 physisorption; measurements are performed at liquid nitrogen temperature to drive the condensation of the gas onto the particle surface and into the internal pores. The method analyzes the adsorption and desorption of N_2 with the amount of N_2 present in the sample vessel referenced to a control vessel. The BJH technique models hysteresis in the adsorption and desorption profiles as due to the capillary effect in the internal pore volume.

3.2.6 X-ray photoelectron spectroscopy

X-ray photoelectron spectroscopy (XPS) utilizes the photoelectric effect, which is the ejection of electrons from atomic orbitals upon absorption of electromagnetic radiation. This effect was connected to Einstein's discovery of the photon, the quantized unit of electromagnetic radiation. The XPS equation is written:

2) $$E_k = h\nu - E_b$$

The ejected electron from an atomic orbital within a specific bonding environment possesses a kinetic energy (E_k) equal to the incident photon ($h\nu$) minus the binding energy of the electron in its orbital (E_b).[5] XPS is a powerful tool for materials characterization due to its ability to measure photoelectron intensity and peak energy. The photoelectron energy may be used to identify the elements present in a sample and their local chemical environment. The reative intensity of the photoelectron emission is related to the stoichiometry within the probed volume.

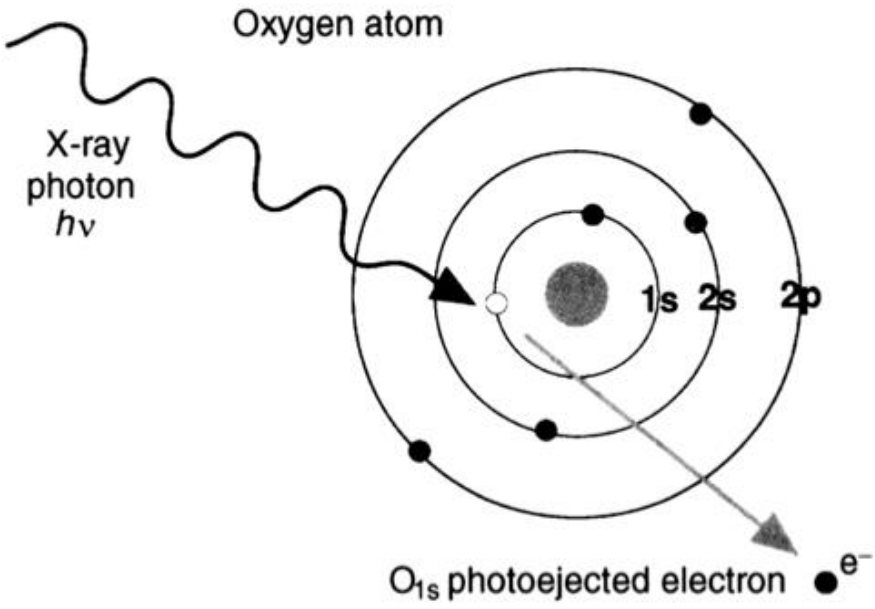

Figure 3.8. Diagram of the electron photoejection process. An X-ray with energy = hν collides with an orbital electron, resulting in ejection of a photoelectron with the energy of the incident X-ray minus the binding energy of the orbital electron.

XPS analysis is limited to the upper <10 nm of a sample surface due to the low mean free path of electrons (and photoelectrons) in solids. As a result, XPS is a surface sensitive characterization technique. This sampling volume limitation makes XPS optimally suited for analysis of nanometer thin films deposited by ALD. Bulk techniques such as EDS may not yield any useful information on a nanometer thin film where the coating to bulk atomic ratio is very low. Due to the extremely shallow sampling depth, analysis must be performed at ultra-high vacuum, so that physisorption of atmospheric molecules is minimized. Operation of the X-ray gun also requires ultra-high vacuum.

In addition to photoelectrons, Auger electrons are also observed in XPS spectra. Auger electrons are emitted as the result of a three electron orbital interaction. The photoejected electron leaves a hole, which is filled by an electron in a higher orbital that falls down to fill the hole. This relaxation is accompanied by X-ray generation. In some cases, the

energy associated with the emitted X-ray is transferred to a third electron orbital, ejecting an Auger electron with a kinetic energy dependent on this three orbital interaction.

The electronic structure of an atom gives rise to a unique set of photoelectron energies and intensities. When using this information for quantification of elements present in a sample, a sensitivity factor must be taken into account, which is based on the calculated and empirical photoejection probability of each electron orbital.[6]

Splitting of the electron peak energy in an XPS spectrum occurs for all electrons except those emitted from s-orbitals due to spin coupling of electrons with different angular momentum. Split peaks have near-degenerate energies, with peak-to-peak distance equal to the spin-orbit interaction energy. This peak splitting energy may vary as a function of chemical environment. Peaks exhibiting spin orbit splitting also have a total area that varies with the spin state. The $p_{1/2}$ and $p_{3/2}$ typically have an area ratio of 1:2, while $d_{3/2}$ and $d_{5/2}$ have a ratio of 2:3 and $f_{5/2}$ and $f_{7/2}$ have a ratio of 3:4.

Photoelectrons undergo inelastic scattering as they escape the solid sample and loose kinetic energy with each collision. The mean free path of an electron in a particular material determines both the amount of energy loss it undergoes, and the total sampling depth of the experiment. Due to this effect, nearly all XPS peaks have a broad tail, and exhibit step-like asymmetry with intensity of electrons increasing toward lower kinetic energy (Figure 3.4). Analysis of peaks must take into account this background noise. Peaks usually use a Shirley background subtraction, which is a function of the derivative of the peak and two end points at either side of the peak.[5, 6] The Shirley background curve takes on the shape of a rounded step.

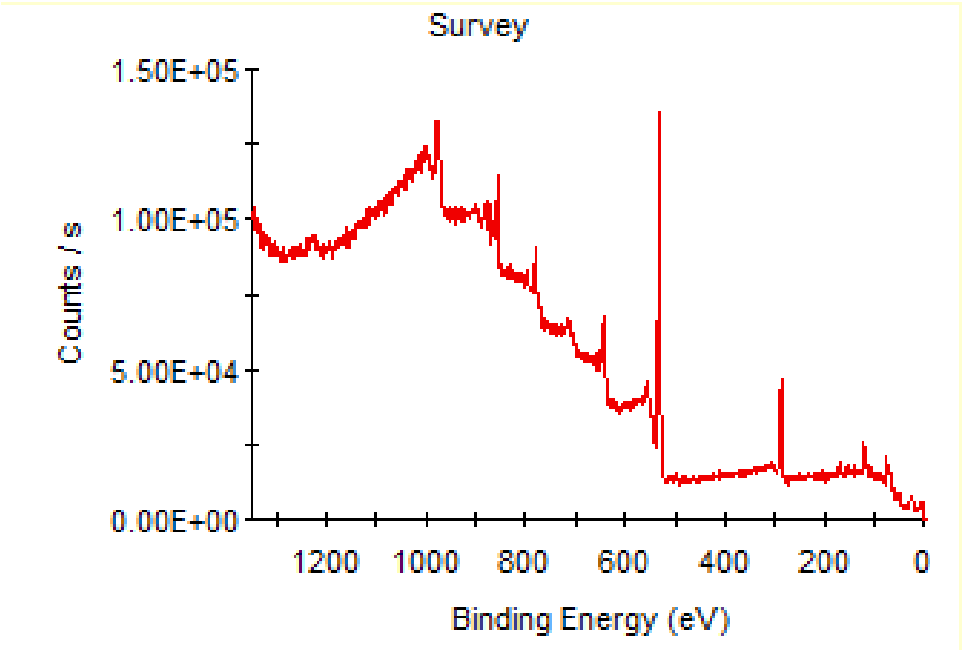

Figure 3.9. Example XPS survey scan showing the full emission spectrum of Al_2O_3 coated NMC particles. Step-like increase of the spectra towards the left is due to photoelectron loss energy by inelastic scattering, or bremsstrahlung.

Chemical shifts in XPS occur when the binding energy of an orbital deviates from that of the pure element due to the bonding environment. For example, the 2p peaks of TiO_2 have a higher binding energy than elemental titanium. The electron withdrawing nature of oxygen causes electrons in the titanium atom to move to a higher orbital binding energy and require more energy for photoemission. This chemical shift of the peak energy in XPS can be used to extract information on the chemical environment of the atoms, including situations when there are a variety of compounds containing the same element.[6]

Deconvolution of peaks may be necessary if multiple compounds are present, as peaks often overlap to a significant degree. Peaks of individual compounds and elements may be separated from a single, complex peak structure, by approximating each individual peak with a specific peak shape based on the statistical distribution of photoemitted electrons. Common peak functions are the Gaussian, Lorentzian and Voight functions. Use of the Shirley background here is an essential background correction allowing for the spectrum to

be properly modeled. Peak deconvolution may be used to quantify the relative amounts of different compounds containing the same element within the sampling volume. For example, relative concentrations of TiO_2 and Ti metal in the sample surface may be determined.

Ar^+ ion etching may be performed in conjunction with XPS to perform a depth profile. Etching was performed using a cluster source, which produces aggregates of Ar atoms with a single positive charge, rather than individual singly charged ions. Under the appropriate conditions, etching removes surface atoms in a controlled manner, so that alternating etch-scan steps will produce a compositional depth profile determining the elemental and chemical nature of the sample as a function of depth. Etching is a destructive technique and in some cases may cause damage to a sample, decreasing the oxidation state of certain elements, or catalyzing chemical reactions within the sample.

3.2.7 Inductively coupled plasma-atomic emission spectroscopy

Inductively coupled plasma-atomic emission spectroscopy (ICP-AES) is an elemental analysis technique that uses the emission spectra of atoms given off when excited in a plasma flame.[1] Samples are digested into an acidic solution and fed into the plasma flame using a peristaltic pump. The high energy plasma causes excitation of ground state electrons to higher atomic orbitals. Relaxation of an excited electron results in the emission of a photon with energy corresponding to the difference between the ground state and excited state orbitals. Intensity and position of peaks are interpreted using the well-known atomic emission energies to give molar concentration of the digestion solution.

This technique is destructive, requiring the digestion of a sample in acid. Care must be taken that the digested elements are not volatile. For example, digestions performed using hydrofluoric acid will lead to formation of volatile halide species such as PF_5 and SiF_4, which evaporate to give artificially low quantities of those elements.

3.2.8 Electrochemical impedance spectroscopy

Electrochemical impedance spectroscopy (EIS) is useful in the analysis of electronic properties of an electrochemical system by modeling it with equivalent circuit elements.[7] A sinusoidal AC signal is swept through a range of frequencies. Analysis of the phase offset between the signal across the electrochemical cell and a control yields the real and imaginary impedance of the cell. Information gained from EIS includes charge transfer resistance, double layer capacitance, and Ohmic resistance. To interpret the data, the spectra must be fit to an equivalent circuit diagram and are plotted as either a Bode plot, showing phase versus frequency, or as a Nyquist plot, showing imaginary versus real impedance.

Individual layers within an electrochemical cell may be differentiated by identifying their impedance. In a battery, this tool is useful in quantifying the charge transfer resistance, which correlates to the ease at which a Li^+ ion will intercalate into an electrode. It also allows a measurement of the solid electrolyte interphase (SEI) that evolves during cycling as a result of electrolyte decomposition. The impedance associated with the SEI can be modeled to monitor the extent of parasitic decomposition reactions.

3.2.9 Mass spectrometer-temperature programmed desorption

Specific density of surface acid and base sites of a powder can be measured using mass spectrometer-temperature programmed desorption (MS-TPD).[8] The mass spectrometer is also a quadrupole, identical to that used for in situ monitoring of ALD processes. This measurement is performed by exploiting the chemisorption of small molecule acids (CO_2) and bases (NH_3) onto basic and acidic surface sites, respectively. For example, CO_2 will react with MgO sites to form $MgCO_3$. Upon chemisorption of the desired probe molecule, the sample is heated in a linear temperature ramp, which will cause the $MgCO_3$ to decompose into its component parts once sufficient temperature has been reached to dissociate the two components. Upon dissociation, the CO_2 or NH_3 will desorb and is detected by the mass

spectrometer. Bond strength is thus related to desorption temperature, and observation of the evolved gasses allows for quantification of the surface sites, assuming a 1-to-1 ratio of detected probe molecules to surface sites.

3.2.10 Outside angle fluorescence

Fluorescence measurement is typically performed as a characterization technique to measure the light absorption and emission of fluorescent molecules dissolved in a solution.[1] A sample cuvette is filled with a solution of known concentration, and the sample is excited with light in the visible or UV range. Upon absorption of a photon, electrons in the fluorophore are excited to higher energy orbitals and excited vibrational modes are activated in the molecule. Relaxation of the molecule occurs first by vibrational relaxation, and then by relaxation to a lower electronic orbital, which is accompanied by emission of a photon corresponding to the energy of the orbital relaxation.

The fluorophore used in this study was 1-pyrene butyric acid, which was grafted to the surface of the ALD coated particle.[9] Pyrene has the unusual property that it forms an excimer consisting of two stacked pyrene molecules, which fluoresces at a higher wavelength than the monomer.[10] When bound to a surface containing clustered and isolated base sites, excimer formation at clustered sites and monomers will form at isolated sides, leading to fluorescence at both wavelengths. This enables identification and qualitative measurement of the amount of base sites proximity.

To measure fluorescence of a solid sample, a cuvette solution cannot be used. Instead, outside angle fluorescence measurements must be performed.[9] Due to this complication, samples were pressed into pellets positioned at an angle so that photons generated by fluorescence reach the detector, while the incident photons do not reflect off the sample into the detector.

3.2.11 High temperature storage measurements

High temperature coin cell storage experiments using full cells employing graphite anodes allow analysis and tracking of a coin cells' lithium inventory.[11] Cells are cycled and then held at 4.3V in an incubator at 40 °C for 500 hours. After the storage period, the cells are cycled again. The voltage drop during the storage period gives some indication of the reactions leading to self-discharge within the cell. The first (D_1) and second (D_2) cycles after storage are compared with the cycle immediately prior (D_0) to the storage test. The difference between D_1 and D_2 shows the reversible capacity loss. The difference between D_2 and D_0 show the irreversible capacity loss. Generally speaking, reversible capacity loss is due to charge shuttling reactions such as decomposition of a $LiPF_6$ electrolyte molecule to form a negative charge that can shuttle a Li^+ from anode to cathode. Irreversible capacity loss might involve decomposition of the electrode crystal structure which hosts Li^+, or loss of Li^+ to form an electrochemically inactive species such as LiF.

3.3 References

1. Strobel, H. A.; Heineman, W. R., *Chemical Instrumentation: A Systematic Approach*. Third Edition ed.; John Wiley & Sons, Inc.: 1988.

2. Cullity, B.; Stock, S., *Elements of X-Ray Diffraction*. 3rd ed.; Prentice-Hall Inc.: 2001.

3. Barrett, E. P.; Joyner, L. G.; Halenda, P. P., The Determination of Pore Volume and Area Distributions in Porous Substances. I. Computations from Nitrogen Isotherms. In Journal of the American Chemical Society, 1951; Vol. 73, pp 373–380

4. Brunauer, S.; Emmett, P. H.; Teller, E., Adsorption of Gases in Multimolecular Layers. In Journal of the American Chemical Society, 1938; Vol. 60, pp 309–319

5. Hüfner, S., *Photoelectron Spectroscopy*. 3rd Edition ed.; Springer: 2003.

6. Moulder, J. F.; Stickle, W. F.; Sobol, P. E.; Bomben, K. D., *Handbook of X-ray Photoelectron Spectroscopy*. Perkin-Elmer Corporation, Physical Electronics Division: Eden Prairie, Minn. 55344, 1992.

7. Bard, A. J.; Faulkner, L. R., *Electrochemical Methods: Fundamentals and Applications*. 2nd edition ed.; Wiley: 2000.

8. Karge, H. G.; Dondur, V., Investigation of the Distribution of Acidity in Zeolites by Temperature-Programmed Desorption of Probe Molecules .1. Dealuminated Mordenites. *Journal of Physical Chemistry* **1990,** 94, (2), 765-772.

9. Katz, A.; Davis, M. E., Molecular imprinting of bulk, microporous silica. *Nature* **2000,** 403, (6767), 286-289.

10. Winnik, F. M., Photophysics of Preassociated Pyrenes in Aqueous Polymer-Solutions and in Other Organized Media. *Chemical Reviews* **1993,** 93, (2), 587-614.

11. Sinha, N. N.; Smith, A. J.; Burns, J. C.; Jain, G.; Eberman, K. W.; Scott, E.; Gardner, J. P.; Dahn, J. R., The Use of Elevated Temperature Storage Experiments to Learn about Parasitic Reactions in Wound LiCoO2/Graphite Cells. *Journal of the Electrochemical Society* **2011,** 158, (11), A1194-A1201.

4 Tuning Acid-Base Properties Using Mg-Al Oxide Atomic Layer Deposition

Atomic layer deposition (ALD) was used to coat γ-Al_2O_3 particles with oxide films of varying Mg-to-Al atomic ratios, which resulted in systematic variation of the acid and base site area densities. Variation of the Mg-to-Al ratio also affected morphological features such as crystalline phase, pore size distribution, and base site proximity. Base site area density increased with increasing Mg content, while acid site density was at a maximum with similar number of Mg and Al atoms in the coating. This behavior leads to nonlinearity in the relationship between Mg-to-Al and acid-to-base site ratio. The physical and chemical properties were elucidated using scanning electron microscopy (SEM), energy-dispersive X-ray spectroscopy (EDS), powder X-ray diffraction (XRD), X-ray photoelectron spectroscopy (XPS), N_2 physisorption, and CO_2 and NH_3 temperature-programmed desorption (TPD). Fluorescence emission spectroscopy of samples grafted with 1-pyrenebutyric acid (PBA) was performed to analyze base site proximity. The degree of base site clustering was correlated to acid site density. Catalytic activity in the self-condensation of acetone was dependent on sample base site density and independent of acid site density.

4.1 Introduction

The use of atomic layer deposition (ALD) in catalysis has found multiple successful applications in recent years.[1-7] Excellent conformality in complex geometries and sub-nanometer-level thickness control[8, 9] make ALD well suited for coating high surface area catalysts. However, few examples exist where the high degree of compositional control offered by ALD has been utilized for catalysis.[7, 10, 11] We show here the surface acid/base properties of a catalyst can be controlled by modifying the pulse sequences in the ALD coating of Mg-Al oxide onto γ-Al_2O_3.

The use of ALD grown mixed oxide catalysts has been studied in the deposition of Ti-V-O, in which control over the pulsing sequence enabled optimization in the liquid phase epoxidation of cyclohexene.[12] ALD has also been shown to enable the tailoring of catalyst acidity,[13-16] although to the best of our knowledge, this is the first example of using ALD to tune both acidity and basicity.

Basic oxides have been studied for their use as catalysts and catalyst supports.[17-19] Traditionally, solid bases have been made by precipitation of the bulk oxide, ion exchange with alkali metal cations,[20, 21] impregnation or occlusion with basic salts or metals,[22-24] and nitridation.[25, 26] These solid oxides are of interest in catalysis because of their potential to replace corrosive homogeneous catalysts such as NaOH, facilitate catalyst separation, and reduce waste stream processing. Basic oxide catalysts have been used in numerous chemistries including isomerization of alkenes, addition reactions, Knoevenagel condensations, and aldol condensations.[20, 27, 28] They are also relevant in biomass conversion strategies, and have been used for the aldol condensation of furfurals with acetone and propanal to produce diesel fuel precursors.[29, 30] We have selected mixed Mg-Al oxide for study here due to its widespread use as a basic oxide.[17, 18]

Magnesium oxide (MgO) films have been deposited by ALD onto planar Si and soda lime glass using Cp_2Mg (bis(cyclopentadienyl)magnesium) and water.[31] Also, magnesium aluminate and mixed magnesium aluminum oxide films have been deposited by using the Cp_2Mg MgO ALD process in combination with Al_2O_3 ALD using trimethylaluminum (TMA).[10, 32] In addition to Cp_2Mg, $EtCp_2Mg$ (bis(ethylcyclopentadienyl)magnesium)[33] and $Mg(thd)_2$ (thd = 2,2,6,6-tetramethyl-3,5-heptanedione)[34] have been studied in the ALD of MgO. We have selected Cp_2Mg, TMA and H_2O as precursors here in the ALD of Mg-Al

oxide. We have selected γ-Al_2O_3 as a powder substrate, due to its broad usage and characterization in the field of catalysis.

4.2 Results and Discussion

The commercial γ-Al_2O_3 particles used as the substrate are fabricated through the calcination of boehmite. The structure of γ-Al_2O_3 made using this process is typically described as having a cubic lattice with a tetragonal distortion.[35, 36] The pores of γ-Al_2O_3 form from the breakdown of hydroxide layers of boehmite, and as a result contain water and hydroxide species, as well as exhibiting some amorphous regions near the surface.[35, 36] The γ-Al_2O_3 phase of Al_2O_3 form a highly mesoporous structure composed of interconnected rod-like nanoparticles.[37]

Particles were coated using 36 ALD cycles (~4 nm) with varying Mg-to-Al pulse ratios. Samples are named to reflect the Mg:Al pulse ratio used during ALD (ratios in this study were: 1:0, 2:1, 1:1, 1:2 and 0:1). Figure 1 shows SEM images of the substrate particles (Figure 1A) and the 1:0 coated particles after 600 °C calcination (Figure 1B). All particles were sieved to within ~11-30 μm in diameter, and is confirmed by SEM. All samples appeared similar in SEM, demonstrating the ability of ALD to deposit thin, conformal films.

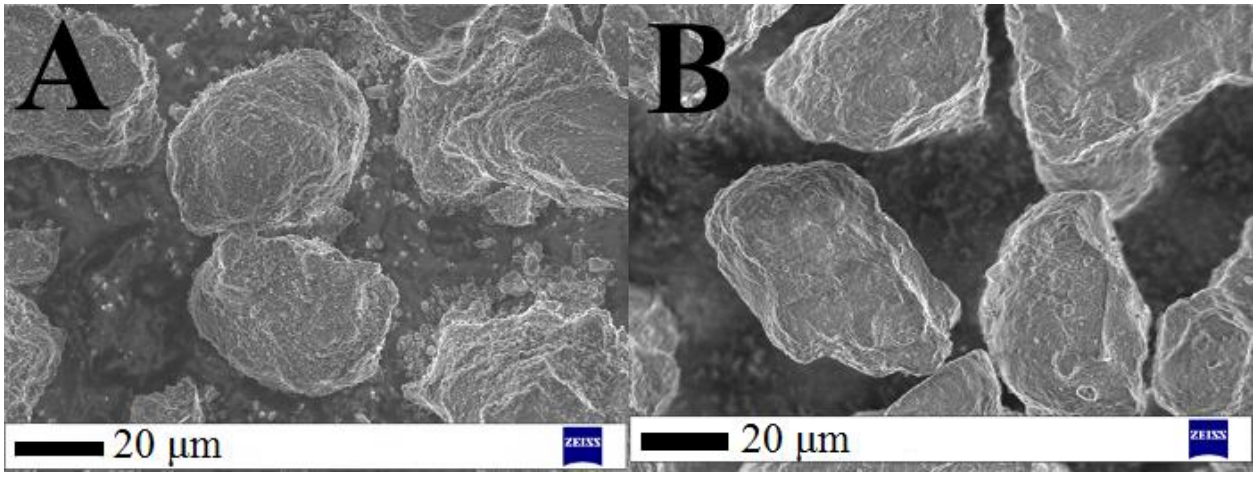

Figure 4.1. SEM micrograph showing (A) the γ-Al_2O_3 substrate and (B) the 1:0 sample after calcination. The scale bars show 20µm.

EDS was used to measure the bulk elemental composition of the samples (Figure 2A), and shows that Mg:Al pulse ratio has a monotonic relationship with Mg/Al atomic ratio. Both the γ-Al_2O_3 substrate and the ALD coating are measured due to the 10 – 20 µm sampling depth of EDS, such that this technique cannot be used to directly measure the Mg/Al content of the ALD film. XPS analysis was also used to quantify the elemental composition of the samples within the shallower sampling volume of the instrument, which is several nm. Similar trends in Mg/Al atomic ratio were observed; however the amounts of Al detected were much lower, with 1:0 having an atomic ratio of 7.32±0.75. Additional studies of these ALD films on other substrates would allow clearer insight into the chemical species present within a mixed Mg/Al film, however the composition of nm-scale ALD films are extremely surface dependent, and results would vary dependent on the substrate.

It should be noted that 1 g of powder in the 5 cm diameter column used in this study leads to a bed height of less than 1 mm, leading to difficulties in fluidization. Additionally, particles in the 10s of µm in size are classified as Geldart C particles,[38] which also are known to agglomerate and are difficult to fluidize. The homogeneity of coating of particles was

confirmed using EDS, and error bars shown represent sampling of 12-15 particles per experimental sample, and shows good homogeneity.

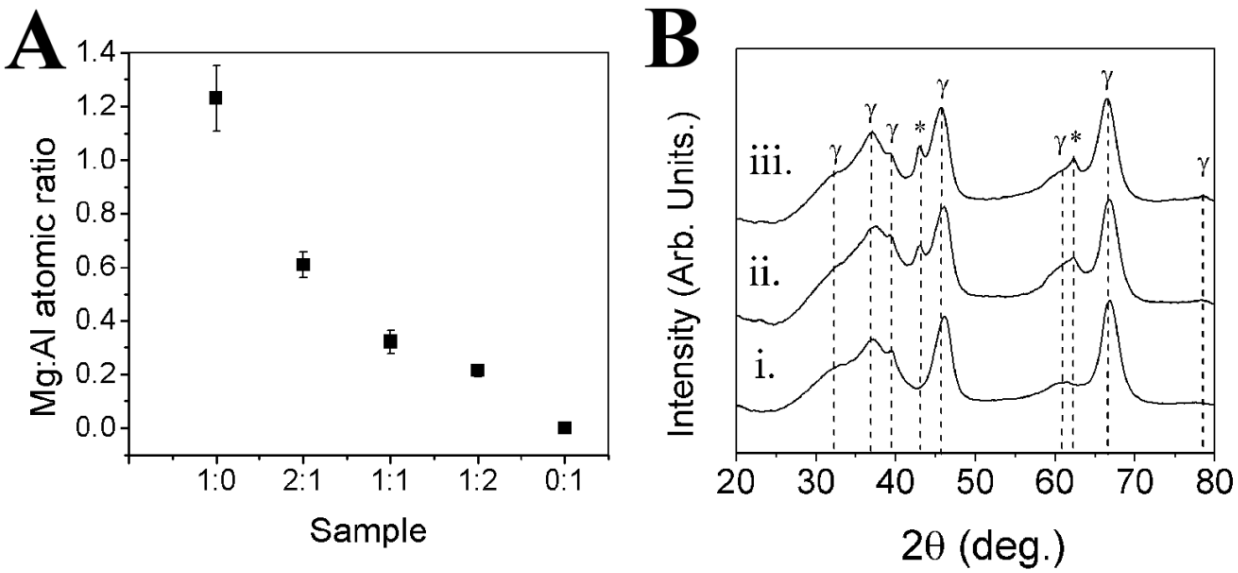

Figure 4.2. A. Mg:Al atomic ratio as determined by EDS point analysis. Samples are named X:Y to reflect the Mg to Al pulse ratio used during ALD. B. Powder XRD spectra showing (i) uncoated γ-Al_2O_3 (ii) 1:0 as deposited, and (iii) 1:0 after 600 °C calcination in air. Peaks marked with "γ" indicate γ-Al_2O_3 and "*" indicate cubic MgO.

We note that ALD of 36 cycles of either oxide or a mixture of oxides is estimated to completely fill all pores of the γ-Al_2O_3, because the predicted thickness of the oxides (~4 nm)[32] is thicker than the average radius of the pores (~3 nm, BJH). However, the magnesium content in the 1:0 sample was ~2 times lower than that estimated assuming that the entire pore volume was filled with crystalline MgO (Mg/Al atomic ratio = 2.2 for crystalline MgO). Possible reasons for this lower than expected measured value include: low film density, pore clogging, and surface poisoning[39, 40] by cyclopentadiene ligands. The relatively wider error bars of the 1:0 sample reflect less homogeneous deposition, and may reflect these factors. This varied deposition is in contrast to reports using this same precursor system on glass and Si wafers, in which pulsing ratio showed little effect on growth per cycle.[32] A seed layer

consisting of a single TMA – H_2O cycle did not significantly affect Mg/Al atomic ratio, indicating that nucleation of MgO on γ-Al_2O_3 is not a likely a cause of the apparent low Mg content.

XRD spectra were acquired for all samples before and after calcination at 600 °C in air for 2 hours. Nearly all spectra were identical to the substrate spectrum (Figure 2Bi), which shows peaks belonging to the γ-Al_2O_3 structure. Spectra with additional peaks were obtained for the 1:0 sample as deposited (Figure 2Bii) and the 1:0 sample calcined in air (Figure 2Biii), which were identified as peaks corresponding to the cubic MgO phase. Calcination causes a small degree of sharpening of the cubic MgO peaks. Using the Scherrer equation with a shape factor of 0.9,[41] MgO crystallites were estimated to be 2.8 nm in the 1:0 as deposited sample and 10.9 nm in the 1:0 calcined sample. A lack of any other peaks in the other samples indicates that the deposited films either remain amorphous, or that the Al_2O_3 crystallizes while MgO remains amorphous. Both of these results are supported by previous studies of calcined ALD films.[3] Phase segregation of spinel $MgAl_2O_4$ in bulk oxides has been reported in the literature when Mg/Al < 1,[42] however this phase was not observed in XRD of these samples. No other phases are expected in this system.[43] The absence of the spinel phase is consistent with other reports of MgO and Mg-Al oxide ALD onto planar Si and soda lime glass, as well as onto ZrO_2 and SiO_2 powders.[31-33]

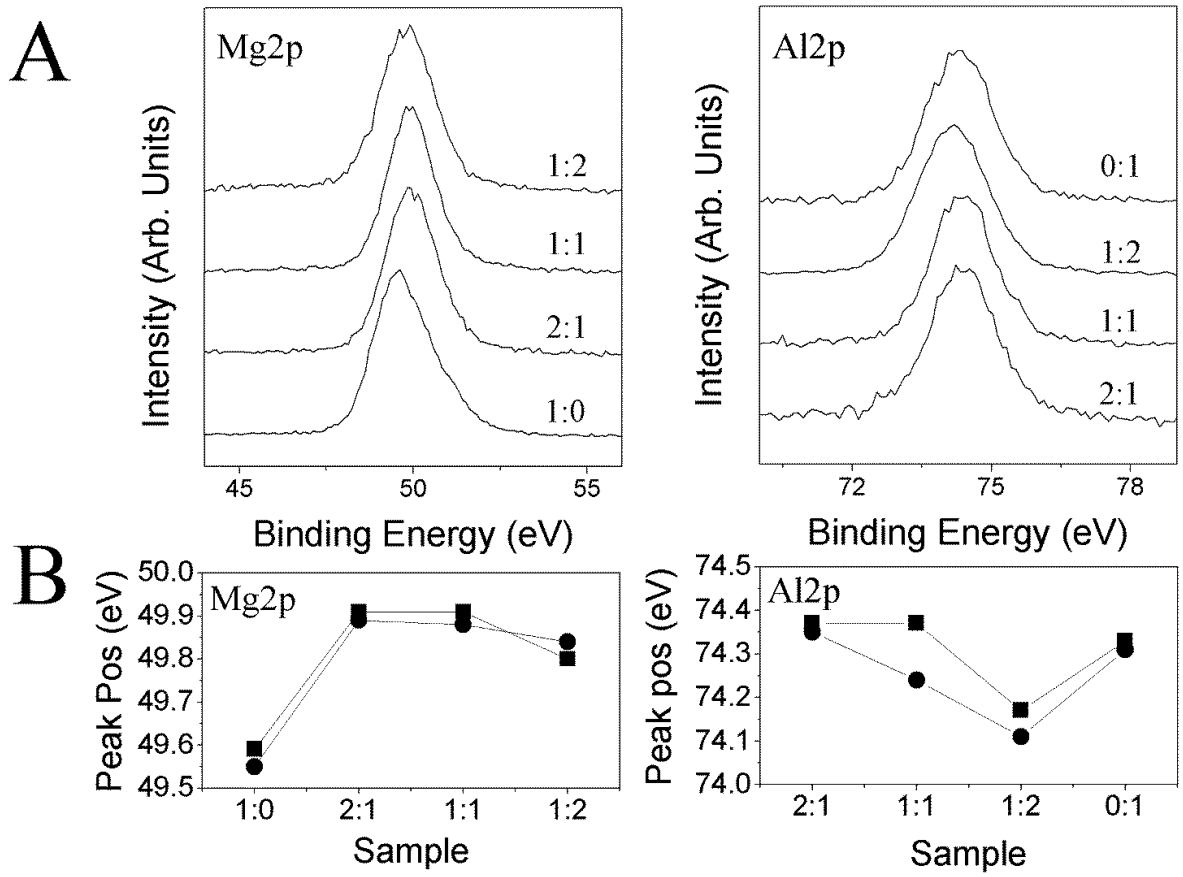

Figure 4.3. (A) XPS spectra of Mg2p and Al2p regions showing changes in peaks depending on precursor pulse ratio. (B) Plots showing peak position of as made (■) and calcined (●) samples.

The most significant difference observable by XPS analysis of the samples is that when deposited in the pure MgO form in 1:0, the Mg2p peak is ~49.6 eV, roughly 0.5 eV lower in binding energy than in the other samples. All mixed Mg-Al samples have roughly the same Mg2p peak position. This difference in binding energy is correlated with the difference in the XRD spectra of 1:0 versus the other samples. However, crystalline MgO is typically reported at >50 eV,[44, 45] so the binding energy is shifted in the opposite direction to that expected. Lower binding energy may be due to reduced ionicity of the Mg atoms. The Mg2p peak shows no change with calcination. Al2p peaks are all within the expected range,[46, 47] although reduction in Al2p binding energy is observed in two cases. The peaks

shift to lower binding energy when mixing Mg and Al in the coatings, in particular 1:1, and also upon calcination of 1:2. This reduction in binding energy may be due to the partial oxidation of Al^{3+} due to interactions with MgO.

N_2 physisorption was performed on all ALD-coated and calcined samples, and the uncalcined samples with Mg:Al ratios of 1:0, 1:1, and 0:1 were analyzed, as shown in Figure 4A. Calcination resulted in an increase in BET surface area in all samples measured. Higher Mg content was correlated with a smaller change in surface area upon calcination, likely due to a tendency of the MgO to be polycrystalline upon deposition (see Figure 2B). The 1:0 as deposited sample and the 1:0 calcined sample are both polycrystalline and have the lowest change in surface area upon calcination (because the sample was partially crystalline upon deposition). Also, a higher Mg content led to higher surface area before and after calcination. The 0:1 sample showed the greatest change in surface area upon calcination. Changing surface area is attributed to a densification of ALD films caused by loss of hydroxyls and by crystallization.[3] Given that ALD Al_2O_3 is amorphous and conformal on the substrate, its crystallization may be associated with increasing surface area from cracking of the ALD film and opening of clogged pores from densification. It should be noted that no significant change in γ-Al_2O_3 peak broadening was observed in XRD spectra.

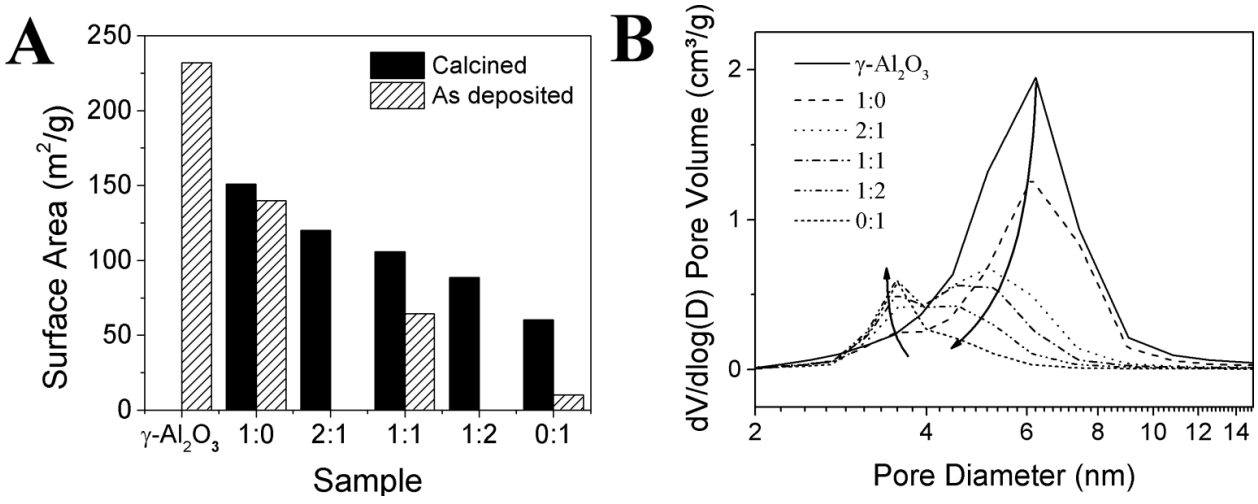

Figure 4.4. (A) BET surface area of samples as deposited (gray), and after 600 °C calcination in air (black). Numbers X:Y denote Mg:Al pulse ratio. (B) Pore volume distribution for the γ-Al_2O_3 substrate and all calcined samples showing a bimodal pore formation trend.

Trends in pore size distribution are shown in Figure 4B, which shows distributions for γ-Al_2O_3 and all calcined samples. Pores may be separated into two size-groups, the first group between 3 and 4 nm, and the second group between 4 and 10 nm. Populations of these two groups depended on the Mg/Al ratio. The pores of the γ-Al_2O_3 substrate show a peak maximum at 6.12 nm with no peaks in the smaller size-group. Interestingly, the average pore diameter of 1:0 was equal to that of the substrate. As Mg/Al decreases, the number of pores and the mean pore diameter in the larger size-group decreases. Additionally, as Mg/Al decreases, the population of the smaller size-group of pores increases. The peak maximum of the smaller size-group is fixed at 3.5 nm regardless of Mg/Al. These 3.5 nm pores are not present in the γ-Al_2O_3 substrate, and form with all ALD samples. The area of this peak increases with decreasing Mg/Al, and the peak is largest with the 0:1 sample. The 3.5 nm pore is attributed to the densification of amorphous alumina that has filled the 6.2 nm pores of the γ-Al_2O_3 substrate. Such a change corresponds to a loss of a third of the volume upon

densification, assuming that the initial state has a pore volume completely filled with amorphous alumina. Also, a pore diameter of 6.2 nm is incongruous with the 10.9 nm MgO crystallite diameter estimated from XRD. This result indicates a few possibilities: that crystallite formation dominates in pores larger than the average pore diameter, that crystallites are continuous in the direction of the pore length, or that a significant fraction of MgO crystallites are on the outside of the particles.

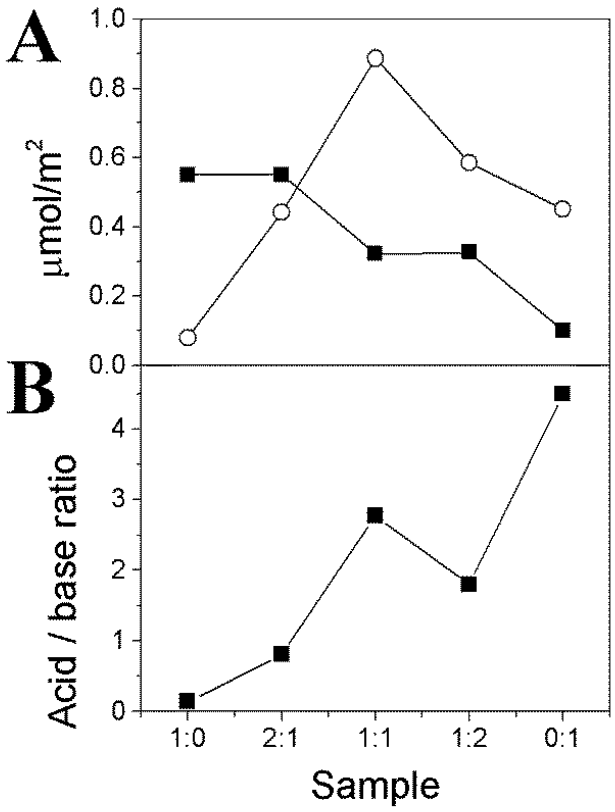

Figure 4.5. (A) Site area densities for base (■) and acid (○) sites in μmol/m2 for all ALD samples. (B) Acid to base site molar ratio.

TPD was performed using CO_2 to measure the number of base sites and NH_3 to measure the number of acid sites, the results are shown in Figure 5A. Standard deviation in these values was ±4%, a value smaller than the symbols used to represent points in this figure. The γ-Al_2O_3 substrate calcined at 600 °C in air gave an average acid site density of 53 μmol/g, and when calcined in He it gave a site

density of 146 μmol/g. This difference is attributed to cationic Al centers that act as Lewis acid sites which are oxidized when calcined in air, but remain stable in He. Samples in Figure 5 were calcined in air to be consistent with reaction pretreatment conditions. TPD spectra of CO_2 show a single peak corresponding to weak basic sites associated with $MgCO_3$ formation.[42]

This study showed that the number of base sites roughly decreased with decreasing Mg content. However, 1:0 and 2:1 were similar with 0.55 μmol/m^2 base site densities and 1:1 and 1:2 were similar with 0.32-0.33 μmol/m^2 base sites densities. The similarity in base site densities is surprising in that the atomic concentration of Mg in 1:0 was almost two times higher than 2:1, demonstrating that base site density is not dependent on elemental composition alone. Acid site densities were highest when Mg:Al was closest to 1:1.

To study base site clustering, the fluorophore PBA was grafted to base sites on the ALD oxide surfaces, and fluorescence emission was measured using 300 nm light excitation (Figure 6).[48-50] Peaks from 350 to 410 nm indicate monomers of pyrene, while the broad peak around 460 nm indicates dimer excimers which form when two or more pyrene molecules are at an intermolecular distance of $0.3 \leq z \leq 1.0$ nm.[51] Pyrene monomers form at isolated base sites while the dimers form at neighboring base sites.

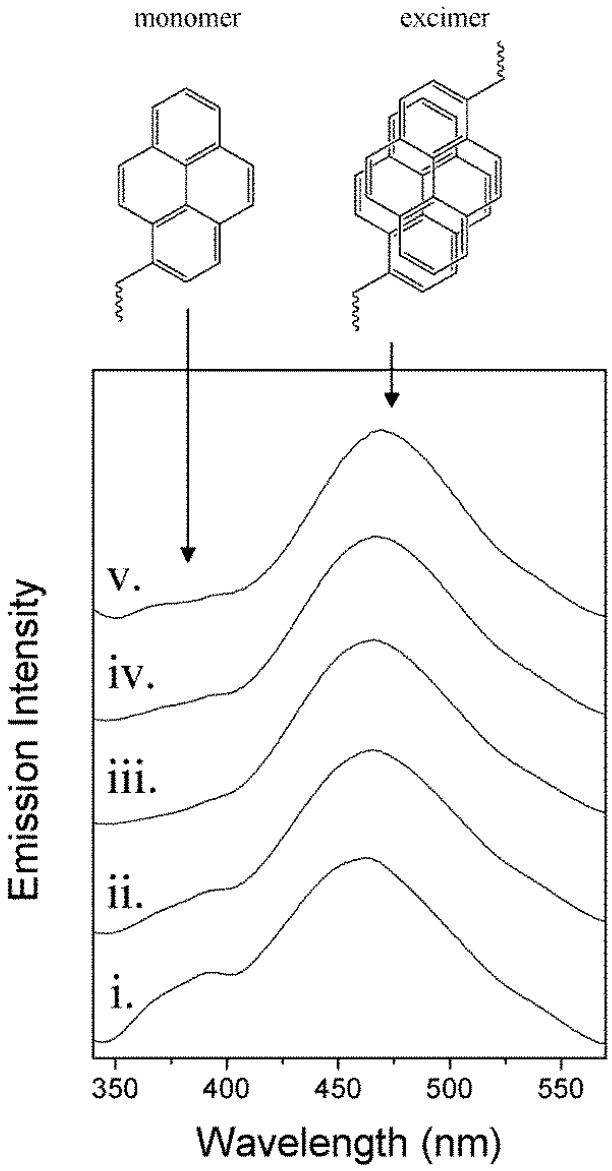

Figure 4.6. Fluorescence emission spectra of pyrenebutyric acid grafted to ALD samples i. 1:0, ii. 2:1, iii. 1:1, iv. 1:2, V. 0:1. Peak heights are normalized.

Red-shifting of the excimer peak indicates a higher degree of pyrene interaction.[51] It was observed that lower Mg/Al led to more pyrene interaction, as excimer peak positions increase monotonically going to higher aluminum content, with 1:0 occurring at 462 nm, 2:1 at 464 nm, 1:1 at 466 nm, 1:2 at 467 nm and 0:1 at 470 nm. (±1.25 nm). This shift is likely

due to the decreasing pore diameter with higher aluminum content rather than base site clustering, as it is not correlated to pyrene monomer peak area, nor increasing base site density. A higher curvature of the pore walls would lead to increased interactions between PBA bound to the oxide surface. The monomer peaks in the region between 350-400 nm are smallest in the 1:1 spectrum. Increasing or decreasing Mg:Al from 1:1 corresponds with increases in the monomer peak area. The intensity of the monomer peak is in an inverse relation to the acid site density of the surface. Such a relationship would indicate that high acid site density leads to a clustering of base sites, while low acid site density leads to more well-spaced base sites, causing monomer formation. This behavior suggests the possibility of a certain degree of spatial control over the active sites which should be explored further.

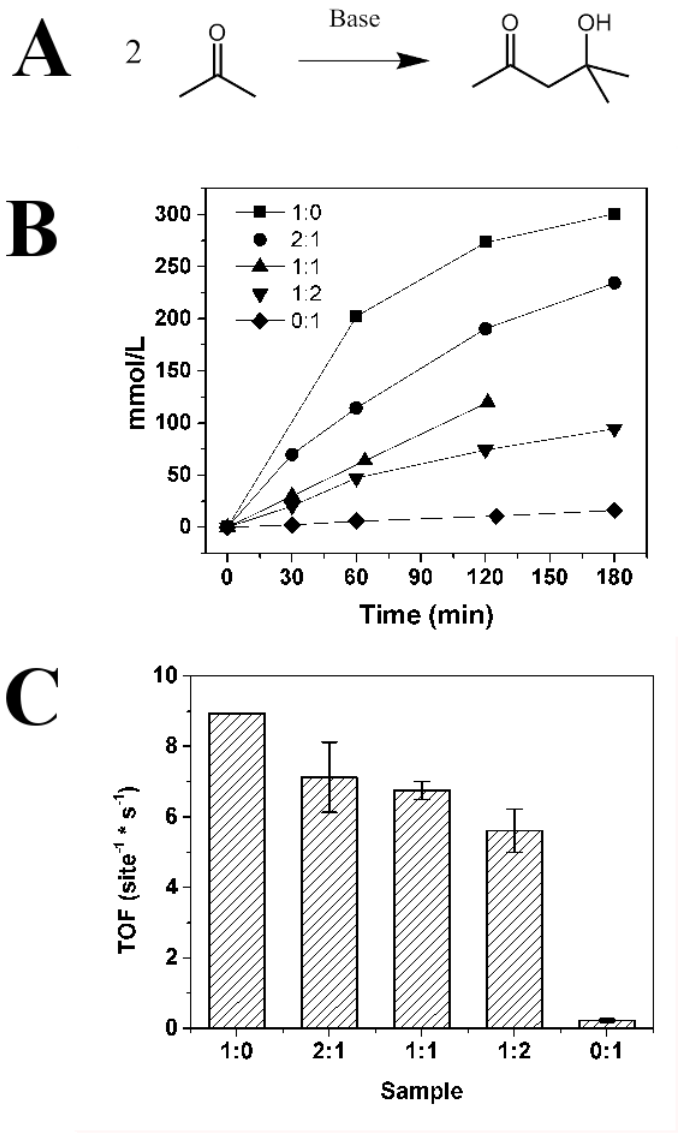

Figure 4.7. (A) The chemical pathway of the acetone self-condensation reaction. (B) Concentration of diacetone alcohol in mmol per liter of acetone as a function of time. (C) Turnover frequency in the production of diacetone alcohol.

Acetone self-condensation reactions were performed using powders calcined at 600 °C immediately prior to reaction. Reactions were performed in glass reactors at 60 °C in pure acetone. The rate of diacetone alcohol (DAA) production was highest for the 1:0 sample, and more DAA was produced with more Mg in the ALD coating (Figure 7B). Additionally, turnover frequency (TOF) of acetone to DAA (Figure 7C) showed that individually, all base

sites behave similarly in all mixed Mg-Al samples, which agrees with other reports on solid base catalyzed aldol condensation.[52] Overall there is a trend of slightly increasing activity with higher Mg content. As the number of base sites determines the DAA production, it can be concluded that the aldol condensation reaction here shows no dependence on measured acid site density or base site proximity, consistent with the base catalyzed aldol condensation mechanism which only requires a single base site and does not require cooperativity between multiple base sites. Areas of future work include reactions that require two reaction intermediates on separate base sites to probe base site cooperativity, or reactions that require neighboring acid and base sites, such as the dehydrogenation of ethanol to acetaldehyde.[42]

4.3 Conclusion

γ-Al_2O_3 was coated using ALD Mg-Al mixed oxides with varied pulse sequences resulting in control of the Mg and Al concentrations in the coatings. Cubic MgO phase was present only in the sample coated using exclusively Cp_2Mg and H_2O as precursors. Upon calcination, MgO crystallites were about 10.9 nm, which is larger than the mean pore diameter (6.2 nm). This size is likely due to crystallite formation in larger than the average pores, or crystallites continuous in the direction of the pore length. Base site density was generally higher for higher Mg content, while acid site density was highest when the coatings were performed in a 1:1 Mg to Al pulse ratio. This high acid site density in the 1:1 sample was correlated with higher base site clustering and lower Al2p XPS binding energy. All samples had similar acetone self-condensation reaction rates when normalized by the number of base sites, demonstrating that the reaction is independent of base site clustering or base to acid site ratio. This study provides a platform for future studies on reactions requiring fine control over acid and base site.

4.4 References

1. Feng, H.; Lu, J.; Stair, P. C.; Elam, J. W., Alumina Over-coating on Pd Nanoparticle Catalysts by Atomic Layer Deposition: Enhanced Stability and Reactivity. *Catalysis Letters* **2011,** 141, (4), 512-517.

2. Lu, J.; Fu, B.; Kung, M. C.; Xiao, G.; Elam, J. W.; Kung, H. H.; Stair, P. C., Coking- and Sintering-Resistant Palladium Catalysts Achieved Through Atomic Layer Deposition. *Science* **2012,** 335, (6073), 1205-1208.

3. O'Neill, B. J.; Jackson, D. H. K.; Crisci, A. J.; Farberow, C. A.; Shi, F. Y.; Alba-Rubio, A. C.; Lu, J. L.; Dietrich, P. J.; Gu, X. K.; Marshall, C. L.; Stair, P. C.; Elam, J. W.; Miller, J. T.; Ribeiro, F. H.; Voyles, P. M.; Greeley, J.; Mavrikakis, M.; Scott, S. L.; Kuech, T. F.; Dumesic, J. A., Stabilization of Copper Catalysts for Liquid-Phase Reactions by Atomic Layer Deposition. *Angewandte Chemie-International Edition* **2013,** 52, (51), 13808-13812.

4. Lu, J. L.; Low, K. B.; Lei, Y.; Libera, J. A.; Nicholls, A.; Stair, P. C.; Elam, J. W., Toward atomically-precise synthesis of supported bimetallic nanoparticles using atomic layer deposition. *Nature Communications* **2014,** 5.

5. Canlas, C. P.; Lu, J. L.; Ray, N. A.; Grosso-Giordano, N. A.; Lee, S.; Elam, J. W.; Winans, R. E.; Van Duyne, R. P.; Stair, P. C.; Notestein, J. M., Shape-selective sieving layers on an oxide catalyst surface. *Nature Chemistry* **2012,** 4, (12), 1030-1036.

6. Lee, J. C.; Jackson, D. H. K.; Li, T.; Winans, R. E.; Dumesic, J. A.; Kuech, T. F.; Huber, G. W., Enhanced stability of cobalt catalysts by atomic layer deposition for aqueous-phase reactions. *Energy & Environmental Science* **2014,** 7, (5), 1657-1660.

7. O'Neill, B. J.; Jackson, D. H. K.; Lee, J.; Canlas, C.; Stair, P. C.; Marshall, C. L.; Elam, J. W.; Kuech, T. F.; Dumesic, J. A.; Huber, G. W., Catalyst Design with Atomic Layer Deposition. *ACS Catalysis* **2015,** 5, 1804-1825.

8. George, S. M., Atomic Layer Deposition: An Overview. *Chemical Reviews* **2010,** 110, (1), 111-131.

9. Puurunen, R. L., Surface chemistry of atomic layer deposition: A case study for the trimethylaluminum/water process. *Journal of Applied Physics* **2005,** 97, (12), 52.

10. O'Neill, B. J.; Sener, C.; Jackson, D. H. K.; Kuech, T. F.; Dumesic, J. A., Control of Thickness and Chemical Properties of Atomic Layer Deposition Overcoats for Stabilizing Cu/gamma-Al2O3 Catalysts. *Chemsuschem* **2014,** 7, (12), 3247-3251.

11. Alba-Rubio, A. C.; O'Neill, B. J.; Shi, F.; Akatay, C.; Canlas, C.; Li, T.; Winans, R.; Elam, J. W.; Stach, E. A.; Voyles, P. M.; Dumesic, J. A., Pore Structure and Bifunctional Catalyst Activity of Overlayers Applied by Atomic Layer Deposition on Copper Nanoparticles. *Acs Catalysis* **2014,** 4, (5), 1554-1557.

12. Muylaert, I.; Musschoot, J.; Leus, K.; Dendooven, J.; Detavernier, C.; Van der Voort, P., Atomic Layer Deposition of Titanium and Vanadium Oxide on Mesoporous Silica and Phenol/Formaldehyde Resins - the Effect of the Support on the Liquid Phase Epoxidation of Cyclohexene. *European Journal of Inorganic Chemistry* **2012**, (2), 251-260.

13. Sree, S. P.; Dendooven, J.; Koranyi, T. I.; Vanbutsele, G.; Houthoofd, K.; Deduytsche, D.; Detavernier, C.; Martens, J. A., Aluminium atomic layer deposition applied to mesoporous zeolites for acid catalytic activity enhancement. *Catalysis Science & Technology* **2011,** 1, (2), 218-221.

14. Verheyen, E.; Sree, S. P.; Thomas, K.; Dendooven, J.; De Prins, M.; Vanbutsele, G.; Breynaert, E.; Gilson, J. P.; Kirschhock, C. E. A.; Detavernier, C.; Martens, J. A., Catalytic activation of OKO zeolite with intersecting pores of 10-and 12-membered rings using atomic layer deposition of aluminium. *Chemical Communications* **2014,** 50, (35), 4610-4612.

15. Detavernier, C.; Dendooven, J.; Sree, S. P.; Ludwig, K. F.; Martens, J. A., Tailoring nanoporous materials by atomic layer deposition. *Chemical Society Reviews* **2011,** 40, (11), 5242-5253.

16. Feng, H.; Elam, J. W.; Libera, J. A.; Pellin, M. J.; Stair, P. C., Oxidative dehydrogenation of cyclohexane over alumina-supported vanadium oxide nanoliths. *Journal of Catalysis* **2010,** 269, (2), 421-431.

17. Cavani, F.; Trifiro, F.; Vaccari, A., Hydrotalcite-Type Anionic Clays: Preparation, Properties and Applications. *Catalysis Today* **1991,** 11, (2), 173-301.

18. Evans, D. G.; Xue, D. A., Preparation of layered double hydroxides and their applications as additives in polymers, as precursors to magnetic materials and in biology and medicine. *Chemical Communications* **2006**, (5), 485-496.

19. Wang, Q.; Luo, J.; Zhong, Z.; Borgna, A., CO2 capture by solid adsorbents and their applications: current status and new trends. *Energy & Environmental Science* **2011,** 4, (1), 42-55.

20. Davis, R. J., New perspectives on basic zeolites as catalysts and catalyst supports. *Journal of Catalysis* **2003,** 216, (1-2), 396-405.

21. Huang, M.; Adnot, A.; Kaliaguine, S., Cation framework interaction in alkali-cation-exchanged zeolites - An XPS study. *Journal of the American Chemical Society* **1992,** 114, (25), 10005-10010.

22. Zhu, J. H.; Chun, Y. A.; Wang, Y.; Xu, Q. H., Attempts to create new shape-selective solid strong base catalysts. *Catalysis Today* **1999,** 51, (1), 103-111.

23. Martens, L. R. M.; Grobet, P. J.; Jacobs, P. A., Preparation and catalytic properties of ionic-sodium clusters in zeolites. *Nature* **1985,** 315, (6020), 568-570.

24. Suppes, G. J.; Dasari, M. A.; Doskocil, E. J.; Mankidy, P. J.; Goff, M. J., Transesterification of soybean oil with zeolite and metal catalysts. *Applied Catalysis a-General* **2004,** 257, (2), 213-223.

25. Ernst, S.; Hartmann, M.; Sauerbeck, S.; Bongers, T., A novel family of solid basic catalysts obtained by nitridation of crystalline microporous aluminosilicates and aluminophosphates. *Applied Catalysis a-General* **2000,** 200, (1-2), 117-123.

26. Han, A. J.; Guo, J. G.; Yu, H.; Zeng, Y.; Huang, Y. F.; He, H. Y.; Long, Y. C., The leading role of association in framework modification of highly siliceous zeolites with adsorbed methylamine. *Chemphyschem* **2006,** 7, (3), 607-613.

27. Ono, Y.; Baba, T., Selective reactions over solid base catalysts. *Catalysis Today* **1997,** 38, (3), 321-337.

28. Ono, Y., Solid base catalysts for the synthesis of fine chemicals. *Journal of Catalysis* **2003,** 216, (1-2), 406-415.

29. Shen, W.; Tompsett, G. A.; Hammond, K. D.; Xing, R.; Dogan, F.; Grey, C. P.; Conner, W. C., Jr.; Auerbach, S. M.; Huber, G. W., Liquid phase aldol condensation reactions with MgO-ZrO2 and shape-selective nitrogen-substituted NaY. *Applied Catalysis a-General* **2011,** 392, (1-2), 57-68.

30. Faba, L.; Diaz, E.; Ordonez, S., Improvement on the Catalytic Performance of MgZr Mixed Oxides for FurfuralAcetone Aldol Condensation by Supporting on Mesoporous Carbons. *Chemsuschem* **2013,** 6, (3), 463-473.

31. Putkonen, M.; Sajavaara, T.; Niinisto, L., Enhanced growth rate in atomic layer epitaxy deposition of magnesium oxide thin films. *Journal of Materials Chemistry* **2000,** 10, (8), 1857-1861.

32. Putkonen, M.; Nieminen, M.; Niinisto, L., Magnesium aluminate thin films by atomic layer deposition from organometallic precursors and water. *Thin Solid Films* **2004,** 466, (1-2), 103-107.

33. Burton, B. B.; Goldstein, D. N.; George, S. M., Atomic Layer Deposition of MgO Using Bis(ethylcyclopentadienyl)magnesium and H2O. *Journal of Physical Chemistry C* **2009,** 113, (5), 1939-1946.

34. Hatanpaa, T.; Ihanus, J.; Kansikas, J.; Mutikainen, I.; Ritala, M.; Leskela, M., Properties of Mg-2(thd)(4) as a precursor for atomic layer deposition of MgO thin films and crystal structures of Mg-2(thd)(4) and Mg(thd)(2)(EtOH)(2). *Chemistry of Materials* **1999,** 11, (7), 1846-1852.

35. Paglia, G.; Buckley, C. E.; Rohl, A. L.; Hart, R. D.; Winter, K.; Studer, A. J.; Hunter, B. A.; Hanna, J. V., Boehmite derived gamma-alumina system. 1. Structural evolution with temperature, with the identification and structural determination of a new transition phase, gamma '-alumina. *Chemistry of Materials* **2004,** 16, (2), 220-236.

36. Paglia, G.; Buckley, C. E.; Udovic, T. J.; Rohl, A. L.; Jones, F.; Maitland, C. F.; Connolly, J., Boehmite-derived gamma-alumina system. 2. Consideration of hydrogen and surface effects. *Chemistry of Materials* **2004,** 16, (10), 1914-1923.

37. Samain, L.; Jaworski, A.; Eden, M.; Ladd, D. M.; Seo, D. K.; Garcia-Garcia, F. J.; Haussermann, U., Structural analysis of highly porous gamma-Al2O3. *Journal of Solid State Chemistry* **2014,** 217, 1-8.

38. van Ommen, J. R.; Valverde, J. M.; Pfeffer, R., Fluidization of nanopowders: a review. *Journal of Nanoparticle Research* **2012,** 14, (3).

39. Goldstein, D. N.; George, S. M., Surface poisoning in the nucleation and growth of palladium atomic layer deposition with Pd(hfac)(2) and formalin. *Thin Solid Films* **2011,** 519, (16), 5339-5347.

40. Aarik, J.; Aidla, A.; Uustare, T.; Sammelselg, V., Morphology and structure of TiO2 thin-films grown by atomic layer deposition. *Journal of Crystal Growth* **1995,** 148, (3), 268-275.

41. Cullity, B.; Stock, S., *Elements of X-Ray Diffraction*. 3rd ed.; Prentice-Hall Inc.: 2001.

42. Di Cosimo, J. I.; Diez, V. K.; Xu, M.; Iglesia, E.; Apesteguia, C. R., Structure and surface and catalytic properties of Mg-Al basic oxides. *Journal of Catalysis* **1998,** 178, (2), 499-510.

43. Alper, A. M.; McNally, R. N.; Ribbe, P. H.; Doman, R. C., :, The System MgO–$MgAl_2O_4$. In Journal of the American Ceramic Society, 1962; Vol. 45, pp 263–268.

44. Aswal, D. K.; Muthe, K. P.; Tawde, S.; Chodhury, S.; Bagkar, N.; Singh, A.; Gupta, S. K.; Yakhmi, J. V., XPS and AFM investigations of annealing induced surface modifications of MgO single crystals. *Journal of Crystal Growth* **2002,** 236, (4), 661-666.

45. Peng, X. D.; Barteau, M. A., SPECTROSCOPIC CHARACTERIZATION OF SURFACE SPECIES DERIVED FROM HCOOH, CH3COOH, CH3OH, C2H5OH, HCOOCH3, AND C2H2 ON MGO THIN-FILM SURFACES. *Surface Science* **1989,** 224, (1-3), 327-347.

46. Moffitt, C. E.; Chen, B.; Wieliczka, D. M.; Kruger, M. B., XPS comparison between nanocrystalline gamma-alumina and a new high pressure polymorph. *Solid State Communications* **2000,** 116, (11), 631-636.

47. Frederick, B. G.; Apai, G.; Rhodin, T. N., ELECTRONIC AND VIBRATIONAL PROPERTIES OF HYDROXYLATED AND DEHYDROXYLATED THIN AL2O3 FILMS. *Surface Science* **1991,** 244, (1-2), 67-80.

48. Katz, A.; Davis, M. E., Molecular imprinting of bulk, microporous silica. *Nature* **2000,** 403, (6767), 286-289.

49. Hicks, J. C.; Dabestani, R.; Buchanan, A. C., III; Jones, C. W., Assessing site-isolation of amine groups on aminopropyl-functionalized SBA-15 silica materials via spectroscopic and reactivity probes. *Inorganica Chimica Acta* **2008,** 361, (11), 3024-3032.

50. Hicks, J. C.; Dabestani, R.; Buchanan, A. C., III; Jones, C. W., Spacing and site isolation of amine groups in 3-aminopropyl-grafted silica materials: The role of protecting groups. *Chemistry of Materials* **2006,** 18, (21), 5022-5032.

51. Winnik, F. M., Photophysics of Preassociated Pyrenes in Aqueous Polymer-Solutions and in Other Organized Media. *Chemical Reviews* **1993,** 93, (2), 587-614.

52. Roelofs, J.; Lensveld, D. J.; van Dillen, A. J.; de Jong, K. P., On the structure of activated hydrotalcites as solid base catalysts for liquid-phase aldol condensation. *Journal of Catalysis* **2001,** 203, (1), 184-191.

5 Enhanced Activity and Stability of TiO_2-coated Cobalt/Carbon Catalysts for Electrochemical Water Oxidation

Production of hydrogen is an important area of study for power storage and many industrial processes. Cobalt nanoparticles on activated carbon supports (Co/C) were overcoated with TiO_2 deposited by atomic layer deposition (ALD), and studied in the electrochemical oxidation of water. The Co/C catalyst with a TiO_2 overcoating of (ALD(TiO_2)-Co/C) demonstrated 2.5 times higher turnover frequency (TOF) than the Co/C electrocatalyst. The TOF of ALD(TiO_2)-Co/C increased with increasing ALD coating cycle number from 5 to 60. In addition, the stability of the 60 cycle ALD(TiO_2)-Co/C catalyst was enhanced compared to the Co/C catalyst. This work shows how ALD can be used to improve the electrocatalytic water oxidation activity and electrochemical stability of non-precious-metal based catalysts like Co/C.

5.1 Introduction

Water electrolysis ($2H_2O \rightarrow 2H_2 + O_2$) is an important industrial reaction for the production of hydrogen and oxygen.[1-3] The hydrogen produced can be used for powering fuel cells,[4-6] for removing oxygen from biomass,[7-10] or for hydrotreating in the petrochemical industry.[11] Water oxidation for oxygen evolution at the anode ($4OH^- \rightarrow O_2 + 2H_2O + 4e^-$ at high pH) has been recognized as more critical in water electrolysis than the hydrogen evolution reaction at the cathode ($4H_2O + 4e^- \rightarrow 2H_2 + 4OH^-$ at high pH) because it requires a higher overpotential.[1, 2, 12] Pt has been commonly used as an electrocatalyst of its high activity and stability,[1, 2] however it is expensive and has limited earth abundance. Metal oxides have been studied as abundant and cheap replacements for Pt. RuO_2 and IrO_2 have been reported as active electrocatalysts for water oxidation in acidic conditions,[13, 14] although these metal oxides are still rare and expensive. Researchers have investigated non-precious

metal and metal oxide catalysts using metals such as cobalt or nickel, which reduce the necessary overpotential and increase water oxidation activity in alkaline conditions.[15-31] Still, non-precious metal catalysts require substantial progress to enhance their activities and stabilities.

Previous studies have shown that ALD metal oxide (*e.g*, Al_2O_3 or TiO_2) overcoatings can inhibit leaching of non-precious metal nanoparticles such as Cu or Co.[32, 33] It has also been reported that an ALD overcoat of metal oxides can stabilize semiconductor photoelectrodes and increase performance in photoelectrochemical applications.[34-38]

In this study, a thin TiO_2-ALD coating is demonstrated to increase catalytic activity and stability of carbon-supported cobalt catalysts (Co/C) for electrochemical water oxidation. We first prepared the Co/C catalyst by incipient wetness impregnation, then ALD coated the Co/C catalyst with TiO_2 (ALD(TiO_2)-Co/C). The coated catalysts were then activated by a treatment that involved high temperature calcination in air and then reduction under hydrogen. The activity of the ALD(TiO_2)-Co/C electrocatalyst in the water oxidation reaction increases with increasing TiO_2 coating thickness, and at its best shows 2.5 times higher activity than the Co/C catalyst. The stability of the ALD(TiO_2)-Co/C catalyst is enhanced, losing only ~25% of its activity after 8 hours, compared to the Co/C catalyst, which lost ~50% of its activity after 8 hours.

5.2 Discussion

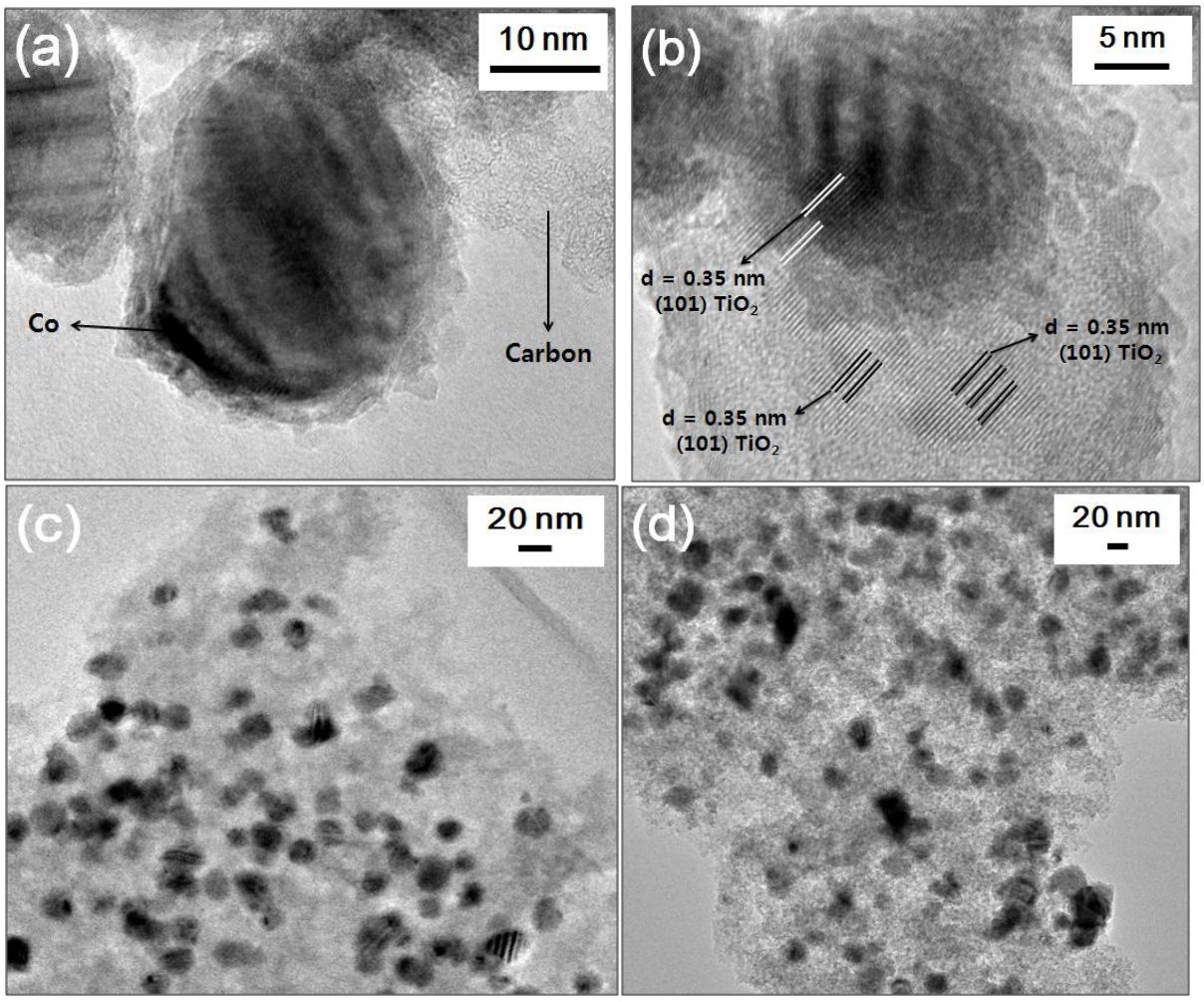

Figure 5.1. High-resolution TEM images of the ALD(TiO_2)-Co/C catalytic system. Catalysts with a thickness of 5 cycles showing (a) oxide decorating a Co nanoparticle and (b) interplanar distance measurement of TiO_2. Catalysts with a coating thickness of (c) 30 cycles and (d) 60 cycles.

Figures 5.1a-d exhibit representative high-resolution transmission electron microscope (HR-TEM) images for structural analysis of ALD(TiO_2)-Co/C catalysts. Mean Co particle sizes were calculated from observation of over 120 particles in the TEM images, and are shown in Table 5.1. The prepared Co/C and ALD(TiO_2)-Co/C catalysts have Co particles of 20±7 nm in size that are distributed on the carbon support. Both the X-ray diffraction (XRD) pattern and the interplanar spacing measurement in Figure 5.1b indicate that anatase is the predominant TiO_2 phase. XRD also detected hexagonal close-packed as the predominant Co

phase in the as-prepared Co/C.[39, 40] Figure 1a also shows that the synthesized catalyst has a surface oxide layer with 2-3 nanometer thickness on Co metal. During the ALD process, the TiO_2 forms a thin film over the cobalt oxide on the exterior of the cobalt particle. After calcination and reduction, the TiO_2 forms pores leaving the Co exposed. In the TiO_2-coated Co/C catalyst, the thin TiO_2 film is thought to decorate the under-coordinated cobalt sites located at defects, corners, and edges which thereby stabilizes the cobalt.[36] The decoration of the Co with TiO_2 is shown in Figure 5.1b showing TiO_2 deposition on both the carbon and the Co particles.

The ALD(TiO_2)-Co/C catalysts were studied for electrocatalytic water oxidation in a three electrode electrochemical cell at room temperature in an aqueous 1M KOH solution. The electrocatalytic results were summarized in Table 5.1. The electrocatalytic performances of all catalysts examined in this study were evaluated in terms of the following five aspects: (1) overpotential (η) = applied potential - thermodynamic potential (E_o = -1.23 V), (2) current divided by geometric electrode area (i_{geo}, glassy carbon: 0.07 cm^2), (3) current divided by entire surface area of the catalyst that was deposited on the glassy carbon electrode ($i_{support}$) (4) current divided by Co metal loading (i_{mass}), and (5) current divided by the number of surface Co atoms (turnover frequency, or TOF)determined by the particle sizes measured by TEM. It is noteworthy that the amount of catalyst loaded on the glassy carbon working electrode (area: *ca.* 0.07 cm^2) was 0.916 mg/cm^2 for all the catalysts tested, although the Co loading on the electrode decreased with the increasing ALD cycles because of titania mass gain (Table 5.1).

Table 5.1. Electrocatalytic activity data for water oxidation at room temperature and in an aqueous 1 M KOH solution.

Catalyst System	Cobalt Loading (Ti/Co mol ratio) [mg/cm^2]	Size[a] [nm]	η[b] @ i_{geo}=10 mA/cm^2 [mV]	i_{geo}[c] @ η=0.40, 0.38V [mA/cm^2]	$i_{support}$[d] @ η=0.40, 0.38V [μA/cm^2]	i_{mass}[e] @ η=0.40, 0.38V [A/g]	TOF[f] @ η=0.40, 0.38V [s^{-1}]
Co/C	0.183	19.1±6.9	425	7.1 (0.40 V)	1.19 (0.40 V)	38.8 (0.40 V)	0.090 (0.40 V)
	(0)			5.3 (0.38 V)	0.89 (0.38 V)	28.9 (0.38 V)	0.065 (0.38 V)
05ALD(TiO_2)-Co/C	0.144	20.4±5.3	411	8.6 (0.40 V)	1.84 (0.40 V)	59.9 (0.40 V)	0.154 (0.40 V)
	(0.33)			6.4 (0.38 V)	1.37 (0.38 V)	44.6 (0.38 V)	0.114 (0.38 V)
30ALD(TiO_2)-Co/C	0.120	21.0±7.9	402	9.5 (0.40 V)	2.44 (0.40 V)	79.4 (0.40 V)	0.209 (0.40 V)
	(0.65)			6.3 (0.38 V)	1.62 (0.38 V)	52.7 (0.38 V)	0.139 (0.38 V)
60ALD(TiO_2)-Co/C	0.112	20.3±7.7	398	10.1 (0.40 V)	2.79 (0.40 V)	90.2 (0.40 V)	0.230 (0.40 V)
	(0.79)			6.8 (0.38 V)	1.89 (0.38 V)	61.1 (0.38 V)	0.156 (0.38 V)

[a] Mean particle size calculated from observation of 120 particles in the TEM images; [b] η (overpotential) = applied potential - thermodynamic potential; [c] i_{geo} = current divided by geometric electrode area (glassy carbon: 0.07 cm^2); [d] $i_{support}$ = current divided by surface area of the carbon support that was deposited on the glassy carbon electrode; [e] i_{mass} = current divided by Co metal loading (g) on the glassy carbon electrode; [f] TOF = turnover frequency for oxygen evolution assuming that every Co surface atom is catalytically active and Faradaic efficiency is 100%, which indicates the rate of electron delivery per surface cobalt atom per second.

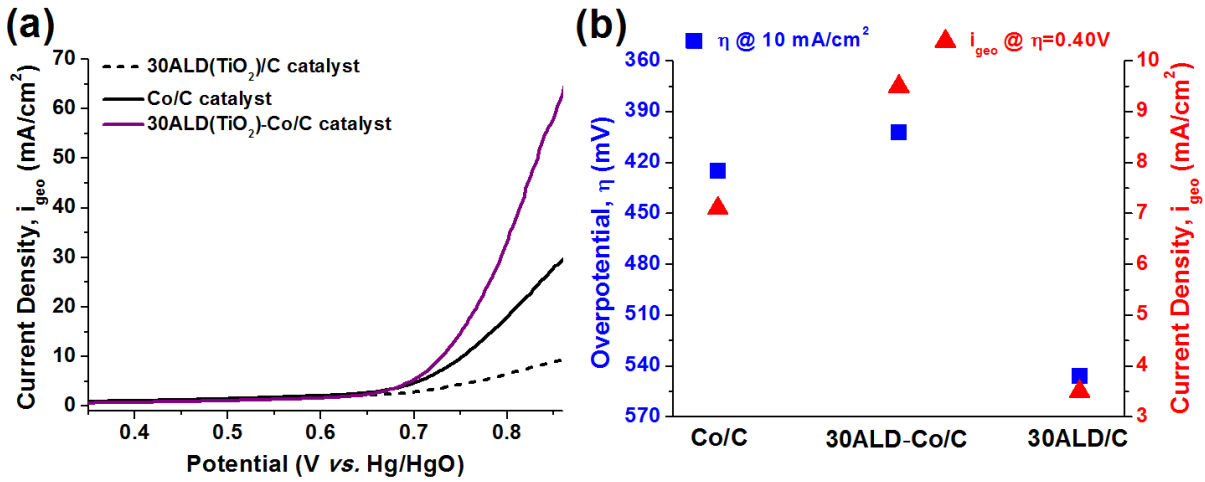

Figure 5.2. Electrocatalytic water oxidation activity of Co/C and ALD(TiO_2)-Co/C catalysts. (a) LSV curves of Co/C, 30 cycle ALD(TiO_2)/C and 30 cycle ALD(TiO_2)-Co/C. (b) Comparisons of η at i_{geo} = 10 mA/cm^2 and i_{geo} at η = 0.4 V for Co/C, 30 cycle ALD(TiO_2)/C and 30 cycle ALD(TiO_2)-Co/C.

In Figures 5.2 and 5.3, the catalytic activity of the Co/C and ALD(TiO_2)-Co/C catalysts were examined by linear sweep voltammetry (LSV). The scan potential was from 0 to 0.9 V (vs. Hg/HgO) at a scan rate of 5 mV s^{-1}. In Figure 2, 30 cycle ALD(TiO_2)/C had very low activity in terms of i_{geo} at η = 0.4 V and η at i_{geo} = 10 mA/cm^2 compared to the Co/C catalyst. This could be expected from previous literature demonstrating that TiO_2 binds O and OH weakly, a characteristic that is associated with low water oxidation activity.[13] The 30 cycle ALD(TiO_2)Co/C catalyst demonstrated higher i_{geo} at η = 0.4 V (also 2 times higher i_{mass}) and lower η at i_{geo} = 10 mA/cm^2 than the Co/C catalyst for the reaction. This result suggests that interactions between Co and TiO_2 in the TiO_2 coated Co/C catalyst leads to improved catalytic activity. In Figure 5.3 and Table 5.1, the catalytic performances of ALD(TiO_2)-Co/C catalysts increased with increasing ALD-TiO_2 coating cycle number from 5 to 60. The η at i_{geo} = 10 mA/cm^2 for all ALD(TiO_2)-Co/C catalysts were lower than for the Co/C catalyst. As shown in Figure 3a, the i_{geo} of the ALD(TiO_2)-Co/C catalysts for electrocatalytic water oxidation

decreased in the following order: 60 cycle ALD(TiO_2)-Co/C > 30 cycle ALD(TiO_2)-Co/C > 5 cycle ALD(TiO_2)-Co/C. Figure 5.3b shows changes of Ti/Co molar ratio and TOF according to ALD coating cycle. As shown in Figure 5.3b, the TOFs of ALD(TiO_2)-Co/C catalysts increased with increasing Ti/Co molar ratio (and with increasing ALD coating cycles). Figures 5.3c shows Tafel plots of Co/C and ALD(TiO_2)-Co/C catalysts, which indicate the electron efficiency in water electrolysis. Figure 3d

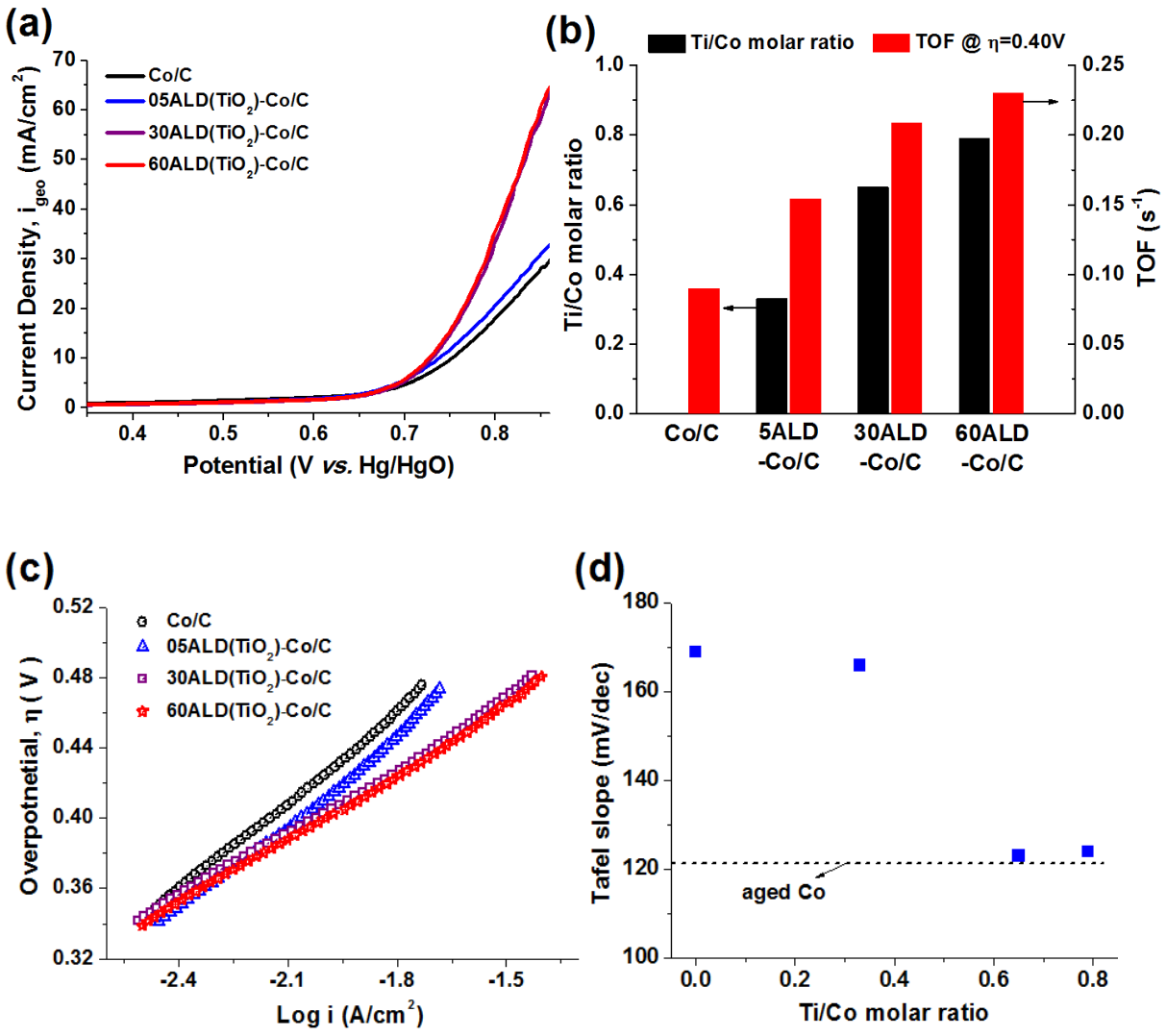

Figure 5.3. Effect of ALD coating cycle number on ALD(TiO_2)-Co/C for electrocatalytic water oxidation. (a) LSV curves of ALD(TiO_2)-Co/C with different ALD coating cycle number. (b) Changes of Ti/Co molar ratio and TOF

according to ALD coating cycle number. (c) Tafel plots of Co/C and ALD(TiO_2)-Co/C catalysts. (d) Change of Tafel slopes with Ti/Co molar ratio. The dashed line indicates a Tafel slope of 122 mV/dec for aged Co electrode (surface oxidized Co by an electrochemical treatment) and are shown for reference.

shows the change of Tafel slopes with Ti/Co molar ratio. For the uncoated Co/C catalyst, a Tafel slope of 169 mV/dec was calculated which agrees with the values calculated from the previous experiments with cobalt electrodes.[41, 42] The Tafel slopes for ALD(TiO_2)-Co/C catalysts decreased with increasing Ti/Co ratios. The Tafel slope at the highest Ti/Co ratio was similar to the reported Tafel slope (122 mV/dec) for an aged Co electrode that was surface-oxidized by an electrochemical treatment.[42] The 60 cycle ALD(TiO_2)-Co/C had the lowest Tafel slope and largest i_{geo}, $i_{support}$, i_{mass}, and TOF among the tested catalysts.

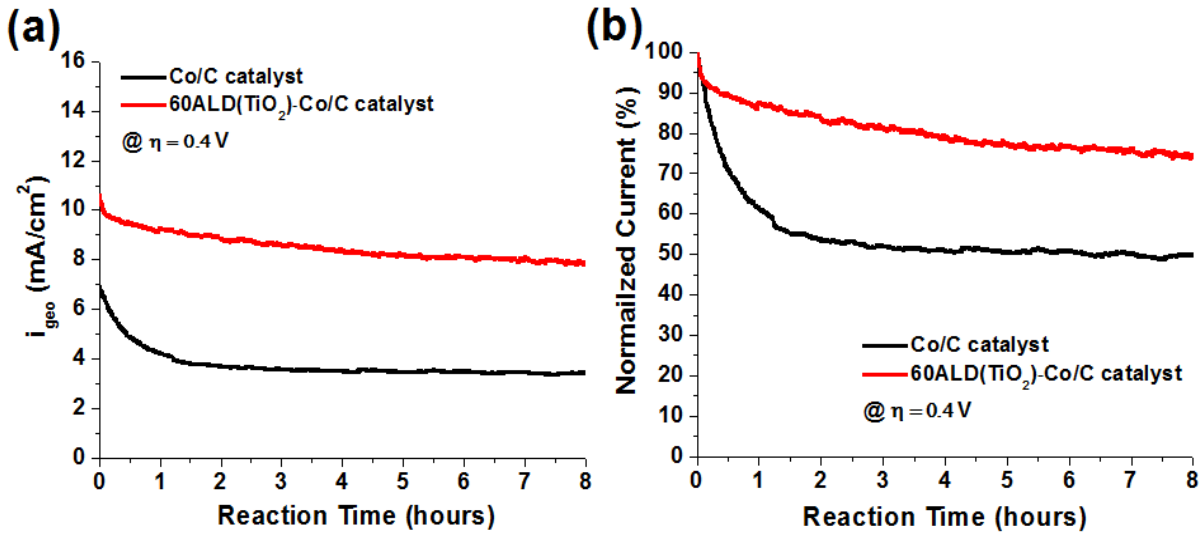

Figure 5.4. Stability tests of Co/C and 60 cycle ALD(TiO_2)-Co/C for electrocatalytic water oxidation at η=0.4 V for 8 hours. (a) chronoamperometry measurements (i_{geo} *vs.* reaction time) and (b) chronoamperometric responses (% of initial current *vs.* reaction time) using rotating disk electrode at a rotation speed of 1600 rpm.

To investigate electrocatalyst stability during water oxidation, chronoamperometry measurements were performed using a rotating disk electrode (rotation speed: 1600 rpm) on the

Co/C and the 60 cycle ALD(TiO_2)-Co/C catalysts at η = 0.4 V for 8 hours. In Figure 5.4a, the steady-state i_{geo} of 60 cycle ALD(TiO_2)-Co/C was found to be stable compared to that of the Co/C. Figure 4b show both currents normalized to their initial value and confirms that the stability of 60 cycle ALD(TiO_2)-Co/C was improved (only ~25% activity loss after 8 hours) compared to the Co/C catalyst (~50% activity loss after 8 hours). Additional TEM analysis was conducted to understand why ALD(TiO_2)-Co/C had a higher stability than to the uncoated Co/C. After the electrochemical stability test, the cobalt particle size of the Co/C increased from 19.1 ± 6.9 nm to 34.5 ± 13.1 nm. However, the cobalt particle size of the used 60ALD(TiO_2)-Co/C (22.1 ± 8.5 nm) did not statistically change from fresh 60ALD(TiO_2)-Co/C (20.3 ± 7.7 nm). In addition, the cobalt loadings of Co/C and 60ALD(TiO_2)-Co/C after the electrochemical stability test did not change compared to those of the fresh Co/C and 60ALD(TiO_2)-Co/C. It has been also reported that the Co nanoparticle catalysts are stable towards dissolution during electrolysis in alkaline solution.[17] This result suggests that the stability enhancement by ALD coating is due to preventing the catalyst from sintering rather than the catalyst leaching during the electrochemical water oxidation. It has been observed that sintering or leaching of metal nanoparticles begins at under-coordinated metal atoms located at defect, corner, and edge sites.[32, 43] Recently, we have reported that the thin TiO_2 overcoating probably decorates these under-coordinated cobalt sites located at defects, corners, and edges which thereby prevents the sintering or leaching of cobalt.[33]

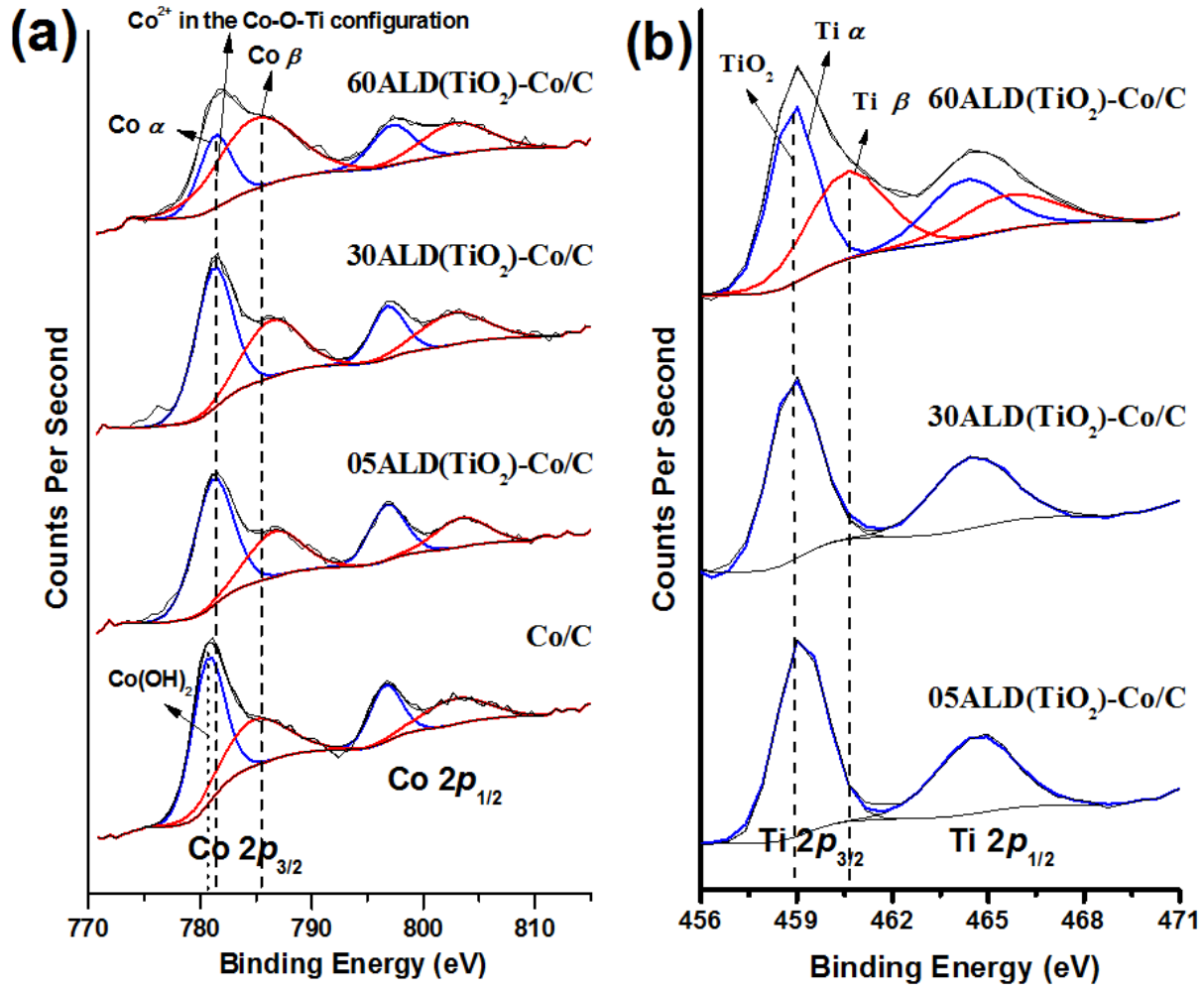

Figure 5.5. XPS analysis of the prepared ALD(TiO_2)-Co/C catalysts. X-ray photoelectron spectra of (a) Co(2*p*) and (b) Ti(2*p*) for the ALD(TiO_2)-Co/C catalysts.

XPS analysis was conducted to elucidate the surface species present on the Co/C and ALD(TiO_2)-Co/C catalysts. Figure 5.5 shows high resolution XPS spectra of the Co 2*p* and Ti 2*p* regions. In the as-made Co/C catalyst, the Co $2p_{3/2}$ peak has a binding energy (BE) of 780.7 eV which is attributed to $Co(OH)_2$ species.[44, 45] The BE of the Co $2p_{3/2}$ peak in the ALD(TiO_2)-Co/C catalysts is 781.3 eV, higher than that of the Co $2p_{3/2}$ peak indicating $Co(OH)_2$, and is similar to that observed in 5% Co doped in TiO_2 (781.5 eV).[46] The Co peak at 781.3 eV in the ALD(TiO_2)-

Co/C catalysts has also been attributed to Co^{2+} in the Co-O-Ti phase.[47] This peak at 781.3 eV has a BE lower than that of Co^{2+} in a CoO phase.[47] This can be explained by the weakening of the Co-O bond because of the formation of Co-O-Ti configuration.[47] Additionally, the Co $2p_{3/2}$ region has two components, a primary peak denoted as Co α and a satellite peak denoted as Co β. The α/β peak area ratio of has been reported to decrease with increasing Co loading on TiO_2 caused by interaction between Co and TiO_2.[46] This ratio decreased as the TiO_2 loading increased for the ALD(TiO_2)-Co/C catalysts. It has been reported that the rate-limiting step in water oxidation is the reaction of an adsorbed OH^- anion with an adsorbed O atom to form OOH species.[13, 18, 20, 48] The catalytic water oxidation activity can be increased by modifying the BE of O or OH species on the surface.[13, 48-50] The formation of Co-O-Ti configuration mediated by the interaction between Co and TiO_2 may change the surface BE of O or OH species on the catalyst, thereby facilitating the formation of O-OH, which could enhance the activity of water oxidation.

The Co BE of the TiO_2 overcoated Co/C catalysts shifts to higher BE as after ALD overcoating, reflecting enhanced oxidation of the surface Co oxide by TiO_2.[45] The large observed peak widths of Co β with increasing TiO_2 coating suggests that other species, such as Co(III) or Co(IV), may be present on the catalysts samples. Co_3O_4 is more active than CoO for the oxygen evolution reaction.[17] It is also known that the activity of cobalt catalysts for water oxidation could be enhanced by increasing the population of Co^{4+} species present in the oxide.[17, 18, 41, 51-53] It has been postulated that the Co^{4+} species improve the electrophilicity of the adsorbed O, which is likely to promote the formation of O-OH *via* nucleophilic attack by an OH^- anion with an O atom associated with Co^{4+} species.[18, 53] The enhancement in catalytic water oxidation activity on TiO_2 overcoated Co/C catalysts may be related to the role of TiO_2 in facilitating the oxidation of surface Co oxide. From these XPS results and the observation of kinetic parameters, we

hypothesize that the TiO_2 overcoating on a Co/C catalyst changes the nature of the active sites, thereby promoting the formation of O-OH (known as the rate-limiting step for the reaction) more effectively, which would improve the water oxidation activity. In Figure 5b, the BE (458.9 eV) of Ti $2p_{3/2}$ peak in the ALD(TiO_2)-Co/C catalysts is attributed to TiO_2.[47, 54] Only in the 60 cycle ALD(TiO_2)-Co/C catalyst, the Ti $2p_{3/2}$ peak has two components of Ti α and Ti β. There is little record of a Ti β peak at this high binding energy (460.5 eV) in the literature. It has been attributed to band bending caused near the metal-TiO_2 interface.[55-57]

5.3 Conclusion

TiO_2-coated Co/C catalysts prepared by ALD were used to study the effects of the TiO_2 overcoating on Co/C catalysts for electrochemical water oxidation. The catalytic activity of the ALD(TiO_2)-Co/C catalyst increased with increasing ALD-TiO_2 coating cycle number from 5 to 60 cycles. The 60 cycle ALD(TiO_2)-Co/C catalyst showed 2.5 times higher TOF than the Co/C catalyst. The improvement in activity is attributed to formation of highly oxidized Co^{3+} or possibly Co^{4+}. In addition, the 60 cycle ALD(TiO_2)-Co/C was found to be highly stable compared to Co/C. The stability improvement is attributed to the overcoating preventing sintering of Co nanoparticles. This work shows how the ALD technique can be used to enhance catalytic activity and stability of non-precious metal catalysts for electrochemical water oxidation. This study also paves the way for future catalyst design in electrochemical applications such as fuel cells and electrolyzers.

5.4 References

1. Turner, J.; Sverdrup, G.; Mann, M. K.; Maness, P. C.; Kroposki, B.; Ghirardi, M.; Evans, R. J.; Blake, D., Renewable hydrogen production. *International Journal of Energy Research* **2008,** 32, (5), 379-407.

2. Holladay, J. D.; Hu, J.; King, D. L.; Wang, Y., An overview of hydrogen production technologies. *Catalysis Today* **2009,** 139, (4), 244-260.

3. Spurgeon, J. M.; Lewis, N. S., Proton exchange membrane electrolysis sustained by water vapor. *Energy & Environmental Science* **2011,** 4, (8), 2993-2998.

4. Jaouen, F.; Proietti, E.; Lefevre, M.; Chenitz, R.; Dodelet, J. P.; Wu, G.; Chung, H. T.; Johnston, C. M.; Zelenay, P., Recent advances in non-precious metal catalysis for oxygen-reduction reaction in polymer electrolyte fuel cells. *Energy & Environmental Science* **2011,** 4, (1), 114-130.

5. Durst, J.; Siebel, A.; Simon, C.; Hasche, F.; Herranz, J.; Gasteiger, H. A., New insights into the electrochemical hydrogen oxidation and evolution reaction mechanism. *Energy & Environmental Science* **2014,** 7, (7), 2255-2260.

6. Hunt, S. T.; Nimmanwudipong, T.; Roman-Leshkov, Y., Engineering Non-sintered, Metal-Terminated Tungsten Carbide Nanoparticles for Catalysis. *Angewandte Chemie-International Edition* **2014,** 53, (20), 5131-5136.

7. Huber, G. W.; Chheda, J. N.; Barrett, C. J.; Dumesic, J. A., Production of liquid alkanes by aqueous-phase processing of biomass-derived carbohydrates. *Science* **2005,** 308, (5727), 1446-1450.

8. Vispute, T. P.; Zhang, H. Y.; Sanna, A.; Xiao, R.; Huber, G. W., Renewable Chemical Commodity Feedstocks from Integrated Catalytic Processing of Pyrolysis Oils. *Science* **2010,** 330, (6008), 1222-1227.

9. Prasomsri, T.; Nimmanwudipong, T.; Roman-Leshkov, Y., Effective hydrodeoxygenation of biomass-derived oxygenates into unsaturated hydrocarbons by MoO3 using low H-2 pressures. *Energy & Environmental Science* **2013,** 6, (6), 1732-1738.

10. Lee, J.; Kim, Y. T.; Huber, G. W., Aqueous-phase hydrogenation and hydrodeoxygenation of biomass-derived oxygenates with bimetallic catalysts. *Green Chemistry* **2014,** 16, (2), 708-718.

11. Marcilly, C., Present status and future trends in catalysis for refining and petrochemicals. *Journal of Catalysis* **2003,** 216, (1-2), 47-62.

12. Zeng, K.; Zhang, D., Recent progress in alkaline water electrolysis for hydrogen production and applications. *Progress in Energy and Combustion Science* **2010,** 36, (3), 307-326.

13. Rossmeisl, J.; Qu, Z. W.; Zhu, H.; Kroes, G. J.; Norskov, J. K., Electrolysis of water on oxide surfaces. *Journal of Electroanalytical Chemistry* **2007,** 607, (1-2), 83-89.

14. Gorlin, Y.; Jaramillo, T. F., A Bifunctional Nonprecious Metal Catalyst for Oxygen Reduction and Water Oxidation. *Journal of the American Chemical Society* **2010,** 132, (39), 13612-13614.

15. Esswein, A. J.; McMurdo, M. J.; Ross, P. N.; Bell, A. T.; Tilley, T. D., Size-Dependent Activity of Co3O4 Nanoparticle Anodes for Alkaline Water Electrolysis. *Journal of Physical Chemistry C* **2009,** 113, (33), 15068-15072.

16. Jiao, F.; Frei, H., Nanostructured cobalt and manganese oxide clusters as efficient water oxidation catalysts. *Energy & Environmental Science* **2010,** 3, (8), 1018-1027.

17. Chou, N. H.; Ross, P. N.; Bell, A. T.; Tilley, T. D., Comparison of Cobalt-based Nanoparticles as Electrocatalysts for Water Oxidation. *ChemSusChem* **2011,** 4, (11), 1566-1569.

18. Yeo, B. S.; Bell, A. T., Enhanced Activity of Gold-Supported Cobalt Oxide for the Electrochemical Evolution of Oxygen. *Journal of the American Chemical Society* **2011,** 133, (14), 5587-5593.

19. Liang, Y. Y.; Li, Y. G.; Wang, H. L.; Zhou, J. G.; Wang, J.; Regier, T.; Dai, H. J., Co3O4 nanocrystals on graphene as a synergistic catalyst for oxygen reduction reaction. *Nature Materials* **2011,** 10, (10), 780-786.

20. Garcia-Mota, M.; Bajdich, M.; Viswanathan, V.; Vojvodic, A.; Bell, A. T.; Norskov, J. K., Importance of Correlation in Determining Electrocatalytic Oxygen Evolution Activity on Cobalt Oxides. *Journal of Physical Chemistry C* **2012,** 116, (39), 21077-21082.

21. Louie, M. W.; Bell, A. T., An Investigation of Thin-Film Ni-Fe Oxide Catalysts for the Electrochemical Evolution of Oxygen. *Journal of the American Chemical Society* **2013,** 135, (33), 12329-12337.

22. McCrory, C. C. L.; Jung, S. H.; Peters, J. C.; Jaramillo, T. F., Benchmarking Heterogeneous Electrocatalysts for the Oxygen Evolution Reaction. *Journal of the American Chemical Society* **2013,** 135, (45), 16977-16987.

23. Ahn, H. S.; Tilley, T. D., Electrocatalytic Water Oxidation at Neutral pH by a Nanostructured Co(PO3)2 Anode. *Advanced Functional Materials* **2013,** 23, (2), 227-233.

24. Mao, S.; Wen, Z. H.; Huang, T. Z.; Hou, Y.; Chen, J. H., High-performance bi-functional electrocatalysts of 3D crumpled graphene-cobalt oxide nanohybrids for oxygen reduction and evolution reactions. *Energy & Environmental Science* **2014,** 7, (2), 609-616.

25. Gao, M. R.; Sheng, W. C.; Zhuang, Z. B.; Fang, Q. R.; Gu, S.; Jiang, J.; Yan, Y. S., Efficient Water Oxidation Using Nanostructured alpha-Nickel-Hydroxide as an Electrocatalyst. *Journal of the American Chemical Society* **2014,** 136, (19), 7077-7084.

26. Deng, X.; Tüysüz, H., Cobalt-Oxide-Based Materials as Water Oxidation Catalyst: Recent Progress and Challenges. *Acs Catalysis* **2014,** 4, (10), 3701-3714.

27. Surendranath, Y.; Kanan, M. W.; Nocera, D. G., Mechanistic Studies of the Oxygen Evolution Reaction by a Cobalt-Phosphate Catalyst at Neutral pH. *Journal of the American Chemical Society* **2010,** 132, (46), 16501-16509.

28. Surendranath, Y.; Dincă, M.; Nocera, D. G., Electrolyte-Dependent Electrosynthesis and Activity of Cobalt-Based Water Oxidation Catalysts. *Journal of the American Chemical Society* **2009,** 131, (7), 2615-2620.

29. Kanan, M. W.; Nocera, D. G., In Situ Formation of an Oxygen-Evolving Catalyst in Neutral Water Containing Phosphate and Co2+. *Science* **2008,** 321, (5892), 1072-1075.

30. Blakemore, J. D.; Gray, H. B.; Winkler, J. R.; Müller, A. M., Co3O4 Nanoparticle Water-Oxidation Catalysts Made by Pulsed-Laser Ablation in Liquids. *ACS Catalysis* **2013,** 3, (11), 2497-2500.

31. Grzelczak, M.; Zhang, J.; Pfrommer, J.; Hartmann, J.; Driess, M.; Antonietti, M.; Wang, X., Electro- and Photochemical Water Oxidation on Ligand-free Co3O4 Nanoparticles with Tunable Sizes. *ACS Catalysis* **2013,** 3, (3), 383-388.

32. O'Neill, B. J.; Jackson, D. H. K.; Crisci, A. J.; Farberow, C. A.; Shi, F.; Alba-Rubio, A. C.; Lu, J.; Dietrich, P. J.; Gu, X.; Marshall, C. L.; Stair, P. C.; Elam, J. W.; Miller, J. T.; Ribeiro, F. H.; Voyles, P. M.; Greeley, J.; Mavrikakis, M.; Scott, S. L.; Kuech, T. F.; Dumesic, J. A., Stabilization of Copper Catalysts for Liquid-Phase Reactions by Atomic Layer Deposition. *Angewandte Chemie-International Edition* **2013,** 52, (51), 13808-13812.

33. Lee, J.; Jackson, D. H. K.; Li, T.; Winans, R. E.; Dumesic, J. A.; Kuech, T. F.; Huber, G. W., Enhanced stability of cobalt catalysts by atomic layer deposition for aqueous-phase reactions. *Energy & Environmental Science* **2014,** 7, (5), 1657-1660.

34. Chen, Y. W.; Prange, J. D.; Duehnen, S.; Park, Y.; Gunji, M.; Chidsey, C. E. D.; McIntyre, P. C., Atomic layer-deposited tunnel oxide stabilizes silicon photoanodes for water oxidation. *Nature Materials* **2011,** 10, (7), 539-544.

35. Scheuermann, A. G.; Prange, J. D.; Gunji, M.; Chidsey, C. E. D.; McIntyre, P. C., Effects of catalyst material and atomic layer deposited TiO2 oxide thickness on the water oxidation performance of metal-insulator-silicon anodes. *Energy & Environmental Science* **2013,** 6, (8), 2487-2496.

36. Lichterman, M. F.; Shaner, M. R.; Handler, S. G.; Brunschwig, B. S.; Gray, H. B.; Lewis, N. S.; Spurgeon, J. M., Enhanced Stability and Activity for Water Oxidation in Alkaline Media with Bismuth Vanadate Photoelectrodes Modified with a Cobalt Oxide Catalytic Layer Produced by Atomic Layer Deposition. *Journal of Physical Chemistry Letters* **2013,** 4, (23), 4188-4191.

37. Hu, S.; Shaner, M. R.; Beardslee, J. A.; Lichterman, M.; Brunschwig, B. S.; Lewis, N. S., Amorphous TiO2 coatings stabilize Si, GaAs, and GaP photoanodes for efficient water oxidation. *Science* **2014,** 344, (6187), 1005-1009.

38. Yang, J.; Walczak, K.; Anzenberg, E.; Toma, F. M.; Yuan, G.; Beeman, J.; Schwartzberg, A.; Lin, Y.; Hettick, M.; Javey, A.; Ager, J. W.; Yano, J.; Frei, H.; Sharp, I. D.,

Efficient and Sustained Photoelectrochemical Water Oxidation by Cobalt Oxide/Silicon Photoanodes with Nanotextured Interfaces. *Journal of the American Chemical Society* **2014,** 136, (17), 6191-6194.

39. Yang, Q.; Choi, H.; Dionysiou, D. D., Nanocrystalline cobalt oxide immobilized on titanium dioxide nanoparticles for the heterogeneous activation of peroxymonosulfate. *Applied Catalysis B-Environmental* **2007,** 74, (1-2), 170-178.

40. Zhou, H. C.; Song, J. L.; Fan, H. L.; Zhang, B. B.; Yang, Y. Y.; Hu, J. Y.; Zhu, Q. G.; Han, B. X., Cobalt catalysts: very efficient for hydrogenation of biomass-derived ethyl levulinate to gamma-valerolactone under mild conditions. *Green Chemistry* **2014,** 16, (8), 3870-3875.

41. Palmas, S.; Ferrara, F.; Vacca, A.; Mascia, M.; Polcaro, A. M., Behavior of cobalt oxide electrodes during oxidative processes in alkaline medium. *Electrochimica Acta* **2007,** 53, (2), 400-406.

42. Lyons, M. E. G.; Brandon, M. P., A comparative study of the oxygen evolution reaction on oxidised nickel, cobalt and iron electrodes in base. *Journal of Electroanalytical Chemistry* **2010,** 641, (1-2), 119-130.

43. Greeley, J., Structural effects on trends in the deposition and dissolution of metal-supported metal adstructures. *Electrochimica Acta* **2010,** 55, (20), 5545-5550.

44. Yang, J.; Liu, H.; Martens, W. N.; Frost, R. L., Synthesis and Characterization of Cobalt Hydroxide, Cobalt Oxyhydroxide, and Cobalt Oxide Nanodiscs. *Journal of Physical Chemistry C* **2010,** 114, (1), 111-119.

45. Biesinger, M. C.; Payne, B. P.; Grosvenor, A. P.; Lau, L. W. M.; Gerson, A. R.; Smart, R. S. C., Resolving surface chemical states in XPS analysis of first row transition metals, oxides and hydroxides: Cr, Mn, Fe, Co and Ni. *Applied Surface Science* **2011,** 257, (7), 2717-2730.

46. Lim, S. H.; Ferraris, C.; Schreyer, M.; Shih, K.; Leckie, J. O.; White, T. J., The influence of cobalt doping on photocatalytic nano-titania: Crystal chemistry and amorphicity. *Journal of Solid State Chemistry* **2007,** 180, (10), 2905-2915.

47. O'Shea, V. A. D.; Galvan, M. C. A.; Prats, A. E. P.; Campos-Martin, J. M.; Fierro, J. L. G., Direct evidence of the SMSI decoration effect: the case of Co/TiO2 catalyst. *Chemical Communications* **2011,** 47, (25), 7131-7133.

48. Rossmeisl, J.; Logadottir, A.; Norskov, J. K., Electrolysis of water on (oxidized) metal surfaces. *Chemical Physics* **2005,** 319, (1-3), 178-184.

49. Garcia-Mota, M.; Vojvodic, A.; Metiu, H.; Man, I. C.; Su, H. Y.; Rossmeisl, J.; Norskov, J. K., Tailoring the Activity for Oxygen Evolution Electrocatalysis on Rutile TiO2(110) by Transition-Metal Substitution. *ChemCatChem* **2011,** 3, (10), 1607-1611.

50. Bajdich, M.; Garcia-Mota, M.; Vojvodic, A.; Norskov, J. K.; Bell, A. T., Theoretical Investigation of the Activity of Cobalt Oxides for the Electrochemical Oxidation of Water. *Journal of the American Chemical Society* **2013,** 135, (36), 13521-13530.

51. Casella, I. G.; Gatta, M., Study of the electrochemical deposition and properties of cobalt oxide species in citrate alkaline solutions. *Journal of Electroanalytical Chemistry* **2002,** 534, (1), 31-38.

52. Lyons, M. E. G.; Brandon, M. P., The Oxygen Evolution Reaction on Passive Oxide Covered Transition Metal Electrodes in Alkaline Solution Part II - Cobalt. *International Journal of Electrochemical Science* **2008,** 3, (12), 1425-1462.

53. Gerken, J. B.; McAlpin, J. G.; Chen, J. Y. C.; Rigsby, M. L.; Casey, W. H.; Britt, R. D.; Stahl, S. S., Electrochemical Water Oxidation with Cobalt-Based Electrocatalysts from pH 0-14: The Thermodynamic Basis for Catalyst Structure, Stability, and Activity. *Journal of the American Chemical Society* **2011,** 133, (36), 14431-14442.

54. Lewera, A.; Timperman, L.; Roguska, A.; Alonso-Vante, N., Metal-Support Interactions between Nanosized Pt and Metal Oxides (WO3 and TiO2) Studied Using X-ray Photoelectron Spectroscopy. *Journal of Physical Chemistry C* **2011,** 115, (41), 20153-20159.

55. Abe, T.; Suzuki, E.; Nagoshi, K.; Miyashita, K.; Kaneko, M., Electron source in photoinduced hydrogen production on Pt-supported TiO2 particles. *Journal of Physical Chemistry B* **1999,** 103, (7), 1119-1123.

56. Perkins, C. L.; Henderson, M. A.; McCready, D. E.; Herman, G. S., Comment on "Electron source in photoinduced hydrogen production on Pt-supported TiO2 particles". *Journal of Physical Chemistry B* **2001,** 105, (2), 595-596.

57. Abe, T.; Suzuki, E.; Nagoshi, K.; Miyashita, K.; Kaneko, M., Reply to the comment on "Electron source in photoinduced hydrogen production on Pt-supported TiO2 particles". *Journal of Physical Chemistry B* **2001,** 105, (2), 597-597.

6 Electrochemical effects of annealing on atomic layer deposited Al_2O_3 coatings on $LiNi_{0.5}Mn_{0.3}Co_{0.2}O_2$

This study investigated the annealing of ALD Al_2O_3-coated Li-ion battery cathodes to enhance the materials electrochemical properties by inducing chemical, electronic and morphological changes. $LiNi_{0.5}Mn_{0.3}Co_{0.2}O_2$ (NMC) cathode powders were coated with 5 ALD cycles at 100 °C, annealed between 300 and 700 °C, cast into electrode sheets and assembled into coin cells. Cells were characterized using charge-discharge cycling, electrochemical impedance spectroscopy, pre-casting and postmortem X-ray photoelectron spectroscopy, charge endpoint slippage measurement, and an elevated temperature storage test. Cell performance and solid-electrolyte interphase properties exhibit relationships with cathode surface properties, which are dependent on annealing temperature. Diffusion of Al into bulk NMC was observable at ≥500 °C, and increased with increasing temperature. High quantities of surface species that formed LiF were detected in cells annealed at 500 °C, and may be responsible for these cells exhibiting the best all-around performance. Un-annealed ALD-coated cathodes showed exceptional capacity retention at high charge-discharge rates. This study approaches post-deposition annealing temperature as a parameter that may be used to explore the electrochemical properties of ALD-coated battery cathodes.

6.1 Introduction

Li-ion batteries play an important role in modern society, with applications in portable electronics, power tools, and electrified vehicles.[1] The broad goals of energy storage technologies, including batteries, are to improve power density, energy density and lifetime. To achieve these goals, much battery research focuses on developing next generation technologies such as Li-air, and also on the further development of commercially used electrodes, such as the

$LiNi_xMn_yCo_{1-x-y}O_2$ cathode.[2, 3] This study is targeted towards the enhancement of the coin cell performance characteristics of $LiNi_{0.5}Mn_{0.3}Co_{0.2}O_2$ (NMC), which serve as an experimental study applicable to other battery configurations.

The parasitic reactions that occur within a cell during operation are some of the major causes attributed to the loss of charge capacity.[4] These parasitic reactions act to remove Li^+ from the redox cycle, increase cell impedance, and degrade the electrode crystals that act as a host matrix for Li^+ ions.[4] Increased cell impedance is caused by a solid electrolyte interphase (SEI) that forms at the electrode surface via the continuous decomposition of the electrolyte during cycling. The SEI impedes Li-ions from entering the electrode, resulting in reduced cell energy density.

ALD coating of cell components has demonstrated utility in improving battery performance to a significant degree.[5-7] Coatings materials are typically composed of Al_2O_3, ZrO_2, or other oxides, and the improved battery performance they yield is attributed to their mechanical stability and the ability to block electron transfer to prevent electrolyte decomposition.[5-7]

Studies into ALD-coated Li-ion battery materials have largely focused on “as-deposited” coatings and not on annealed coatings. Limited studies touching on the effects of post-deposition annealing exist, and have described the approach as cathode surface doping.[8] Post-deposition annealing has been more thoroughly studied in applications such as catalysis[9, 10] and semiconductors.[11, 12] Annealing allows for the activation of new film properties by inducing chemical, morphological and electronic changes. This present study systematically investigated

the effects of post-deposition annealing of ALD-coated NMC on the electrochemical performance of Li-ion batteries.

6.2 Results

Coated and annealed NMC powders were examined by XPS with the results collected in Figure 6.1. Annealing temperature shows a negative correlation with both Al 2*p* peak area and peak position (Al 2*s* peaks exhibited identical trends and are not shown). Figure 6.1a shows the XPS spectra of the Al 2*p* region, with both peak shifts and intensity changes apparent. Figure 6.1b shows the Al 2*p* peak position versus temperature, exhibiting a negative linear relationship. Al 2*p* peak positions shifted to lower binding energies, away from the tabulated values for Al in sapphire,[13] and towards the tabulated values reported for Al metal.[13] At higher temperatures, the Al bonding changes from more ionic in nature to more a covalent, metallic system, such as one with a smaller band gap than sapphire. NMC is a semiconductor so stronger interaction of Al with the layered NMC structure would account for the binding energy shift observed. Figure 6.1c shows the Al/Co ratios, where Al 2*p* peak areas are divided by the areas of the Co 2*p* peaks for the purpose of internal referencing. The Al/Co value represents the overall amount of Al at and just below the NMC surface. Unlike peak position, Al/Co does not have a linear relationship to temperature (Fig 6.1c). The 100-500 °C range shows a modest correlation between annealing temperature and Al/Co. A more pronounced slope is seen from 500-700 °C, where Al/Co falls far below that of the lower temperature anneals. This type of rapid decrease in Al content measured by XPS is due to the diffusion of Al atoms into the NMC bulk. When atoms diffuse beyond the sampling volume of XPS, they are not detected. XPS sampling volume reaches to a depth similar to that of typical photoelectron escape depths, or <10 nm. Onset of observable

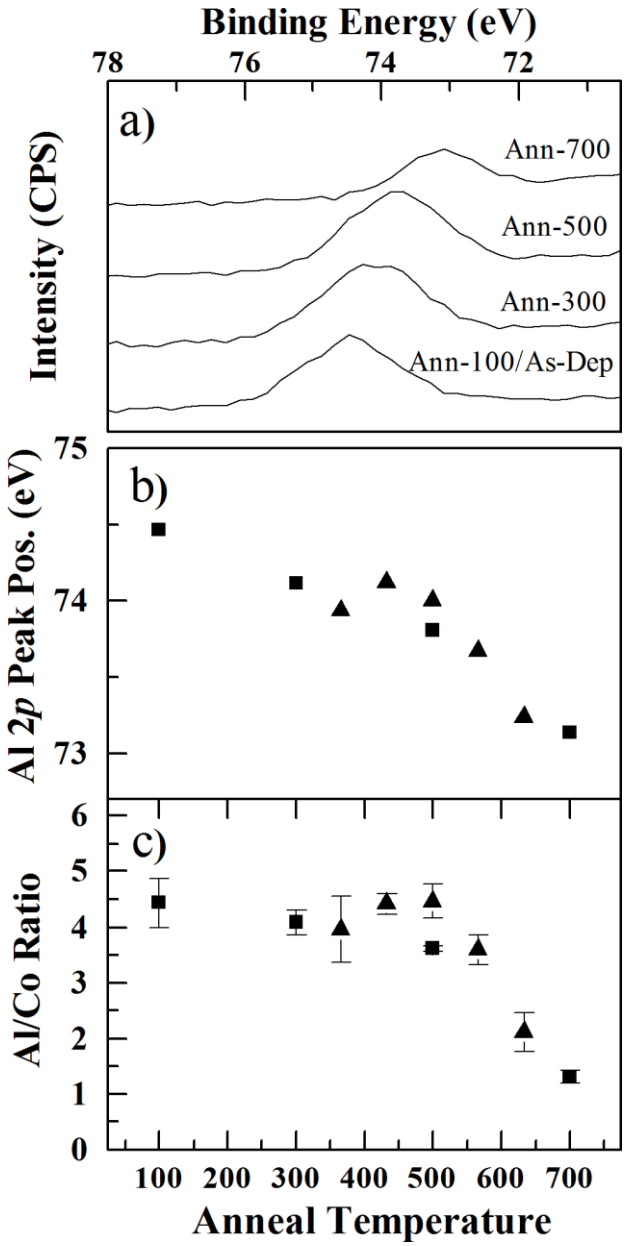

Figure 6.10. XPS of coated, annealed NMC. a) Al 2*p* region spectra, b) Al 2*p* peak position versus temperature, c) Al/Co ratio represents the quantity of Al at the surface of NMC. In panels b) and c) squares show the first batch of coated NMC powders while triangles show the second batch.

diffusion is at ~500 °C, and the extent of diffusion increases with increasing temperature (Fig 6.1c). Upon diffusion, Al atoms will form interstitial ions or substitute for metal atoms in the NMC lattice, both processes support the shift in peak position observed in Figure 6.1b.

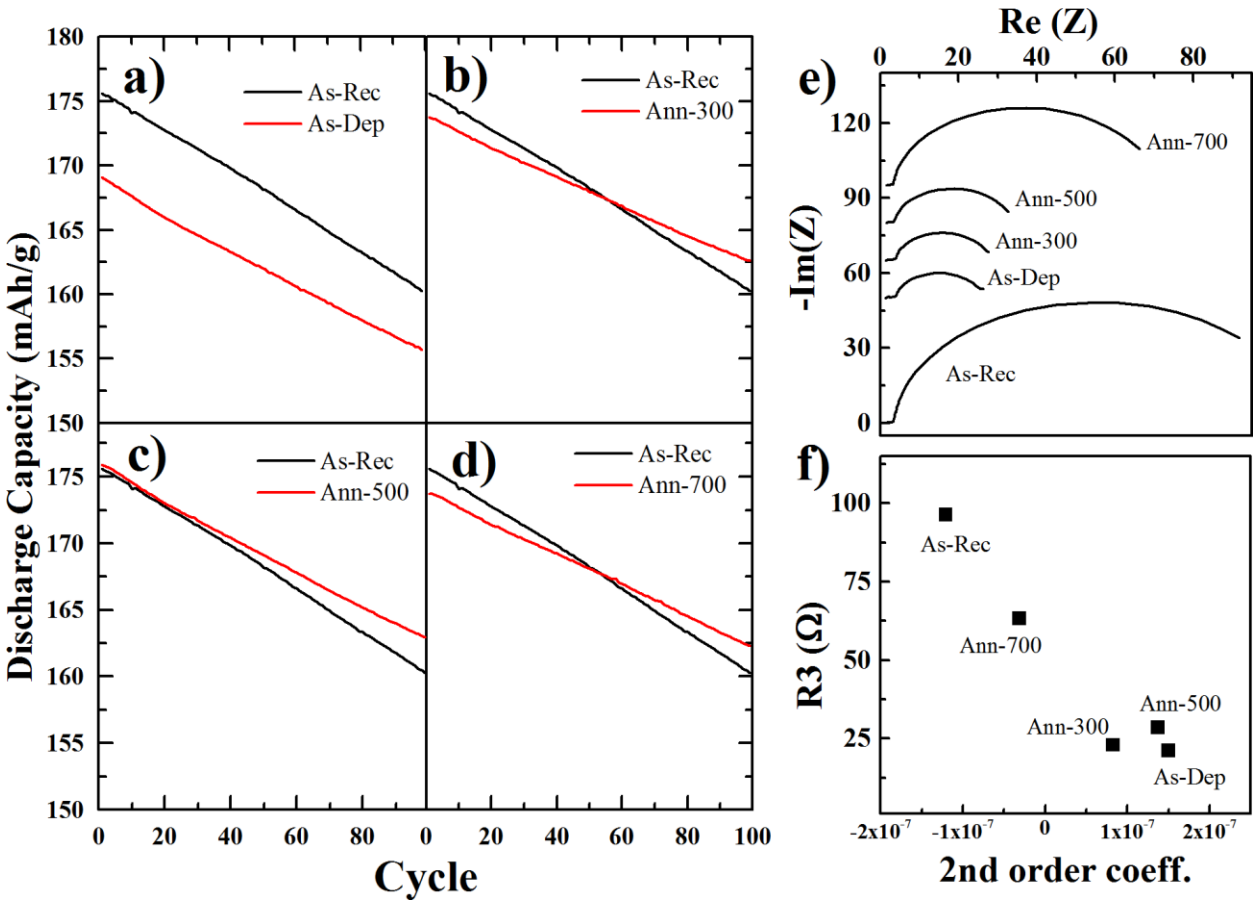

Figure 6.2. a-d) C/5 rate discharge capacity profiles of experimental cells plotted with the As-Rec control sample for comparison. e) C/5 EIS results, and f) R3 versus the 2nd order coefficient, R3 represents the large semicircle in the EIS data, which corresponds the resistance of the SEI layer.

Coin cells were cycled 100 times at a C/5 rate. The results of cycling are shown in Figure 6.2, with each of the experimental samples displayed against the As-Rec control sample. In this test, the As-Dep started with an initial discharge capacity ~5 mAh/g lower than the control (Fig 6.2a). This loss of initial capacity is attributed to lower Li^+ ion diffusivity, or sequestration of Li^+ in the Al_2O_3 film as ALD coatings formed at low temperature have high proton concentration, perhaps acting as an exchange ion.[14] Performance of all cells was similar, though Ann-300 and Ann-700 retained 93.6±0.3% and 93.4±0.1%, respectively, of initial discharge capacity over 100 cycles. These two values were the highest of samples tested.

After 100 cycles at C/5 rate, cells were examined using EIS (Figure 6.2e). The resistance corresponding to R1 is the electrolyte resistance. R2 is the real impedance assigned to the interface between coating and cathode and is too small to be easily seen at the figures scale. R3 is attributed to the SEI layer, with a larger R3 implying a thicker SEI layer.

In addition to the comparison of the discharge capacity retention, discharge profile curvatures were analyzed to show the dynamic nature of surface reactions occurring within the cell during operation. The discharge profile curvature was defined as the second order coefficient to a parabolic line fit to the profiles shown in Figure 6.2a-d. Figure 6.2f shows curvature plotted against R3, with a negative linear trend observed. Negative curvature (concavity), as seen in As-Rec, indicates that discharge capacity fade increases at an accelerating rate during cycling. A thicker SEI (larger R3) would result from parasitic reactions that accelerate as cycling continues. The positive curvature (convexity) seen in the measurement of As-Dep, Ann-500 and Ann-300, corresponds with smaller R3. Convexity implies a decelerating charge capacity fade, so that the NMC capacity becomes more stabilized the longer cycling continues. Reduced parasitic reactions would result in a thinner SEI layer, and convexity would yield smaller R3.

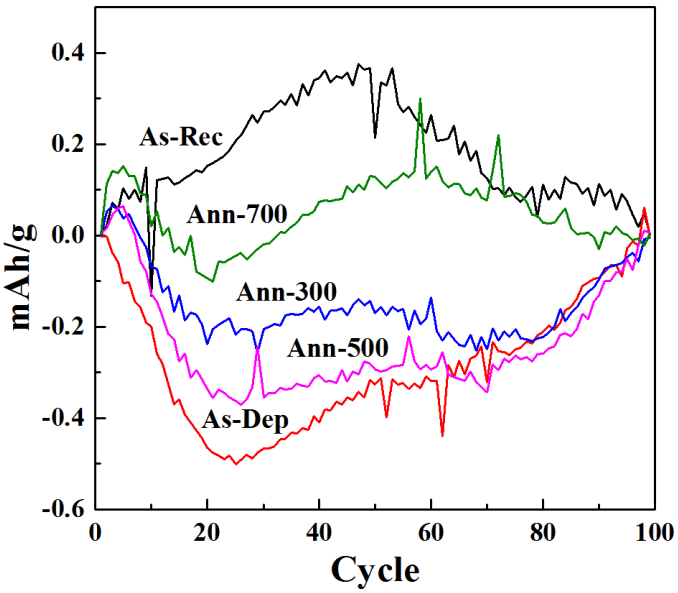

Figure 6.3. Discharge profile at C/5 rate with end-to-end line fit subtraction. Convex curvature means that the rate of loss in charge capacity per cycle is decreasing while concave curvature means it is increasing.

Figure 6.3 shows the discharge profiles of C/5 samples normalized to show the convex/concave nature of the profiles in greater detail. This normalization consisted of subtracting a line fit to the two end points of the discharge capacity profile. While the parabolic fit used above in Fig 6.2f reflects the curvature of the profiles in very general terms, the end-to-end line fit subtraction in Figure 6.3 shows the more detailed structure of the profile with multiple peaks and valleys. A detailed analysis of the peak structure could yield more information about surface reaction dynamics during cycling, though that analysis is beyond the scope of the current study.

Figures 6.4a-d show the discharge profiles of half cells cycled at a rate of 5C with a 2 hour potentiostatic hold at 4.3 V after every charge. Overall, As-Dep showed the smallest loss in discharge capacity, falling to 60.7±1.1% after 100 cycles. Some improvement over As-Rec was seen with Ann-500 and Ann-700. Ann-300 performed the worst, being nearly identical to As-

Rec, and falling to 49.8±9.3% of its initial discharge capacity. Ann-300 also demonstrated the largest error bars, and thus was the least reproducible.

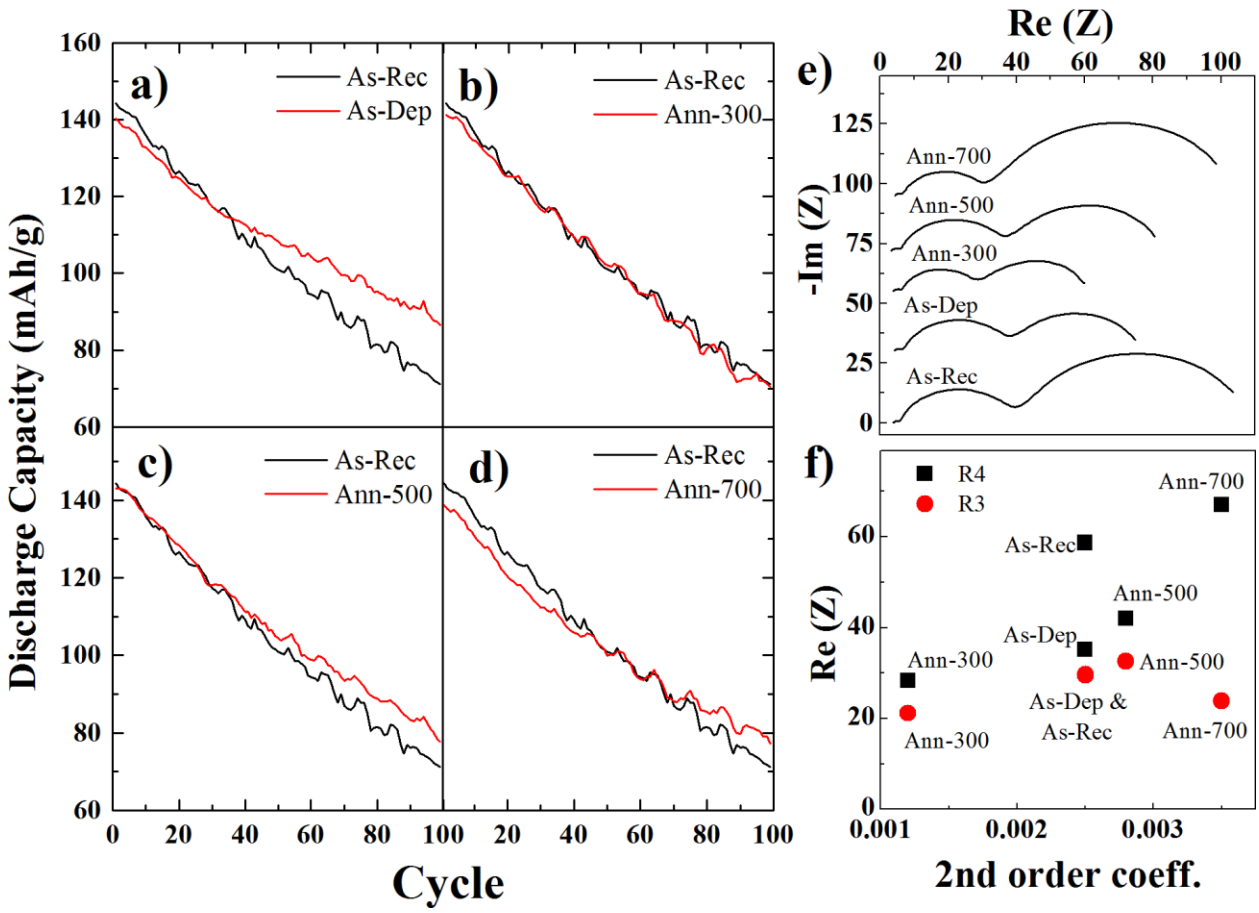

Figure 6.4. a-d) 5C rate discharge capacity profiles of experimental cells plotted with the As-Rec control sample for comparison. e) 5C EIS and f) Real impedance of R3 and R4, the two large semicircles representing the interface of the film and the resistance of the coatings, respectively. f) R3 and R4 versus the 2nd order coefficient to a 2nd order polynomial fit of the discharge profiles.

Nyquist plots in Figure 6.4e show post mortem EIS measurements performed after 100 cycles at 5C, with impedance components named R1-R4 moving from left to right. R1 is the electrolyte solution impedance. R2 is the real impedance attributed to the interface and belongs to a semicircle too small to be seen at the current scale. R3 is attributed to the ALD coating, and

R4 is attributed to the SEI layer (both also semicircles).[15, 16] Interestingly, Ann-300 had the smallest R4 impedance, despite being the worst performing sample with the highest capacity loss. Similarly, the well performing As-Dep had the largest R4 impedance. It is worth noting that R3 appears bimodal, as Ann-300 and Ann-700 have R3 = ~20 Ohms, while the other samples are ~30 Ohms.

In comparison of Figures 6.2e and 6.4e, it is observable that three semicircles are present in the EIS of 5C cells while only two are seen in the EIS of C/5 cells. The additional semicircles reflect differing electrochemically induced changes in the cells due to use of high and low rate cycling protocols.

Second order coefficients are plotted against the real impedances R3 and R4 in Figure 4f to reflect the relationship between curvature and SEI formation. No clear relationship between curvature and R3 is observed. R4 impedance and discharge profile curvature have a positive linear relationship, indicating that continuous generation of SEI layer during 5C cycling is generally desirable to prolong cycle lifetime. This correlation between curvature and SEI impedance is directly opposite to that seen in the C/5 cells shown in Fig. 6.2f, and suggests fundamental differences in cycle performance at high and low rates.

Table 6.1. Initial discharge capacity and discharge capacity retention after 100 cycles at 5C and C/5 rates.

	C/5 initial capacity (mAh/g)	**C/5 Capacity Retention (%)**	**5C initial capacity (mAh/g)**	**5C Capacity Retention (%)**
As-Rec	176	91.3±0.2	144	49.3±2.6
As-Dep	169	92.1±0.2	140	60.7±1.1
Ann-300	174	93.6±0.3	141	49.8±9.3
Ann-500	176	92.6±0.3	143	54.5±4.4
Ann-700	174	93.4±0.1	139	55.7±2.5

Table 6.1 shows initial discharge capacity and discharge capacity retention after 100 cycles of all samples at both 5C and C/5 rates. Ann-500 has the smallest reduction in starting capacity at C/5 rate, and As-Dep had a notably large reduction in C/5 initial capacity. In C/5 rate cycling percentage capacity retention did not deviate significantly (<0.3%) across any samples. The As-Dep sample had significantly higher 5C capacity retention than other samples. All ALD-coated samples outperformed the As-Rec controls at both C/5 and 5C rates, though suffered some loss in initial discharge capacity.

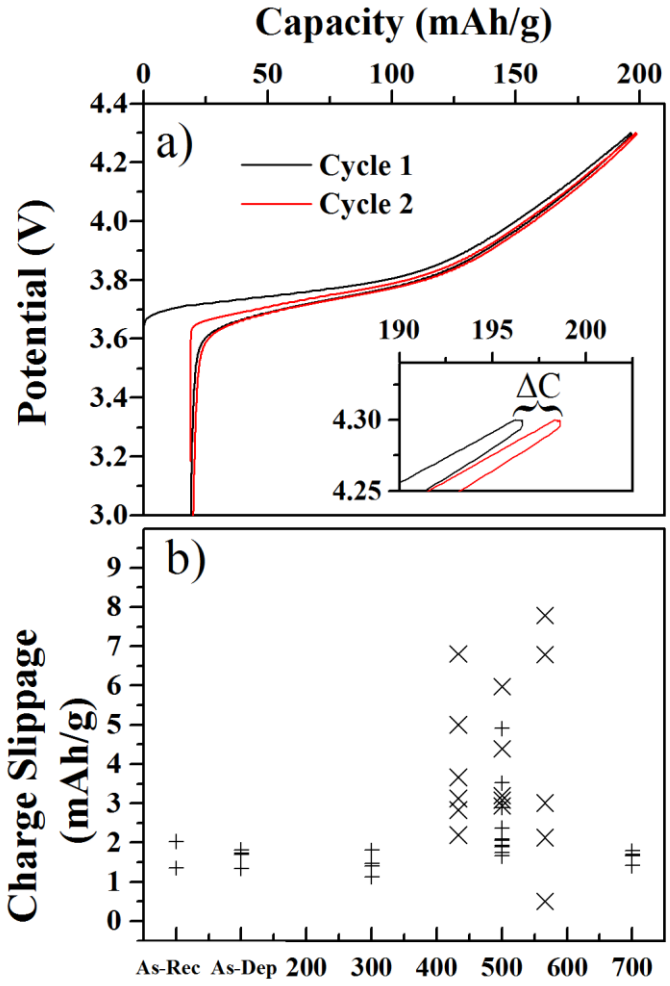

Figure 6.5. Example plot of charge endpoint slippage (ΔC) analysis of the first two cycles for As-Rec.

Before all cycling, cells were conditioned by performing two charge-discharge cycles at C/10. These C/10 cycles were used to measure charge endpoint slippage during initial charging and discharging. An example of an endpoint slippage plot is shown in Figure 6.5a. The difference between the charge endpoints of the first and second charge, denoted as ΔC, is the slippage. Slippage towards the right is generally attributed to parasitic side reactions.[17] Values for ΔC are shown in Fig 6.5b for each of the individual cells studied. Most samples tested had a similar ΔC of about 1-2 mAh/g, however Ann-500 showed a noticeably higher average value at ~3 mAh/g in the first batch of cells, and ~4 in a second, repeat batch. This high slippage was accompanied by much higher noise. In addition to a repeat of Ann-500, the second batch included Ann-433 and Ann-566, which also showed higher slippage and a higher level of noise. The ranges of values produced from Ann-433, Ann-500, and Ann-566 are much broader than As-Rec, As-Dep, Ann-300 and Ann-700, indicating inhomogeneity in the ALD coating characteristics that result in slippage. This result highlights the unique electrochemical properties of ALD films annealed in this narrow temperature range. Notably, this phenomenon occurs very close to the onset temperature of Al diffusion into the NMC bulk as seen in Figure 6.1c.

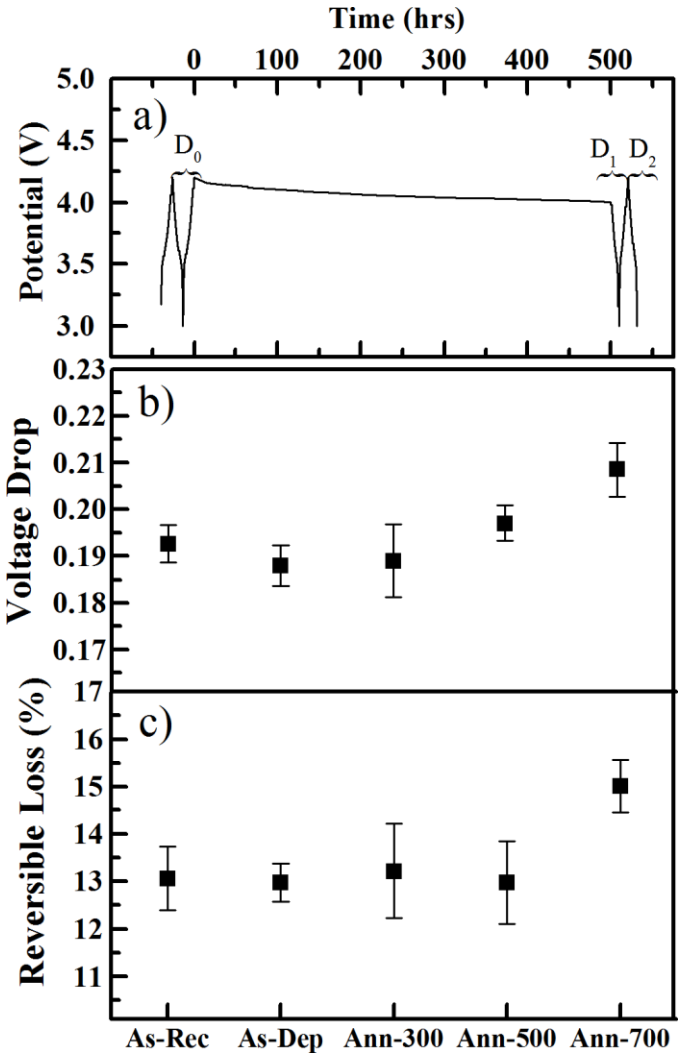

Figure 6.6. Elevated temperature storage experiment. (a) An example of the voltage versus time plot during a 500 hour open circuit hold at 40 °C (showing As-Dep), with the D_0, D_1 and D_2 discharges before and after the hold.

Elevated temperature storage tests were performed at 40 °C using full cells fabricated from graphite anodes instead of lithium (Figure 6.6). An initial charge-discharge cycle (D_0) was performed before the cells were charged to 4.2 V and held for 500 hours under open circuit conditions. After storage, the cells were discharged (D_1), charged, and discharged one final time (D_2). The difference between discharge capacities D_1 and D_2 gives the reversible capacity loss, while the difference between D_2 and D_0 gives the irreversible capacity loss.[17] Reversible loss is

defined as reversible charge transfer reactions that involve spontaneous discharge of charge carriers such as Li^+. Irreversible loss is categorized as the loss of active Li^+ into an electrochemically inactive form such as LiF, or as the dissolution of the electrode host matrix into solution.[18]

The voltage drop (Fig. 6.6b) observed during the experiment shows some dependence on annealing temperature in the ALD-coated samples, exhibiting a greater voltage drop with higher temperature annealing. As-Rec, As-Dep, and Ann-300 are the most effective at protecting the cathode surface and preventing spontaneous transfer of charges to or from electrode to solution, and Ann-700 is the least effective, facilitating self-discharge.

Figure 6c shows the reversible loss (D_1 - D_2) of samples. All samples show the same reversible loss within statistical variation, except Ann-700, which has a higher reversible loss. In addition to the highest reversible capacity loss, Ann-700 has the highest voltage drop. The positive correlation between voltage drop and reversible capacity loss is supported by existing literature.[18] Irreversible loss was also calculated though it does not show any trend, a result also consistent with the literature.[18]

After cycling tests, cells were disassembled and their cathode s were analyzed using XPS. Results from postmortem XPS chemical analyses are shown in Figure 6.7. Spectra were acquired before and after Ar^+ sputtering to analyze the SEI composition at the surface and within the SEI layer. Spectra of the O 1*s*, F 1*s*, P 2*p* and C 1*s* regions were acquired. Most spectral regions were easily deconvoluted into 2-3 component peaks, though the C 1*s* region did not lend itself to facile quantification,[19, 20] and detailed analysis of this region was not performed. The O 2*s* region in Figure 6.7a-b was deconvoluted to yield an oxide peak (529.6 eV), a Li_2CO_3 peak (532.0 eV)

and a carbonate, or RCO_3 peak (533.8 eV). The oxide peak was excluded from analysis, as the intention of this analysis was to examine SEI composition. The F 1*s* region in Figure 6.7c-d was divided into a peak associated with LiF (684.7eV) and a peak containing overlapping PvdF and $LiPF_x$ signals (687.0 eV). Finally, the P 2*p* region was divided into a $LiPF_xO_y$ (134.1 eV) peak and a $LiPF_x$ (137.2 eV) peak associated with the parent $LiPF_6$ molecule.

Comparison of chemical species before and after sputtering in the O 1*s* spectra (Fig 6.7a-b) show that the Li_2CO_3 content is generally higher at the surface of the SEI during C/5 cycling, while the Li_2CO_3 content is generally lower at the surface of the SEI in 5C cycling. RCO_3 content is higher in the 5C samples, indicating a greater degree of carbonate solvent decomposition, as would result from accelerated parasitic reactions under more aggressive cycling conditions. Among the 5C samples, the As-Rec has the highest amount of RCO_3, which indicates the highest degree of solvent decomposition. Figures 6.7c-d show the F 1*s* region. A notable observation here is an increase in LiF in Ann-500 at the surface of the SEI versus the interior composition. This observation holds for both 5C and C/5 rates. A higher content of LiF near the surface coincides with the onset of Al diffusion observed by XPS in pre-casting and pre-cycled NMC (Figure 1c). This also coincides with the anomalous charge slippage observed in Figure 6.5. The P 2*p* spectra in Figure 6.7e-f show a general trend of higher $LiPF_xO_y$ within the films as compared with at the surface, which most likely originates from decomposition and oxidation of $LiPF_x$ at the electrode-SEI interface.

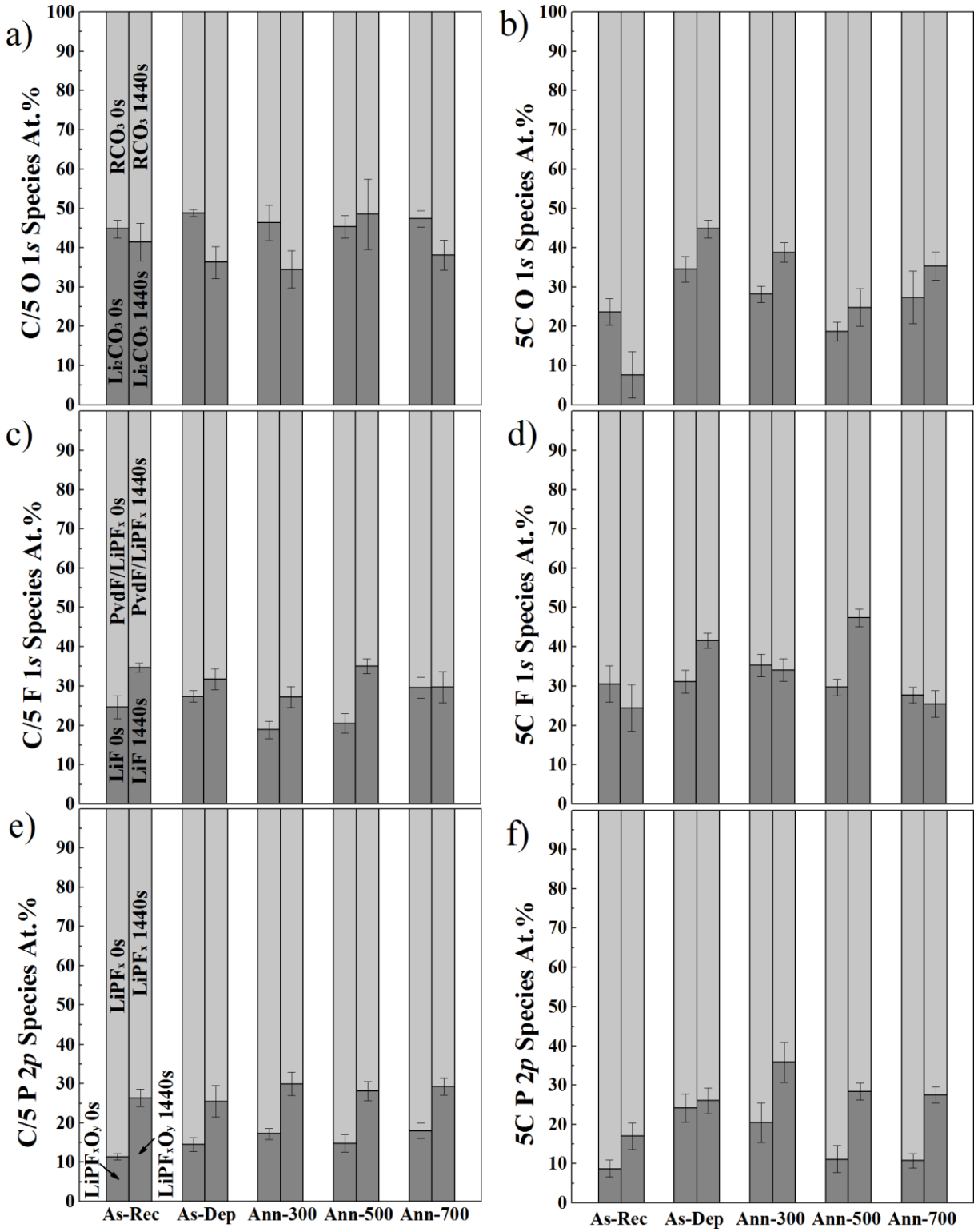

Figure 6.7. Post Mortem XPS depth profile of cells cycled at 5C and C/5 rates. Results for cycling at C/5 and 5C rates are shown for each sample. Adjacent pairs of columns show the composition of the SEI before and after a 1440 s sputter. Compositions were quantified using deconvolution of XPS peaks.

Powders that were ALD-coated and annealed at 500 °C showed the onset of diffusion of Al into the NMC bulk, the smallest reductions in starting cell capacity, increased parasitic reactions seen in charge endpoint slippage, and high quantities of LiF formed near the surface of the electrode within the SEI. These observations may be used to conclude the presence of a surface species formed as Al diffusion into bulk NMC become significant. The surface Al takes on unique chemical properties before diffusing into the bulk. This could be an intermediate species necessary for the transition from Al_2O_3 in the coating to Al in the NMC crystal. This species may be responsible for increased charge consumption measured during the initial cycles, the parasitic current resulting in formation of LiF. The unique Ann-500 surface leads to the best all-around electrochemical characteristics of all samples tested. It has the highest initial discharge capacity at high and low rates, has among the highest charge capacity retention at high and low rates, and does not suffer from accelerated self-discharge.

As-Dep has the lowest charge capacity loss at 5C, although it also has the lowest initial capacity in C/5 cycling. At C/5, As-Dep suffers from loss of charge possibly due to higher film impedance or to Li^+ sequestration within the ALD film due to ion exchange with protons remaining from initial ALD process.[14] These protons would leave the film during annealing, so the capacity loss should not appear in annealed samples. As-Dep is the most effective “high-rate” coating and shows low self-discharge.

The relationship between SEI impedance measured by EIS and the curvature of the discharge profile showed a negative linear relationship at C/5 and a positive linear relationship at C5. This contradiction is not trivial and highlights the complex relationship between SEI formation characteristics and charge-discharge rate.

6.3 Conclusions

Extensive characterization was performed to investigate the annealing of Al_2O_3 ALD-coated NMC powders. The un-annealed As-Dep samples which were ALD-coated at 100 °C show the lowest initial discharge capacity at C/5, but also show the best cycle performance at 5C. Samples annealed at 500 °C showed the best all-around performance with the highest initial capacity, among the best high and low rate discharge capacity retention tested, and no significant self-discharge. It was found that significant Al diffusion into the bulk NMC was apparent at and above an annealing temperature of ~500 °C. Surface species formed at Al diffusion onset result in higher parasitic reactions during the initial two cycles. The parasitic reactions led to a higher LiF content at the cathode-SEI interface than that observed in ALD samples absent this surface species. A deeper investigation into the relationship between annealing parameters at 500 °C, LiF formation, and performance metrics is an interesting direction for future research. Understanding the nature of the diffusion process observed here will be crucial for future researchers in this field. An interesting implication of this induced diffusion is that it could be used to produce particles with a radial composition gradient of Al, a concept which has shown recent promise.[21] Analysis of discharge profile curvature showed contradicting trends in the relationship between cycle performance and SEI layer impedance. Further exploration of this phenomenon would shed new scientific insight into the cycle rate dependence of reactions leading to charge capacity loss.

6.4 References

1. Van Noorden, R., The Rechargeable Revolution: A Better Battery. *Nature* **2014,** 507, (7490), 26-28.

2. Yabuuchi, N.; Ohzuku, T., Novel lithium insertion material of LiCo1/3Ni1/3Mn1/3O2 for advanced lithium-ion batteries. *Journal of Power Sources* **2003,** 119, 171-174.

3. Lu, Z. H.; MacNeil, D. D.; Dahn, J. R., Layered Li NixCo1-2xMnx O-2 cathode materials for lithium-ion batteries. *Electrochemical and Solid State Letters* **2001,** 4, (12), A200-A203.

4. Arora, P.; White, R. E.; Doyle, M., Capacity fade mechanisms and side reactions in lithium-ion batteries. *Journal of the Electrochemical Society* **1998,** 145, (10), 3647-3667.

5. Jung, Y. S.; Cavanagh, A. S.; Riley, L. A.; Kang, S. H.; Dillon, A. C.; Groner, M. D.; George, S. M.; Lee, S. H., Ultrathin Direct Atomic Layer Deposition on Composite Electrodes for Highly Durable and Safe Li-Ion Batteries. *Advanced Materials* **2010,** 22, (19), 2172-+.

6. Meng, X.; Yang, X.-Q.; Sun, X., Emerging Applications of Atomic Layer Deposition for Lithium-Ion Battery Studies. *Advanced Materials* **2012,** 24, (27), 3589-3615.

7. Bloom, I.; Trahey, L.; Abouimrane, A.; Belharouak, I.; Zhang, X. F.; Wu, Q. L.; Lu, W. Q.; Abraham, D. P.; Bettge, M.; Elam, J. W.; Meng, X. B.; Burrell, A. K.; Ban, C. M.; Tenent, R.; Nanda, J.; Dudney, N., Effect of interface modifications on voltage fade in 0.5Li(2)MnO(3)center dot 0.5LiNi(0.375)Mn(0.375)CO(0.25)O(2) cathode materials. *Journal of Power Sources* **2014,** 249, 509-514.

8. Xie, M.; Hu, T.; Yang, L.; Zhou, Y., Synthesis of high-voltage (4.7 V) LiCoO2 cathode materials with Al doping and conformal Al2O3 coating by atomic layer deposition. *Rsc Advances* **2016,** 6, (68), 63250-63255.

9. O'Neill, B. J.; Jackson, D. H. K.; Crisci, A. J.; Farberow, C. A.; Shi, F. Y.; Alba-Rubio, A. C.; Lu, J. L.; Dietrich, P. J.; Gu, X. K.; Marshall, C. L.; Stair, P. C.; Elam, J. W.; Miller, J. T.; Ribeiro, F. H.; Voyles, P. M.; Greeley, J.; Mavrikakis, M.; Scott, S. L.; Kuech, T. F.; Dumesic, J. A., Stabilization of Copper Catalysts for Liquid-Phase Reactions by Atomic Layer Deposition. *Angewandte Chemie-International Edition* **2013,** 52, (51), 13808-13812.

10. Lu, J.; Fu, B.; Kung, M. C.; Xiao, G.; Elam, J. W.; Kung, H. H.; Stair, P. C., Coking- and Sintering-Resistant Palladium Catalysts Achieved Through Atomic Layer Deposition. *Science* **2012,** 335, (6073), 1205-1208.

11. Kim, H.; McIntyre, P. C.; Saraswat, K. C., Effects of crystallization on the electrical properties of ultrathin HfO2 dielectrics grown by atomic layer deposition. *Applied Physics Letters* **2003,** 82, (1), 106-108.

12. Kim, E. J.; Wang, L. Q.; Asbeck, P. M.; Saraswat, K. C.; McIntyre, P. C., Border traps in Al2O3/In0.53Ga0.47As (100) gate stacks and their passivation by hydrogen anneals. *Applied Physics Letters* **2010,** 96, (1).

13. Moulder, J. F.; Stickle, W. F.; Sobol, P. E.; Bomben, K. D., *Handbook of X-ray Photoelectron Spectroscopy*. Perkin-Elmer Corporation, Physical Electronics Division: Eden Prairie, Minn. 55344, 1992.

14. Groner, M. D.; Fabreguette, F. H.; Elam, J. W.; George, S. M., Low-temperature Al2O3 atomic layer deposition. *Chemistry of Materials* **2004,** 16, (4), 639-645.

15. Bettge, M.; Li, Y.; Sankaran, B.; Rago, N. D.; Spila, T.; Haasch, R. T.; Petrov, I.; Abraham, D. P., Improving high-capacity Li1.2Ni0.15Mn0.55Co0.1O2-based lithium-ion cells by modifiying the positive electrode with alumina. *Journal of Power Sources* **2013,** 233, 346-357.

16. Bruce, P. G.; Saidi, M. Y., The Mechanism of Electrointercalation. *Journal of Electroanalytical Chemistry* **1992,** 322, (1-2), 93-105.

17. Smith, A. J.; Burns, J. C.; Xiong, D.; Dahn, J. R., Interpreting High Precision Coulometry Results on Li-ion Cells. *Journal of the Electrochemical Society* **2011,** 158, (10), A1136-A1142.

18. Sinha, N. N.; Smith, A. J.; Burns, J. C.; Jain, G.; Eberman, K. W.; Scott, E.; Gardner, J. P.; Dahn, J. R., The Use of Elevated Temperature Storage Experiments to Learn about Parasitic Reactions in Wound LiCoO2/Graphite Cells. *Journal of the Electrochemical Society* **2011,** 158, (11), A1194-A1201.

19. Quinlan, R. A.; Lu, Y. C.; Shao-Horn, Y.; Mansour, A. N., XPS Studies of Surface Chemistry Changes of LiNi0.5Mn0.5O2 Electrodes during High-Voltage Cycling. *Journal of the Electrochemical Society* **2013,** 160, (4), A669-A677.

20. Niehoff, P.; Winter, M., Composition and Growth Behavior of the Surface and Electrolyte Decomposition Layer of/on a Commercial Lithium Ion Battery LixNi1/3Mn1/3Co1/3O2 Cathode Determined by Sputter Depth Profile X-ray Photoelectron Spectroscopy. *Langmuir* **2013,** 29, (51), 15813-15821.

21. Sun, Y. K.; Chen, Z. H.; Noh, H. J.; Lee, D. J.; Jung, H. G.; Ren, Y.; Wang, S.; Yoon, C. S.; Myung, S. T.; Amine, K., Nanostructured high-energy cathode materials for advanced lithium batteries. *Nature Materials* **2012,** 11, (11), 942-947.

7 Conclusions and Future Recommendations

Atomic layer deposition and post-deposition heat treatment of powder materials were used to engineer surfaces across a range of advanced material applications. Applications investigated were catalysis, electrocatalysis, and Li-ion batteries. In each case, the materials properties were studied in order to engineer functionality suited to the desired application. The effects of both deposition conditions and heat treatment on the materials were investigated; significant phenomena such as the generation of desired microstructure, surface chemistry and ionic diffusivity were discovered and characterized. The properties achieved by annealing are not accessible by ALD alone, it is the combination of coating and annealing that enabled these studies. Thermally induced interactions between the substrate and the coating or within the coating material itself were used to further tailor the properties of the coatings. This section contains a discussion of experimental results, suggestions for expanding on these studies, and outlines new powder ALD research directions built upon the over-arching lessons learned in the context of this cross-disciplinary study.

7.1 Conclusions

The mixing of ALD Mg-Al oxide film composition was performed by controlling the pulse ratios, spanning the range from pure MgO to pure Al_2O_3. It was found that the ALD-MgO was poly-crystalline with crystallites measured to be 2.8 nm by XRD using the Scherer equation. γ-Al_2O_3 coated by only MgO exhibited the smallest change in surface area, from 225 m^2/g before ALD to 140 m^2/g after, while the pure Al_2O_3 coating yielded a surface area of 15 m^2/g after coating. The difference in surface area is a result of the difference in crystallinity in the coatings. The amorphous Al_2O_3 coating conformally fills all mesopores, eliminating pore volume and reducing the surface area. MgO deposits containing nanometer scale crystallites and these

crystallites grow within the mesopores of γ-Al_2O_3 to yield new surfaces within the internal volume of the particle. The mixing of Mg and Al pulses leads to lower surface area with lower Mg content. The mixed oxide samples do not exhibit any crystalline phases aside from the γ-Al_2O_3 phase attributed to the supporting particles. Annealing of the coatings led to significant changes in the catalyst microstructure. Surface area of all samples increased upon 600 °C calcination in air. MgO crystallites increased in average diameter to 10.9 nm due to sintering of crystallites or further crystallization of amorphous MgO domains. The surface area of non-crystalline mixed oxides and Al_2O_3 coatings increased due to a densification of films which led to increases in pore diameter. This densification did not result in changes in XRD spectra, and are assumed to have not led to formation of any new crystals apart from the possible generation of more γ-Al_2O_3. Instead, densification is attributed to a loss of interatomic void volume and loss of dangling bonds, such as dangling hydroxyls turning into water molecules and evaporating from the coatings.

The compositions of the ALD coatings were correlated to the acid and base site densities on the surface (measured in μmol/m^2). Base site density was linearly proportional to the Mg content, and acid site density was highest when the Mg and Al mixing was the highest. This demonstrates that base site generation was only dependent on the atomic fraction of Mg cations in the film, while interaction of the Mg and Al atoms led to the generation of acid sites. The presence of isolated base sites was inversely correlated to acid sites and thus to Al-Mg mixing. It is possible that the clustering of base sites was driven by a higher surface density of acid sites. While base site surface density was dependent on Mg content in the film, the catalytic activity of base sites decreased slightly with more mixing of Mg with Al.

Water oxidation electrocatalysts composed of cobalt nanoparticles supported on activated carbon powders were enhanced by overcoating with TiO_2-ALD films followed by heat treating under oxygen and then hydrogen. This procedure led to the formation of a microstructured coating on the Co particles in which the low index crystal planes were exposed while the edges and steps of the crystal were coated. This microstructure leads to stabilization of the particles while allowing for the cobalt-water interface necessary for the water oxidation reaction. Immediately following ALD, the coatings formed a continuous layer blocking the entire surface of the electrocatalytically active Co particles. Upon heat treatment under oxygen, pores in the coatings were generated. The subsequent reduction converted cobalt oxide to metallic cobalt and generated highly active catalytic sites formed at the interface of the Co and TiO_2.

XPS analysis of the catalysts showed that the amount of highly oxidized Co cations increased with increasing TiO_2 deposition. XPS showed that while the un-coated catalysts had predominately $Co(OH)_2$ at the surface, deposition of TiO_2 caused peak shifts and changes in the peak structure that have been reported to reflect Co^{3+} and potentially Co^{4+}. Ti peaks did not show changes associated with oxidation state, implying that upon interacting with Co, the Ti remains as TiO_2, while the Co changes due to the influence of the TiO_2 electronic structure.

While higher film thickness was correlated with better electrochemical activity, TiO_2 films as thin as 5 ALD cycles demonstrated 175% activity improvement in the water oxidation reaction. The sample with 60 ALD cycles, the thickest coating tested, demonstrated a 240% increase in activity. This improvement was attributed to the formation of the highly oxidized Co observed in XPS. The 60-cycle sample also demonstrated improved stability, retaining 75% of its initial current over 8 hours of continuous operation, compared to 50% observed with the

control. This stability was due to Co nanoparticle encapsulation by TiO_2 which prevented sintering.

NMC cathode powders coated with ALD-Al_2O_3 were annealed and the surface chemistry and microstructure that result from annealing were investigated and correlated to electrochemical performance of coin cells made using these powders. Deposition was performed at 100 °C, an atypically low temperature for ALD, which has been reported to yield Al_2O_3 films with high proton concentration.[1] Changes in the Al_2O_3 film upon annealing are in part attributed to the densification of films, as is observed in other studies.[2] This results in loss of hydroxyl groups and a decrease in interatomic void fraction within the film. Upon annealing at or above 500 °C, the Al_2O_3 coatings diffuse observably into the bulk NMC. Higher annealing temperature correlated with a greater degree of diffusion into the bulk. The temperature controlled diffusion of the ALD coatings is responsible for the changes observed in electrochemical behavior. Upon annealing at 700 °C, the highest temperature studied, more than half of the film diffused beyond the upper ~5 nm of the NMC particles. These samples should no longer be considered to have a coating at the surface of NMC, with the majority of the Al either incorporated into the NMC crystal structure replacing the Ni, Co or Mn transition metals in the lattice, or having intercalated between the layers of the oxide structure.

A range of electrochemical properties were examined to characterize annealed Al_2O_3-NMC, and no single treatment showed clear improvement across all studies. The un-annealed sample showed the best capacity retention during an aggressive cycling protocol consisting of high-rate charging and discharging in combination with extended potentiostatic holds at the end of each charge cycle. The un-annealed samples also exhibited significant loss of initial charge capacity during low-rate cycling. The Al_2O_3 deposited at 100 °C with low density and high

proton content may facilitate Li^+ transport and minimize parasitic reactions during high-rate cycling. The coatings as deposited also add impedance to the cells during low-rate cycling resulting in low initial capacity. Samples annealed at 500 °C were designated as the best all-around performers, due to their initial capacity, capacity retention at both high- and low-rate cycling, and self-discharge during an elevated temperature storage test. The sample annealed at 700 °C demonstrated similar desirable cycle performance, but underwent significantly higher self-discharge during the storage test.

Observable diffusion began at 500 °C, and samples annealed at this temperature also demonstrate the all-around best electrochemical properties. Charge endpoint slippage analysis of the first two cycles of all cells showed that samples annealed from 433 to 566 °C showed anomalously high charge consumption due to parasitic reactions. In a post-mortem XPS analysis, the 500 °C annealed cathodes also exhibited anomalously high LiF content within the SEI that had formed during cycling. As a result, the good performance of 500 °C annealed samples is attributed in part to a charge-consuming surface species that forms as diffusion into the bulk begins. This surface species may be associated with the high amounts of LiF detected. This surface species may be an intermediate chemical state between Al in Al_2O_3 and Al in NMC, which possesses chemical properties that enhance battery performance.

7.2 Recommendations for future work

This section contains suggestions for extending the research described here, and also suggests research in other fields that employ powders in an attempt to build off of the trends observed in this cross-disciplinary study.

Mixed oxide ALD has been demonstrated as an effective approach to tuning the acid base surface properties of a Mg-Al oxide. While the reaction used for characterization of samples was

a simple model reaction, the catalysts may be used for an exploration of bifunctional reaction mechanisms. Such a mechanism might require the presence of proximal acid and base sites for a single reaction step, such as the dehydrogenation of ethanol.

Deposition of TiO_2 onto a cobalt-carbon electrocatalyst represents the first study investigating the application of ALD-coated metal nanoparticles as an electrocatalyst. Possible directions for building upon this study would likely include exploration of other base metals such as nickel that are seen as not effective catalysts due to leaching, sintering and low catalytic activity. This electrocatalyst design approach may also be employed in the analogous fuel cell system, where similar reactions are required.

Improvements to Al_2O_3 ALD-coated battery cathodes have been achieved using a post-ALD annealing. With the acquired knowledge of the effects of heat treatment, advanced electrode oxide particles may be designed. For example, a controlled diffusion may be used to form a concentration gradient along the radial depth of a particle, consisting of a higher concentration of elements with high capacity on the particle interior, while a high concentration of elements imparting stability are on the exterior. Additional investigation of the suggested surface species forming at 500 °C annealing should also be performed. A better understanding of its chemical nature, formation, electrochemical properties, and its reactions with the electrolyte could lead to further optimization of electrodes. Electrode performance may also be engineered via post-deposition annealing towards a specific application such as high- or low-rate, or high temperature operation.

Phosphors are a powder materials application that may benefit from the use of ALD techniques investigated in this study. A phosphor is a material that exhibits luminescence, and is

usually doped with rare earth metals to generate color centers. Phosphors are used in a range of lighting and display applications including cathode ray tubes, and notably, in white light LEDs acting as light converters. A significant amount of light in LED conversion phosphors is lost due to scattering at the interface between the phosphor particles and the binders that embed them in the LED.[3] This scattering is caused by a difference in refractive index between the phosphor and binder, and might be mitigated by grading the refractive index at the interface, thus eliminating the sharp step in refractive index. Deposition of a compositionally graded coating or a coating of intermediary refractive index might solve this problem, and could be achieved through controlled diffusion of an ALD coating. Phosphor particles containing sulfides have been noted to degrade rapidly due to reactions with ambient moisture. One approach to increasing sulfide phosphor lifetime is to coat the particles with a moisture barrier. The excellent thickness control and conformality of ALD would allow for the thinnest possible functional moisture barrier, minimizing the light blocked by a coating.

In the field of medicine, drug delivery agents are currently a major focus of study, which are often high surface area powders that allow for absorption of drugs within the particle volume. These drugs may be released in a controlled manner either over time, or at a specific input signal such as the local biological environment, or electromagnetic radiation. The role of surface properties have been shown to regulate endocytosis, a key factor for intracellular drug delivery.[4] Surface functionalization can be used to control the drug-surface interactions. ALD may be a promising technique for the engineering of new drug delivery agents beyond the currently employed methods.

7.3 References

1. Groner, M. D.; Fabreguette, F. H.; Elam, J. W.; George, S. M., Low-temperature Al_2O_3 atomic layer deposition. *Chemistry of Materials* **2004,** 16, (4), 639-645.

2. O'Neill, B. J.; Jackson, D. H. K.; Crisci, A. J.; Farberow, C. A.; Shi, F. Y.; Alba-Rubio, A. C.; Lu, J. L.; Dietrich, P. J.; Gu, X. K.; Marshall, C. L.; Stair, P. C.; Elam, J. W.; Miller, J. T.; Ribeiro, F. H.; Voyles, P. M.; Greeley, J.; Mavrikakis, M.; Scott, S. L.; Kuech, T. F.; Dumesic, J. A., Stabilization of Copper Catalysts for Liquid-Phase Reactions by Atomic Layer Deposition. *Angewandte Chemie-International Edition* **2013,** 52, (51), 13808-13812.

3. Winkler, H.; Rueger, R. Coated phosphor particles with refractive index adaption. 2015.

4. Vallet-Regi, M.; Balas, F.; Arcos, D., Mesoporous materials for drug delivery. *Angewandte Chemie-International Edition* **2007,** 46, (40), 7548-7558.

8 Appendices

8.1 Safety considerations

The ALD growth process and other laboratory work involved in this study present many different safety concerns, including pressurized gases, high temperatures, and pyrophoric and/or toxic reactants. Several precautions were taken during the execution of experiments:

Pressurized cylinders containing inert N_2 gas were safely secured at all times during use. Cylinders are attached securely to a wall, and when being transported they are capped. Any damage to a high pressure cylinder would force high pressure gas out of the cylinder, turning it into an accelerated projectile that could cause large amounts of damage to people and the lab.

Metal precursors used in this study are all pyrophoric and will react violently upon exposure to air. In order to keep precursors separate from air, the ALD reactor must be maintained as air tight, requiring continual maintenance and upkeep of reactors. The reactor is leak checked using a helium leak checker, any leaks showing intake of helium into the reactor are addressed and eliminated by repairing gas panel connections and changing gaskets. Bubblers are attached to the reactor using leak free pneumatic valves to protect the bubblers from oxidants during depositions. Bubblers and the precursors they contain are handled in a glove box maintained in an oxygen and water free argon environment. During depositions the ALD reactor is held at rough vacuum, creating negative reactor pressure ensuring that no pyrophoric gasses escape from the reactor into the laboratory.

Deposition and powder annealing is performed at high temperatures ranging from 100 to 700 °C and should be considered dangerous. Heated furnaces are marked with appropriate signage, and time at high temperature is minimized by only heating the reactor during deposition.

8.2 Reactor schematics

Viscous Flow Reactor Schematic

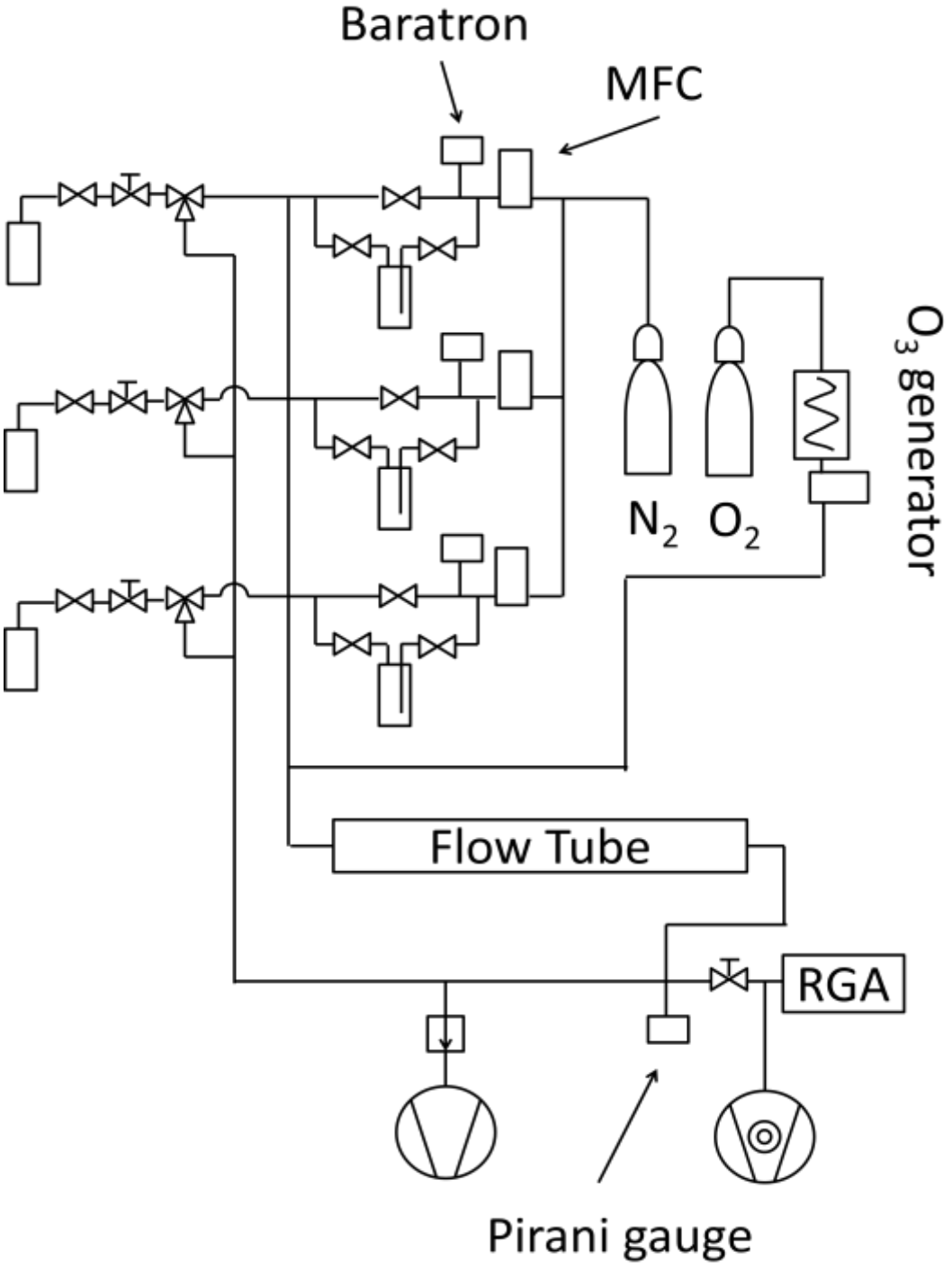

Fluidized Bed Reactor Schematic